2018

# Carbon support effects on Pd/C catalysts for the liquid-phase hydrogenation of multifunctional chemicals

Radhika Giri Rao
*Iowa State University*

**Carbon support effects on Pd/C catalysts for the liquid-phase hydrogenation of multifunctional chemicals**

by

**Radhika Giri Rao**

A dissertation submitted to the graduate faculty

in partial fulfillment of the requirements for the degree of

DOCTOR OF PHILOSOPHY

Major: Chemical Engineering

Program of Study Committee:
Jean-Philippe Tessonnier, Major Professor
D. Raj Raman
Aaron D. Sadow
Brent H. Shanks
Dennis R. Vigil

The student author, whose presentation of the scholarship herein was approved by the program of study committee, is solely responsible for the content of this dissertation. The Graduate College will ensure this dissertation is globally accessible and will not permit alterations after a degree is conferred.

Iowa State University

Ames, Iowa

2018

## DEDICATION

I would like to dedicate this thesis to my parents, Smita Giri Rao and Padmanabha Giri Rao and my grandmother, Manik Balwant Hawaldar. Their constant support and encouragement throughout my life made it possible for me to pursue a doctoral degree. They have sacrificed a lot to make my dreams come true and for that, I am eternally grateful.

TABLE OF CONTENTS

## ACKNOWLEDGMENTS

I would like to express my sincere gratitude and appreciation to my major professor, Dr. Jean-Philippe Tessonnier, for his mentoring and guidance during the years of my doctoral degree. Without his gracious support and encouragement, this work would not have been possible. His insights, knowledge, dedication, and motivation helped me in conducting good quality research at Iowa State University. During my time as a graduate research assistant, I have learned a lot from Dr. Tessonnier and I am very grateful to him for being an excellent mentor.

I am very thankful to my program of study committee members, Drs. Raj Raman, Aaron Sadow, Brent Shanks, and Dennis Vigil, for their valuable suggestions throughout the course of my doctoral work. I am grateful for the collaborations with researchers at Iowa State University, the University of Texas at Dallas, the University of Florida, the University of Strasbourg in France, the Technical University of Denmark, and the Fritz Haber Institute of the Max Planck Society in Germany. I appreciate the funding for this research, which was provided by the National Science Foundation Engineering Research Center- Center for Biorenewable Chemicals (CBiRC). Additionally, I am thankful to the department faculty members, staff, and my colleagues for all their help during my time at Iowa State University

The path to my doctoral degree was paved by the knowledge imparted to me by all my teachers and mentors. I am very grateful to them for their training and guidance. I would also like to thank my family and friends for their patience and unconditional support throughout my life. Their backing and encouragement are the key ingredients that made this thesis possible.

## ABSTRACT

Climate change due to anthropogenic greenhouse gas emissions is a major concern for nations worldwide. In order to mitigate the challenges associated with this issue, it is imperative for industrial sectors to switch to renewable feedstocks and energy sources for decreasing $CO_2$ emissions. Lignocellulosic biomass is one such alternative that demonstrates a promising future, specifically for the sustainable production of chemicals. However, the transition from a petroleum-based to a bio-based chemical industry poses new challenges for catalysis. In contrast to petrochemical reactions that are typically conducted in the gas phase at high temperature, biomass conversion reactions often require low temperature aqueous-phase conditions to mitigate the undesired side reactions and degradation of the feedstock molecules. Metal oxide supports that are commonly used in the petroleum industry (silica, alumina) lose their structural integrity in aqueous environments and, therefore, alternative supports and catalysts need to be developed. Carbon materials represent a suitable alternative to metal oxides as carbon-carbon bonds withstand hydrolytic attacks, under both highly acidic and basic aqueous environments, even in the presence of salts, which makes them a support material of choice for a broad range of biomass conversion reactions. However, these promising materials remain poorly understood and the structure-activity relationships required to design high-performance catalysts are still missing. The present work addresses this gap in knowledge. Specifically, we built this work on the hypothesis that structure-activity correlations can be established for carbon-supported metal catalysts by decreasing the support complexity and controlling the support properties at the nanoscale. We pursued this hypothesis and were able to deconvolve the contributions of the scaffold's surface

chemistry and electronic properties to the catalytic activity of the supported metal active phase.

In order to conduct a systematic study of support effects, we developed a synthetic platform based on stacked-cup carbon nanotubes (SCCNTs) as scaffolds. The key advantage of these SCCNTs is their dual structure consisting of a graphitic core and an amorphous carbon shell, which offers a handle on the graphitic character and surface chemistry through simple thermochemical treatments. Pd metal nanoparticles deposited on the SCCNTs were carefully characterized using advanced methods—aberration corrected transmission electron microscopy and synchrotron-based X-ray photoelectron spectroscopy—and the performance of the synthesized catalyst series was evaluated for the hydrogenation of cinnamaldehyde, an α,β-unsaturated aldehyde probe molecule. Strong correlations between the activity and selectivity of Pd/SCCNTs for the liquid phase hydrogenation reaction and the structure of the support were observed. Advanced characterization revealed that the observed trends could be assigned to electronic metal-support interaction (EMSI), resulting in a charge transfer and the formation of an electron-depleted $Pd^{\delta+}$ phase at the metal-carbon interface.

Once the presence of EMSI for carbon-supported catalysts was established, we attempted to quantitatively determine the contribution of the $Pd^{\delta+}$ phase to the overall performance of the Pd/C catalyst. Thermal annealing of the samples enabled incremental changes in the Pd particle size and Pd-C contacts. The analysis of the corresponding catalytic results revealed major differences in the selectivity and intrinsic rate of $Pd^0$ and $Pd^{\delta+}$ metal atoms, and demonstrated that controlling the structure of the carbon surface offers a powerful handle for tuning the activity of Pd/C catalysts.

As the MSI effects observed in this work were electronic in nature, the catalysts were further investigated by ultraviolet photoelectron spectroscopy in an attempt to explain the origin of the charge transfer and associate it with the scaffold's electronic properties. Linear correlations between the work function and band gap of SCCNTs and carbon nitride materials and the selectivity towards C=C bond hydrogenation were established. These results are expected to facilitate the development of strategies for rationally designing carbon supports for target biomass conversion reactions.

In summary, we developed strategies to control the properties of carbon supports at the nanoscale, we demonstrated the existence of electronic metal-support interactions for carbon-supported precious metal catalysts, and we established structure-activity correlations that may guide the rational design of next-generation hydrogenation catalysts.

# CHAPTER 1

# GENERAL INTRODUCTION

## 1.1 Introduction

The present-day demand for energy and chemicals is predominantly dependent on fossil resources.[1, 2] The magnitude of this dependence manifests itself in the 78.4% contribution of fossil fuels to the estimated total global energy consumption in 2015.[3] As the world population is expected to further increase until the end of the century, this demand and dependence is expected to follow the same trend.[4] Scientific evidence proves that anthropogenic activities, specifically the consumption of petroleum based fuels and chemicals leads to greenhouse gas emissions that adversely affect Earth's climate.[5] These effects cause increased occurrence of extreme weather conditions such as floods and droughts that disrupt agriculture and thereby affect food supply chains.[6] Climate change also leads to rising global temperatures that are expected to cause an increase in sea levels and disturb oceanic ecosystems.[6] In order to mitigate these challenges, nations worldwide are attempting to curb their greenhouse gas emissions by reducing our dependence on petroleum resources.

Lignocellulosic biomass is one of the promising renewable alternatives to petroleum.[7, 8] Biomass from agricultural waste and non-edible plants is an abundant, cheap, and renewable source of carbon that can facilitate the sustainable production of energy and chemicals. The need for a transition to a bio-based economy has been identified by several agencies. In the United States, the Department of Agriculture has set out a goal to produce 20% of the transportation fuel using biomass by 2030.[9] In addition to transportation fuels,

production of chemicals from lignocellulosic biomass has also been emphasized upon. The U.S. Department of Energy (DOE) has identified 10 platform chemicals and the main conversion pathways that will set the foundations for a bio-based chemical industry.[10] This proposal of the U.S. DOE also highlights that the platform molecules obtained from biomass contain a significant fraction of oxygen functionalities. Consequently, classes of reactions such as decarbonylation and hydrogenation that can selectively remove or modify oxygen-containing functional groups will be of central importance. Since these reactions typically involve the use of metal catalysts, it is essential to design catalytic materials that can selectively convert a target bond in multifunctional bio-based molecules.

The transition from a petroleum-based to a bio-based chemical industry poses new challenges for catalysis. While reactions in the petrochemical industry are typically conducted in the gas phase at high temperature, biomass conversion reactions often involve transformations in the condensed phase. In addition, water is commonly used as a solvent in the bio-based chemical industry due to its low cost and ability to dissolve polar oxygenates that are produced from biomass.[11] However, the use of water at temperatures above its normal boiling point, under extreme pH (very acidic or very basic conditions), and in the presence of salts creates new challenges for the stability of the current generation of heterogeneous catalysts that were initially developed for petrochemistry. Non-precious metal active phases such as nickel (Ni), iron (Fe), and their alloys were found to slowly dissolve (leach), especially below pH 4.5.[12, 13, 14] Additionally, many oxide supports and metal catalysts undergo structural reconstruction and partial dissolution under these reaction conditions.[15] Several groups reported that silica,[16] SBA-15,[16] alumina,[17, 18] zeolites,[19] and niobia[20] lose 50-90% of their surface area within 10-12 hours in water at 200 °C. Therefore,

the lack of stability of the support and catalysts represents a major roadblock for the development of a bio-based economy. New catalysts and supports that can demonstrate high stability and can selectively produce value-added chemicals under biomass conversion reaction conditions need to be developed.

## 1.2 Hydrogenation reactions

Catalytic hydrogenation reactions are of prime significance in the present-day chemical industry. These reactions are expected to play an increasingly important role in the biorenewable chemical industry due to their ability to convert functionalities, such as C=C and C=O, which are typically present in biomass-derived molecules.[21] This importance of hydrogenation reactions in the current and future chemical industry makes it one of the most widely researched areas in catalysis.[22]

### 1.2.1 Selective hydrogenation of α,β- unsaturated aldehydes

Selective hydrogenation of the functionalities present in biomass is vital for the production of value-added chemicals. Specifically, C=C and C=O bond reduction reactions are important due to the abundance of these functional groups in bio-based feedstock and platform molecules. Therefore, in this work we chose the hydrogenation of a model α,β-unsaturated aldehyde compound, containing an olefinic bond (C=C) and a carbonyl (C=O) group. Due to the structural similarities between α,β-unsaturated aldehydes and several monomers of lignin, these molecules and their selective conversion reactions are central for biomass conversion. Additionally, a large body of work is already available in the literature for the selective hydrogenation of these model compounds, which provides a strong

foundation of data for comparing our results. In addition to biomass conversion, these selective reduction reactions are also important for the fragrance, flavor, and pharmaceutical industry.[23] For example, cinnamaldehyde (3-phenyl-2- propenal) upon reduction of the C=O bond produces cinnamyl alcohol, which is widely used in the perfume industry. Similarly, in citral (3,7-dimetyl-2,6-octadienal), selective hydrogenation of the C=O bond results in the formation of geraniol which is utilized in flavors and mosquito repellents.[24] However, chemoselective reduction of α,β- unsaturated aldehydes is challenging since thermodynamics favors the C=C over C=O bond hydrogenation by about 35 kJ $mol^{-1}$.[25]

### 1.2.2 Role of the electronic and geometric properties of metal nanoparticles on hydrogenation activity

The selectivity of hydrogenation reactions can be tuned by altering the electronic and geometric properties of the metal catalyst. Correlations between the width of the d band, position of the d band center, and the catalytic performance of metals have been reported.[26, 27, 28] Based on this understanding, one simple method for modifying the selectivity involves changing the metal active phase itself. For example, in cinnamaldehyde hydrogenation, the selectivity towards unsaturated alcohol followed a decreasing trend with Ir > Pt > Ru > Rh > Pd.[23] A more elite strategy for tuning electronic properties involves alloying or doping the metal catalyst and thereby controlling its performance for selective hydrogenation.[29, 30, 31, 32, 33] This technique allows for the modification of the d band width at the surface of the active phase due to a combination of strain and ligand effects, which in turn governs chemical properties such as the dissociative adsorption energy of hydrogen.[34] The addition of a secondary element alters the electronic configuration and the coordination of the active metal

leading to a ligand-like influence.[34, 35] The bimetallic species also induce changes in the geometric structure by modifying the bond length and angle. These effects have a significant influence on the performance of the catalysts.[34, 35] While alloys are typically formed by deliberate addition of a secondary metal, interactions between the metal and a non-inert support can also lead to doping of the active phase. For example, in the case of Pt/ZnO catalysts, the formation of PtZn alloy was observed upon catalyst reduction.[36] The presence of the PtZn increased the selectivity towards the unsaturated alcohol in crotonaldehyde (but-2-enal) hydrogenation.[36] Therefore, changing the nature of the support can provide an alternate route to tuning the elemental composition and catalytic performance.

### 1.2.3 Reactant adsorption configuration

Altering the geometric and electronic structure of the metal typically influences the catalytic selectivity by modifying the adsorption mode of the reactant. For instance, the crystallographic planes at the catalyst surface were shown to affect the binding mode of 3-methylcrotonaldehyde on platinum.[37] Preferred adsorption and thereby hydrogenation of the C=O was observed on Pt (111) due to repulsion between the methyl groups attached to the C=C and this metal surface.[37] Similar results were observed for cinnamaldehyde hydrogenation with a higher selectivity to the unsaturated alcohol on Pt (111) as compared to Pt (100).[38] Theoretical calculations supporting these experimental observations were also reported.[26, 39] While controlling the crystallographic structure for altering reactant adsorption and product selectivity is an interesting approach, designing catalysts with specific facets is a challenging task. Currently, ligand-assisted synthesis of nanocrystals is a preferred approach for gaining precise control on their exposed facets.[40] In addition to tailoring the catalyst

structure, the ligands also open new opportunities for improving the catalytic performance. The concentration, size, and chemical functionalities of the ligands act as selectivity-switchers by altering the adsorption mode of the reactants.[41, 42] Similar effects were observed when varying the surface chemistry of the support.

### 1.2.4 Support effects

In the case of supported metal catalysts, the physicochemical properties of the support can influence the catalytic performance. This can occur through the interactions between the metal, the reactant/product molecules, and the support material. Specifically, the polarity of the support surface plays a major role in these interactions. For cinnamaldehyde hydrogenation, studies reported differences in selectivity depending on the support polarity due to the repulsion of the benzene ring in the molecule by the support's oxygen-functional groups (Figure 1).[28, 43, 44] Similar results were also observed for supports containing surface nitrogen-functionalities, wherein the preferential C=C hydrogenation increased with increasing nitrogen content.[45, 46] In addition to this, the support functional groups can also have an electronic effect on the metal catalysts, which have also been reported to affect the product distribution.[47] The oxygenated functional groups, for instance, can act as electron-donor sites resulting in an increase in the electron density on the supported metal nanoparticles.[23] These electronic effects were shown to increase selectivity towards crotyl alcohol in crotonaldehyde hydrogenation.[48]

While tuning the support functional groups offers an attractive approach for altering the catalytic performance, de-convolving the electronic and polar effects remains a challenge in catalysis. Additionally, limited support materials offer flexibility in modifying their

surface chemistry. These challenges act as a barrier in utilizing this technique for the rational design of catalysts for selective hydrogenation.

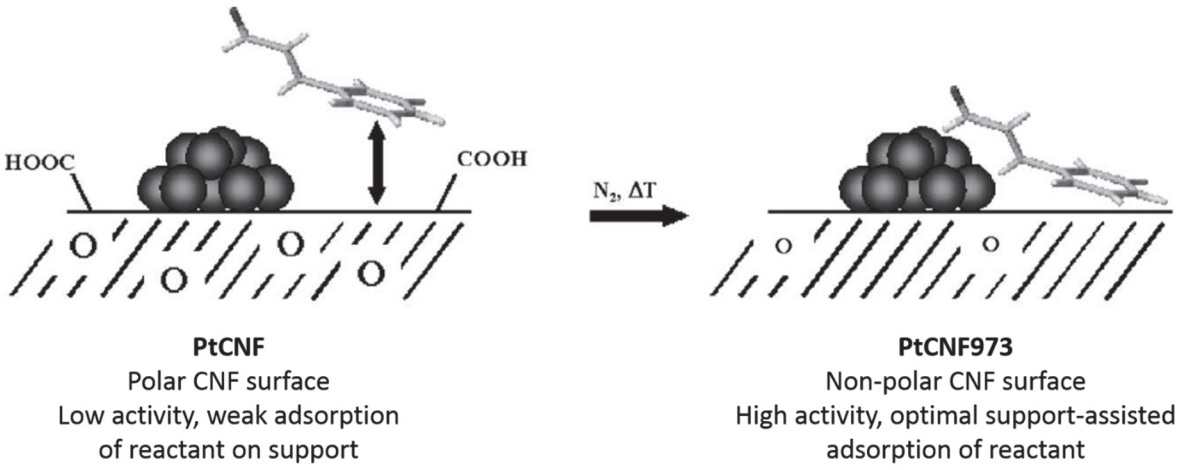


Figure 1. Schematic representation of cinnamaldehyde adsorption on the carbon nanofiber (CNF)-supported Pt catalyst. PtCNF represents Pt nanoparticles on CNF with oxygen-functional groups. PtCNF973 represents Pt nanoparticles on CNF after majority of the oxygen-containing groups on the support surface were removed by a treatment at 973 K (700 °C). Reproduced from [43].

### 1.3 Carbon materials

Carbon is one of the very few materials that offers an ease in the tunability of chemical and electronic properties, making it a material of interest for a wide array of fields from catalysis to energy storage and molecular electronics.[49, 50, 51, 52] Due to their high thermal and electrical conductivity, mechanical strength, and optoelectronic properties, carbon-based nanomaterials are also used for biomedical and photocatalytic applications.[53, 54] Additionally, carbon is structurally stable in liquid water under harsh conditions (high pressure, very low or high pH) due to the high resistance of carbon-carbon bonds to hydrolytic attacks. . Therefore, carbons are an attractive class of materials for the bio-based

chemical industry. This breadth of fields in which carbons are applied provides a perspective on the importance of studying these materials and understanding their properties at a fundamental level. In this report, we will primarily focus on the role of carbon materials as catalyst supports.

### 1.3.1 Carbon materials in catalysis

Carbons have been applied in catalysis for several decades due to their high surface area, relative inertness under acidic/basic environments, and low costs.[55] Another advantage is the facile recovery of the metal active phase by combustion of the carbon scaffold. Carbons also offer an ease in the tunability of surface functional groups using thermal and chemical treatments.

Currently, hundreds of different types of carbons are commercially available. The most commonly used carbon materials are activated carbons (AC). A schematic representation of ACs as shown in Figure 2, depicts the presence of polyaromatic hydrocarbon domains arranged in complex three-dimensional structures that are interconnected with amorphous carbon. AC is typically obtained from materials such as coconut shells, wood, or bamboo and demonstrates high surface area and low costs. However, due to the variations in the properties of the raw materials, significant differences in the impurities and nature of the carbons can be observed. Further, the complex three-dimensional structure aggravates the issues of mass transfer limitations and inhibits the rational design of supported catalysts. These challenges associated with AC can be addressed by synthetic carbons such as carbon nanotube (CNT) or carbon nanofiber (CNF) materials.

Figure 2. A schematic representation of an activated carbon comprising of polyaromatic hydrocarbon domains arranged in a complex three-dimensional structure. Reproduced from [56].

Catalytic chemical vapor deposition (CCVD) is the most common method used to grow CNTs and CNFs.[55, 57] In CCVD, the carbon-source decomposes on the surface of a metal catalyst, typically Fe, Co, or Ni, and the carbon dissolves in the nanoparticle catalyst to form carbides. The metastable carbide then decomposes into metal and graphitic carbon. The formation of the graphitic carbon increases the pressure and the catalyst particle is pushed out. Following this, the metal surface is exposed to the carbon source and the process of graphitic carbon formation continues. This mechanism for CNT and CNF synthesis using CCVD, depicted in Figure 3, is supported by several studies.[55, 57, 58, 59] Since CCVD is a bottom-up synthesis technique, it also allows the incorporation of heteroatoms such as nitrogen in the nanocarbons.[60, 61, 62] Additionally, depending on the size, shape, and elemental composition of the catalyst nanoparticle, the nature of the nanocarbons and their properties such as their diameter can be controlled. The tunable structure of the nanocarbons along with their high purity, mesoporosity, and high thermal conductivity, makes them attractive materials for catalytic applications.[55] However, high production costs of CNTs, five time higher than that of AC, along with the low bulk density of CNTs (60 – 280 kg $m^{-3}$) in

comparison to AC (300 – 580 kg $m^{-3}$) limits their economic viability for use in industrial reactors.[63]

In addition to AC, CNTs, and CNFs, collections of other carbons with different physicochemical properties are commercially available. While the wide variety offers several possibilities for catalysis, the structure-activity correlations for carbon-supported catalysts remain unclear. This gap in knowledge limits the optimum utilization of the current materials and inhibits the development of next-generation carbon-based catalysts. In order to overcome this barrier, it is imperative to first develop a fundamental understanding of the interplay between the properties of carbons and catalytic performance.

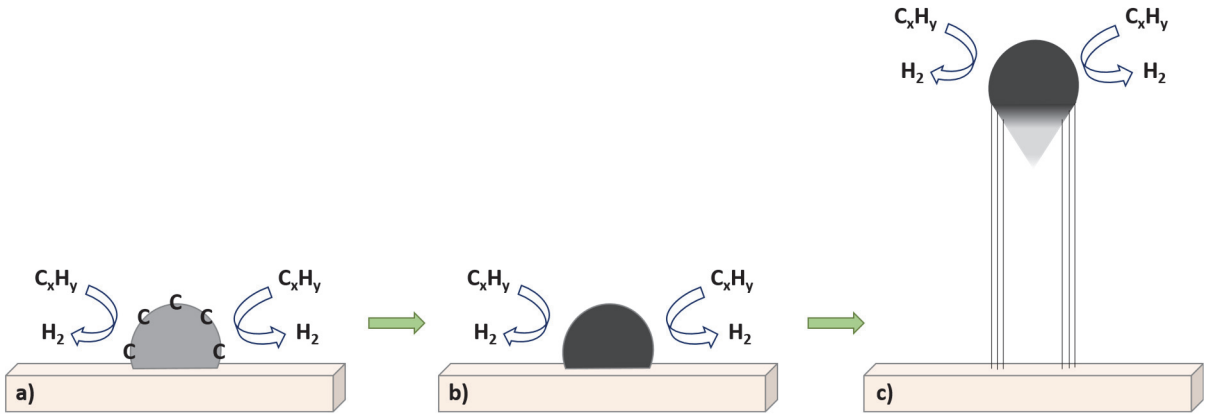


Figure 3. Schematic representation of growth routes of carbon nanotubes using catalytic chemical vapor deposition: a) decomposition of the carbon-source on the catalyst particle surface; b) carbon atom diffusion through the particle; c) precipitation of carbon and the formation of a nanofiber or nanotube. Adapted from [57].

### 1.3.2 Reactivity of carbons

One of the most important properties of materials in catalysis is their reactivity. Traditionally, carbons are considered to be inert in comparison to metal oxides due to the absence of Lewis acid groups on their surface. In addition, the weak Brønsted acid-base

functionalities that are present in carbons are not expected to directly participate in reactions. However, this inertness of carbon materials is relative and in the 1960s it was observed that AC can facilitate selected reactions.[64] The reactivity of AC was discovered to be a function of the activation process (steam, $CO_2$, $ZnCl_2$, etc.).[64, 65, 66] This behavior of carbons stoked interest in understanding the molecular level phenomena which govern their reactive nature.

Broadly, the important parameters that influence the surface properties, hence the catalytic activity, of carbons can be classified into three interdependent groups, namely their physical, chemical, and electronic structure. Attempts of understanding the correlations between these properties and the reactivity of carbons revealed some interesting results. In the case of defect-free fullerenes, the reactivity of the $sp^2$ hybridized carbons was due to the strain induced by the curvature of the nanocarbons.[67] Typically, $sp^2$ carbon atoms in any aromatic nanocarbon with a very high curvature (radius of curvature of 5 to 10 Å) will undergo a pyramidalization of its orbitals. This will strongly facilitate addition reactions that break the C=C and let atoms relax due to rehybridization to C-$sp^3$.[68] Chirality in single wall carbon nanotubes (SWCNTs) creates additional strain on C=C bonds due to "twisting" and leads to a misalignment of the $p_z$ orbitals.[69, 70] The high reactivity is not limited to well-defined nanocarbons like fullerene and SWNT, but it can also occur on any site with a very high local curvature. In the case of Stone-Wales defects (Figure 4), which are created in the process of strain relief, the presence of the C5 and C7 rings would induce curvature in the carbon materials.[67, 71, 72, 73]

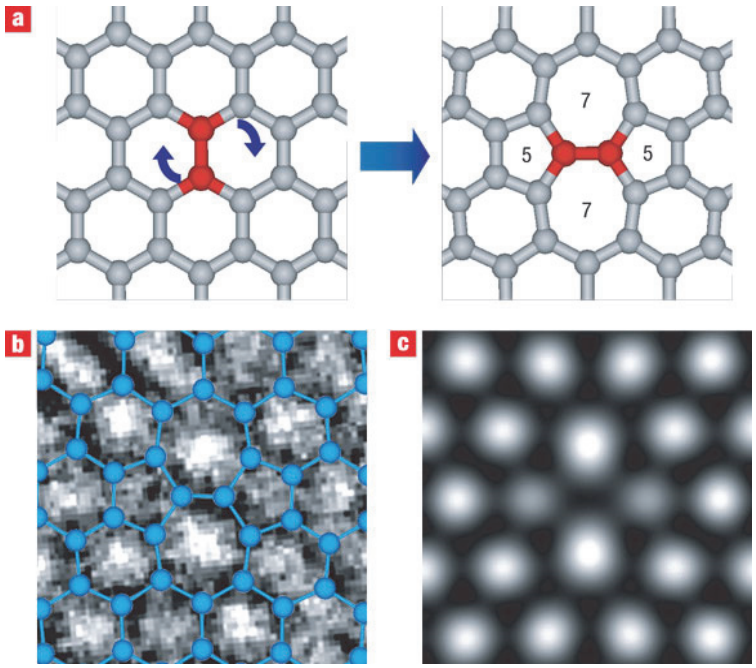


Figure 4. Atomic arrangement of the Stone–Wales (SW) model. a, The SW transformation leading to the 5–7–7–5 defect, generated by rotating a C–C bond in a hexagonal network. b, HR-TEM image obtained for the atomic arrangement of the SW model. c, Simulated HR-TEM image for the model shown in b. Reproduced from [74]

Typically, the interaction of defects with oxygen leads to modifications of surface properties. For instance, reaction of topological defects with strong oxidizing agents results in the formation of $CO_2$ and the creation of a vacancy. Therefore, carbons consist of defect-free graphitic domains that are interconnected by vacancies (Figure 5). The interaction of defects with oxygen also introduces oxygen-doped functionalities on the surface of carbon materials, for example around vacancies or edge/prismatic plane carbon atoms that are far more reactive towards oxidation than basal plane atoms.[75, 76, 77, 78] For instance, carbon atoms on the edges of graphene can lead to activation of $O_2$ to form epoxides that migrate or hop on the surface of the basal plane.[79, 80] Therefore, the presence of edges or defects is essential for introducing heteroatoms in the basal plane of carbons.

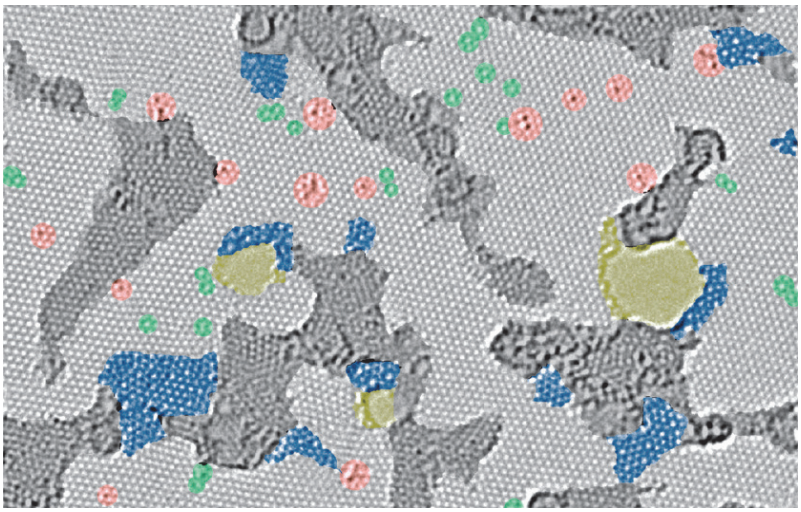

Figure 5. Aberration-corrected transmission electron microscopy (TEM) image of reduced-graphene oxide. Dark grey: contaminated regions; blue: disordered single-layer carbon networks or extended topological defects; red: ad-atoms or substitutions; green: isolated topological defects; yellow: holes and their edge reconstructions. Reproduced from [81]

Defects are generally introduced in the carbon materials during their synthesis.[57] However, post-synthesis defects can also be created with the help of strong oxidants, such as the mixture of nitric acid ($HNO_3$) and potassium chlorate ($KClO_3$) as proposed by B. C. Brodie in 1859, for the oxidation of graphene.[82] Similarly, the Staudenmaier method combined fuming $HNO_3$, concentrated sulfuric acid ($H_2SO_4$), and $KClO_3$ for graphite oxidation.[83] Further, Hummers and Offeman utilized sodium nitrate ($NaNO_3$), potassium permanganate ($KMnO_4$), and $H_2SO_4$ for further improving the process of graphene oxide (GO) synthesis.[84] Following these works, new methods that facilitated the introduction of oxygen functionalities on carbons using ozone,[85] oxygen plasma,[86] gas-phase oxidation using nitric acid vapors,[87] and several other strong oxidizing reagents were developed.

The introduction of defects and heteroatoms disrupts the delocalized electron cloud and alters the electronic properties at the carbon surface.[88] Thus, the presence of defects and heteroatoms influences the role of carbons as catalysts. Specifically, in the case of carbons as

supports, heteroatom-containing surface functional groups provide anchoring points for metal precursors, essential for decorating the scaffolds with metal nanoparticles. Therefore, it is important to understand the interaction of these sites and the metal active phase for the design of carbon-supported catalysts.

### 1.3.3 Carbons as catalyst supports

The synthesis of carbon-supported catalysts is a difficult task due the delicate balance that exists between the properties of the catalyst (particle size and shape) and its performance (activity, selectivity, and stability). This challenge is further aggravated by the lack of understanding of the interactions between the metal and the carbon scaffolds. Presently, methods for the synthesis of carbon-supported catalysts are based on the understanding developed from metal-oxide supported catalyst synthesis techniques with minor modifications based on surface properties of carbons.

One of the common methods for catalyst synthesis is incipient wetness impregnation. In this technique, the amount of the metal precursor solution is set equal to the pore volume of the support. The impregnation step is typically followed by drying, calcination, and reduction of the catalysts. The parameter that plays a major role in defining the properties of the final catalyst is the interaction between the metal and the support during each step of the synthesis. For example, the work of Brunelle in 1978 demonstrated that coulombic interactions between the metal precursor and the support are critical for the good dispersion of the active phase on the support.[89] The work specifically highlights the importance of the pH of the precursor solution and the isoelectric point (IEP) of the support, which together govern the adsorption phenomena. However, the evolution of charge on the oxygen-

functional groups with the pH is different for metal oxide materials and carbons. Silica is protonated at pH less than 1, remains almost neutral until in a pH range from 1 to 7, and only gets significantly charged at values over 7.[89] Carbon materials, on the other hand demonstrate an IEP in the pH range of 2-4 for oxidized activated carbon, between 4-5 for graphitic carbon and 8-10 for activated carbon.[90] The differences in the surface charging and zeta potential is due to the presence of a variety of oxygen-containing functional groups on carbons as opposed to hydroxyl groups on the metal oxide surfaces.

A variety of oxygen functionalities can be introduced on the surface of carbon materials as depicted in Figure 6. The functionalities on carbons can be divided into acidic, neutral, and basic groups. For instance, the carboxylic acid, quinone, and lactone groups demonstrate acidic behavior while phenols and ethers depict weakly acidic to neutral species. Depending on the amount and nature of the functional groups, the IEP of the carbon scaffolds varies, which influences the interaction between the metal precursor and the support. During the catalyst synthesis, an acidic precursor solution wherein the pH is lower than the pH of the isoelectric point ($pH_{IEP}$) of the carbon, a positive charge will develop on its surface leading to increased adsorption of the anionic precursor species. On the other hand, if the pH of the solution is higher than the $pH_{IEP}$, the carbon surface will develop a negative charge and thereby attract cationic precursor species. This amphoteric nature of carbons is represented in Figure 7.

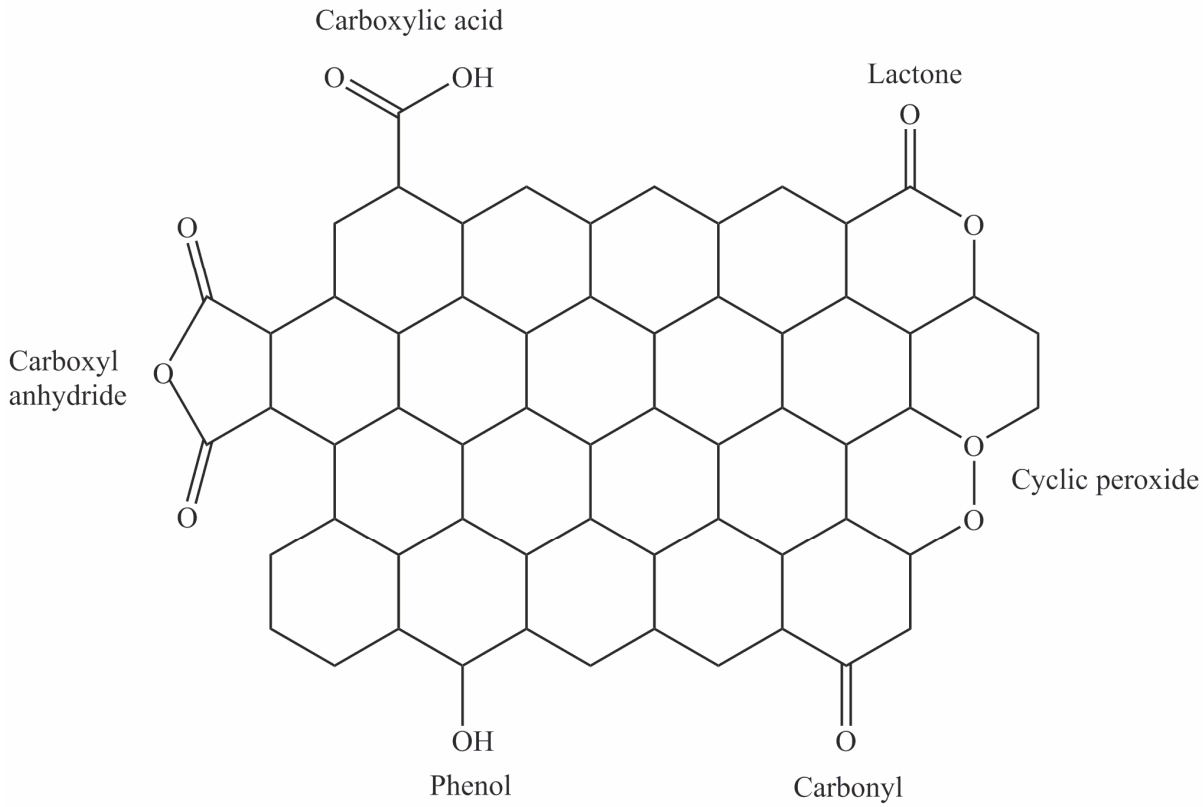


Figure 6. Oxygen-functional groups on graphitic carbon. Adapted from [91]

The differences in interactions have been demonstrated to affect the metal dispersion and catalyst stability. In Pd catalysts supported on activated carbon and carbon black, it was shown that higher dispersions were achieved with increasing amount of oxygen functional groups on the surface.[92] Similarly, for Pt catalysts, it was observed that the dispersion and sintering resistance increased with the amount of oxygen groups on the surface of activated carbon and carbon black.[93] This handle on the catalyst properties that is provided by carbon materials, opens several possibilities for catalyst design making carbons an attractive class of scaffolds.

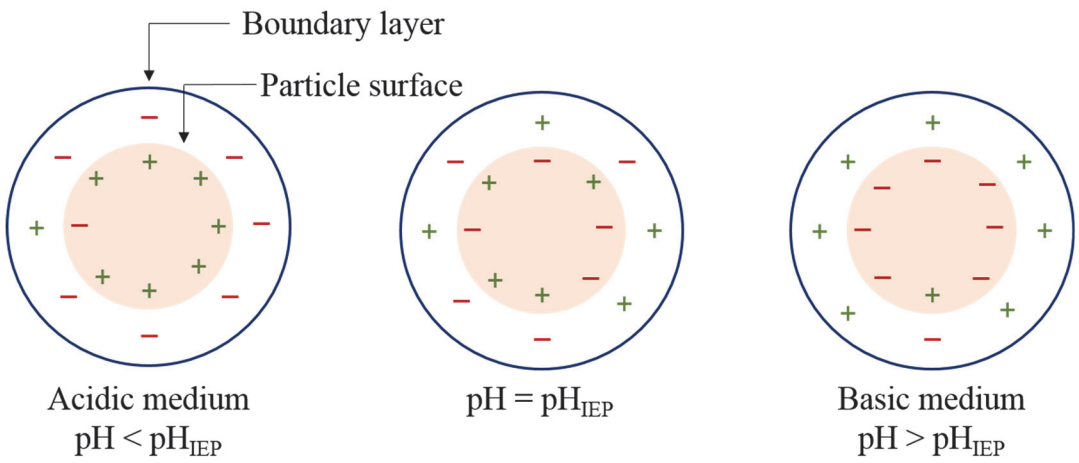


Figure 7. Amphoteric character of carbon materials. Adapted from [94]

### 1.3.4 Challenges for carbons in catalysis

While a certain level of understanding of the properties of carbon materials and control on the synthesis of carbon-supported catalysts has been established, many challenges plague the application of carbons in catalysis. For instance, currently collections of carbon materials with varied amounts of graphitic and functionalized components exist and "the best material" for a specific catalytic application is determined empirically. There is limited scientific guidance on the choice of materials, even though general features of carbon's chemical and material properties (porosity, conductivity, mechanical stability, hydrophobicity, resistance to hydrolysis) make these substances very appealing for catalytic applications. The structure-property-function relationships, that are key to catalyst and catalyst-support choices, are not established for carbon as they are for common metal oxides such as silica, alumina, ceria, or titania.[95, 96, 97] The nature (activated carbon, carbon black, nanotube, graphene) and the surface chemistry of the carbon support are known to impact the activity and stability of the catalysts.[98] However, the origin of these differences is not well understood and the rules for rationally designing carbon-supported catalysts are still lacking.

This gap in knowledge acts as a barrier for the design of new catalysts.

Determining the structure-property relationships that link atom hybridization, structure and functional group compositions to the metal-support interactions and catalytic activity is critically important for establishing general design rules for developing catalysts.[99, 100] Previous attempts in this direction have failed due to the structural and chemical complexity of the studied carbons.[101] For instance, in the studies focusing on understanding the effect of oxygen functionalized activated carbon on the catalyst performance, the influence of the graphitic domains and complex three-dimensional structures could not be elucidated.[102, 103] The challenges caused by the porous structure of activated carbons could be partly addressed by utilizing synthetic supports such as CNTs due their hollow cylindrical tubular geometry. However, despite meticulous studies, the problems associated with the chemical properties of the CNTs and the nature of their interactions with the metal active phase remained unclear.[43, 104, 105, 106] In addition to the differences in chemical properties of carbon materials, alterations in the electronic properties of carbons due to curvature or the incorporation of heteroatoms creates more barriers for the rational design of carbon-supported catalysts.[107, 108]

Due to this complex nature of carbon materials, studies reported in the literature were not able to unravel the metal-support interaction effects for catalysts utilizing carbon scaffolds. Specifically, previous works did not permit to isolate the covalent (metal-carbon bonds) from the non-covalent (ligand-like) effects at the metal-carbon interface. Decoupling the electronic and chemical effects, from transport limitations is required for the development of general design principles for selective and stable catalysts. The current state-of-the-art has not achieved success in decoupling the chemical, electronic, and transport effects in carbon-

based catalysts. This lack of understanding acts as a major roadblock in the rational design of carbon-supported catalysts and limits their applications for a broad array of reactions.

### 1.4 Research rationale

Research efforts from computational studies have provided evidence for electronic interactions between the metal active phase and carbon supports. Theoretical calculations have been performed for various metal (Fe, Ni, Pd, Pt) clusters and nanoparticles interacting with carbon at the basal plane (graphene-like honeycomb structure), prismatic plane (stacked edges), and defect sites (vacancies).[109, 110, 111, 112, 113, 114, 115, 116] All the calculations predicted important charge transfers between the metal and the carbon support. The intensity and direction of the charge transfer depend on the size of the metal cluster (5 to 100 atoms) and on the local electronic configuration of the carbon support, which varies with chirality, curvature, structure of the surface (basal vs prismatic), and the presence of heteroatoms (doping, functionalization).[109, 112, 113, 114, 115] Despite the prediction of electronic metal-support interactions provided by theoretical calculations, there is little experimental evidence for these effects.

In addition to these non-covalent interactions, carbon atoms from the support may also penetrate the cluster and form new metal-carbon bonds at the interface.[111, 117] The formation of interfacial non-stoichiometric carbide for 5 nm Ni particles supported on defective carbon (high $sp^3/sp^2$ ratio) has been observed.[117] X-ray photoelectron spectroscopy (XPS) and X-ray absorption spectroscopy (XAS) investigation carried out by other groups on Pt/CNT samples revealed that covalent and non-covalent interactions at the metal-carbon interface also impact the electronic structure of metal atoms in the bulk and at the surface of

the nanoparticle. Differences in catalytic activity have been measured experimentally in agreement with these XPS/XAS investigations.[118] The observed differences in catalytic activity are likely due to more than one effect. Although there is some understanding of these effects, an in-depth perspective of their influence on the interactions between the metal and the support is still missing. A fundamental understanding of each of these effects and strategies to control their contribution to the metal-support interactions need to be developed.

### 1.5 Research hypothesis and overarching goals

Our research project is built on the hypothesis that contributions from covalent and non-covalent metal-support interactions to the catalytic activity can be isolated and studied systematically if the heterogeneous catalyst is synthesized using a bottom up approach and/or the structure of the support is controlled at the atomic level. In order to test our hypothesis, two main strategies will be utilized in this thesis. In the first approach, the support materials will be systematically chosen from commercially available ones and their properties will be controlled using simple thermochemical techniques. In the second strategy, carbon supports will be synthesized from scratch and precise control on the support properties will be developed. The combined information obtained from these two approaches will together help in tailoring the interfacial metal-support interactions.

The overarching goal of this work is to develop a detailed understanding of the influence of metal-support interactions, nature of the support material, support functionalization, and defects on the catalytic performance. We will specifically probe the correlations between the properties of carbon materials and selectivity of supported noble metal catalysts for α,β- unsaturated aldehydes. The hydrothermal stability of carbon materials

could make the studied catalysts applicable for reactions in liquid water at high temperature. However, this aspect of stability will not be addressed in our work due to the challenges associated with sintering of metal nanoparticles under aqueous media at high temperatures, which makes it difficult to study the metal-support interaction effects. We will be exclusively focusing on tuning the catalyst performance for the selective hydrogenation of C=C vs C=O bonds that are commonly present in biomass-derived platform molecules. Our work will thereby establish general design principles for the development of selective carbon-based catalysts for biomass conversion reactions.

Our interdisciplinary approach, combining knowledge from materials chemistry and chemical engineering, will lead to a deeper understanding of carbon and nanocarbon supports for applications in catalysis. Our work will demonstrate that carbon is not an inert catalyst support despite its high structural and chemical stability in aggressive media; instead, nanocarbons with tailored functional properties actively contribute to the catalytic activity and facilitate desired reaction pathways. In addition, the results of this study will set the foundations for design rules that will guide future catalyst design for selective hydrogenation reactions beyond the compounds studied within the framework of this project.

### 1.6 Scope and outline of the thesis

In an effort to develop a fundamental understanding of the metal-support interactions for carbon-supported catalysts, three studies will be presented. In Chapter 1, a literature review focused on the importance and challenges of carbon materials in catalysis has been presented. This chapter provides a background and an outline for the overall objectives of this thesis. Chapter 2 investigates the effects of diffusion limitations in batch and flow

reactors under the conditions of interest for this work. Chapter 3 is a detailed study that provides strong evidence for the presence of electronic metal-support interaction effects for palladium on carbon catalysts. It establishes coherent trends between the properties of the carbon scaffolds, the amount of charge transfer between the metal and the support, and the performance of the catalysts, thereby providing a handle on the design of the next generation of carbon-based catalysts. Chapter 4 furthers the understanding of the impact of palladium particle size and interfacial metal-support interactions on the performance of Pd/C catalysts. Chapter 5 develops correlations between the electronic nature of different types of carbons and their influence on the metal-support interaction effects. These chapters are standalone manuscripts and have been formatted in a journal specific manner. Chapters 6 and 7 provide a conclusion for the work conducted thus far and a plan for the future direction, respectively.

## 1.7 References


1. Annual energy outlook 2017 with projections to 2050: U.S. Energy Information Administration; 2017.
2. International energy outlook 2016: U.S. Energy Information Administration; 2016.
3. Renewables 2017 global status report; 2017.
4. Gerland, P. et al. World population stabilization unlikely this century. *Science* **346,** 234-237 (2014).
5. Hansen, G. & Stone, D. Assessing the observed impact of anthropogenic climate change. *Nat. Clim. Change* **6,** 532-537 (2016).
6. U.S. Global change research program. [cited 2017] Available from: http://www.globalchange.gov/
7. Li, C., Zhao, X., Wang, A., Huber, G. W. & Zhang, T. Catalytic transformation of lignin for the production of chemicals and fuels. *Chem. Rev.* **115,** 11559-11624 (2015).

8. Simonetti, D. A. & Dumesic, J. A. Catalytic strategies for changing the energy content and achieving C-C coupling in biomass-derived oxygenated hydrocarbons. *ChemSusChem* **1,** 725-733 (2008).

9. USDA announces investments in bioenergy research and development to spur new markets, innovation, and unlimited opportunity in rural america: U.S. Department of Agriculture; 2013.

10. Bozell, J. J. & Petersen, G. R. Technology development for the production of biobased products from biorefinery carbohydrates—the US Department of Energy's "top 10" revisited. *Green Chem.* **12,** 539-554 (2010).

11. Ravenelle, R. M. et al. Stability of zeolites in hot liquid water. *J. Phys. Chem. C* **114,** 19582-19595 (2010).

12. Chen, B. et al. New developments in hydrogenation catalysis particularly in synthesis of fine and intermediate chemicals. *Appl. Catal., A* **280,** 17-46 (2005).

13. Besson, M., Gallezot, P. & Pinel, C. Conversion of biomass into chemicals over metal catalysts. *Chem. Rev.* **114,** 1827-1870 (2013).

14. Kukula, P. & Červený, L. Preparation of tartaric acid modified raney nickel catalysts: Study of modification procedure. *Appl. Catal., A* **210,** 237-246 (2001).

15. Gardner, D. W., Huo, J., Hoff, T. C., Johnson, R. L., Shanks, B. H. & Tessonnier, J.-P. Insights into the hydrothermal stability of ZSM-5 under relevant biomass conversion reaction conditions. *ACS Catal.* **5,** 4418-4422 (2015).

16. Pham, H. N., Anderson, A. E., Johnson, R. L., Schmidt-Rohr, K. & Datye, A. K. Improved hydrothermal stability of mesoporous oxides for reactions in the aqueous phase. *Angew. Chem. Int. Ed.* **51,** 13163-13167 (2012).

17. Ravenelle, R. M., Copeland, J. R., Kim, W.-G., Crittenden, J. C. & Sievers, C. Structural changes of γ-$Al_2O_3$-supported catalysts in hot liquid water. *ACS Catal.* **1,** 552-561 (2011).

18. Koichumanova, K., Vikla, A. K. K., de Vlieger, D. J. M., Seshan, K., Mojet, B. L. & Lefferts, L. Towards stable catalysts for aqueous phase conversion of ethylene glycol for renewable hydrogen. *ChemSusChem* **6,** 1717-1723 (2013).

19. Kruger, J. S., Nikolakis, V. & Vlachos, D. G. Aqueous-phase fructose dehydration using Brønsted acid zeolites: Catalytic activity of dissolved aluminosilicate species. *Appl. Catal., A* **469,** 116-123 (2014).

20. Pham, H. N., Pagan-Torres, Y. J., Serrano-Ruiz, J. C., Wang, D., Dumesic, J. A. & Datye, A. K. Improved hydrothermal stability of niobia-supported Pd catalysts. *Appl. Catal., A* **397,** 153-162 (2011).

21. Gürbüz, E. I. & Dumesic, J. A. Catalytic strategies and chemistries involved in the conversion of sugars to liquid transportation fuels. In: Behrens M, Datye AK (eds). *Catalysis for the conversion of biomass and its derivatives*, vol. 2: Berlin, Germany, 2013.

22. Vilé, G., Albani, D., Almora-Barrios, N., López, N. & Pérez-Ramírez, J. Advances in the design of nanostructured catalysts for selective hydrogenation. *ChemCatChem* **8,** 21-33 (2016).

23. Gallezot, P. & Richard, D. Selective hydrogenation of α, β-unsaturated aldehydes. *Cat. Rev. - Sci. Eng.* **40,** 81-126 (1998).

24. Barnard, D. R. & Xue, R.-D. Laboratory evaluation of mosquito repellents against aedes albopictus, culex nigripalpus, and ochlerotatus triseriatus (diptera: Culicidae). *J. Med. Entomol.* **41,** 726-730 (2004).

25. Mohr, C. & Claus, P. Hydrogenation properties of supported nanosized gold particles. *Sci. Prog.* **84,** 311-334 (2001).

26. Delbecq, F. & Sautet, P. Competitive C=C and C=O adsorption of α-β unsaturated aldehydes on Pt and Pd surfaces in relation with the selectivity of hydrogenation reactions: A theoretical approach. *J. Catal.* **152,** 217-236 (1995).

27. Jiang, F., Cai, J., Liu, B., Xu, Y. & Liu, X. Particle size effects in the selective hydrogenation of cinnamaldehyde over supported palladium catalysts. *RSC Adv.* **6,** 75541-75551 (2016).

28. Durndell, L. J., Parlett, C. M. A., Hondow, N. S., Isaacs, M. A., Wilson, K. & Lee, A. F. Selectivity control in Pt-catalyzed cinnamaldehyde hydrogenation. *Sci. Rep.* **5,** 9425 (2015).

29. Vu, H. et al. Bimetallic catalysis on carbon nanotubes for the selective hydrogenation of cinnamaldehyde. *J. Catal.* **240,** 18-22 (2006).

30. Zheng, R., Porosoff, M. D., Weiner, J. L., Lu, S., Zhu, Y. & Chen, J. G. Controlling hydrogenation of C=O and C=C bonds in cinnamaldehyde using silica supported Co-Pt and Cu-Pt bimetallic catalysts. *Appl. Catal., A* **419–420,** 126-132 (2012).

31. Qi, X., Axet, M. R., Philippot, K., Lecante, P. & Serp, P. Seed-mediated synthesis of bimetallic ruthenium–platinum nanoparticles efficient in cinnamaldehyde selective hydrogenation. *Dalton Trans.* **43,** 9283-9295 (2014).

32. Plomp, A. J. et al. Catalysts based on platinum–tin and platinum–gallium in close contact for the selective hydrogenation of cinnamaldehyde. *J. Catal.* **263,** 146-154 (2009).

33. Coq, B., Kumbhar, P. S., Moreau, C., Moreau, P. & Warawdekar, M. G. Liquid phase hydrogenation of cinnamaldehyde over supported ruthenium catalysts: Influence of particle size, bimetallics and nature of support. *J. Mol. Catal.* **85,** 215-228 (1993).

34. Kitchin, J. R., Nørskov, J. K., Barteau, M. A. & Chen, J. Role of strain and ligand effects in the modification of the electronic and chemical properties of bimetallic surfaces. *Phys. Rev. Lett.* **93,** 156801 (2004).

35. Liao, F., Lo, T. W. B. & Tsang, S. C. E. Recent developments in palladium-based bimetallic catalysts. *ChemCatChem* **7,** 1998-2014 (2015).

36. Consonni, M., Jokic, D., Yu Murzin, D. & Touroude, R. High performances of Pt/ZnO catalysts in selective hydrogenation of crotonaldehyde. *J. Catal.* **188,** 165-175 (1999).

37. Pradier, C., Birchem, T., Berthier, Y. & Cordier, G. Hydrogenation of 3-methyl-butenal on Pt (110); comparison with Pt (111). *Catal. Lett.* **29,** 371-378 (1994).

38. Serrano-Ruiz, J. C., López-Cudero, A., Solla-Gullón, J., Sepúlveda-Escribano, A., Aldaz, A. & Rodríguez-Reinoso, F. Hydrogenation of α, β unsaturated aldehydes over polycrystalline, (111) and (100) preferentially oriented Pt nanoparticles supported on carbon. *J. Catal.* **253,** 159-166 (2008).

39. Loffreda, D., Delbecq, F., Vigné, F. & Sautet, P. Chemo−regioselectivity in heterogeneous catalysis: Competitive routes for C=O and C=C hydrogenations from a theoretical approach. *J. Am. Chem. Soc.* **128,** 1316-1323 (2006).

40. Xia, Y., Xiong, Y., Lim, B. & Skrabalak, S. E. Shape-controlled synthesis of metal nanocrystals: Simple chemistry meets complex physics? *Angew. Chem. Int. Ed.* **48,** 60-103 (2009).

41. Vu, K. B., Bukhryakov, K. V., Anjum, D. H. & Rodionov, V. O. Surface-bound ligands modulate chemoselectivity and activity of a bimetallic nanoparticle catalyst. *ACS Catal.* **5,** 2529-2533 (2015).

42. Jeong, H., Kim, C., Yang, S. & Lee, H. Selective hydrogenation of furanic aldehydes using Ni nanoparticle catalysts capped with organic molecules. *J. Catal.* **344,** 609-615 (2016).

43. Toebes, M. L. et al. Support effects in hydrogenation of cinnamaldehyde over carbon nanofiber-supported platinum catalysts: Kinetic modeling. *Chem. Eng. Sci.* **60,** 5682-5695 (2005).

44. Solhy, A. et al. MWCNT activation and its influence on the catalytic performance of Pt/MWCNT catalysts for selective hydrogenation. *Carbon* **46,** 1194-1207 (2008).

45. Chizari, K. et al. Tuning of nitrogen-doped carbon nanotubes as catalyst support for liquid-phase reaction. *Appl. Catal., A* **380,** 72-80 (2010).

46. Amadou, J. et al. N-doped carbon nanotubes for liquid-phase C=C bond hydrogenation. *Catal. Today* **138,** 62-68 (2008).

47. Claus, P. Selective hydrogenation of α,β-unsaturated aldehydes and other C=O and C=C bonds containing compounds. *Top. Catal.* **5,** 51-62 (1998).

48. Coloma, F., Sepúlveda-Escribano, A. & Rodríguez-Reinoso, F. Improvement of the selectivity to crotyl alcohol in the gas-phase hydrogenation of crotonaldehyde over platinum/activated carbon catalysts. *Appl. Catal., A* **123,** L1-L5 (1995).

49. Zhai, Y., Dou, Y., Zhao, D., Fulvio, P. F., Mayes, R. T. & Dai, S. Carbon materials for chemical capacitive energy storage. *Adv. Mater.* **23,** 4828-4850 (2011).

50. Su, D. S. & Schlögl, R. Nanostructured carbon and carbon nanocomposites for electrochemical energy storage applications. *ChemSusChem* **3,** 136-168 (2010).

51. Avouris, P. Molecular electronics with carbon nanotubes. *Acc. Chem. Res.* **35,** 1026-1034 (2002).

52. Loh, K. P., Bao, Q., Eda, G. & Chhowalla, M. Graphene oxide as a chemically tunable platform for optical applications. *Nat. Chem.* **2,** 1015-1024 (2010).

53. Cha, C., Shin, S. R., Annabi, N., Dokmeci, M. R. & Khademhosseini, A. Carbon-based nanomaterials: Multifunctional materials for biomedical engineering. *ACS Nano* **7,** 2891-2897 (2013).

54. Leary, R. & Westwood, A. Carbonaceous nanomaterials for the enhancement of $TiO_2$ photocatalysis. *Carbon* **49,** 741-772 (2011).

55. Serp, P. & Figueiredo, J. L. *Carbon materials for catalysis*. John Wiley & Sons, 2009.

56. Stoeckli, H. F. Microporous carbons and their characterization: The present state of the art. *Carbon* **28,** 1-6 (1990).

57. Tessonnier, J. P. & Su, D. S. Recent progress on the growth mechanism of carbon nanotubes: A review. *ChemSusChem* **4,** 824-847 (2011).

58. De Jong, K. P. & Geus, J. W. Carbon nanofibers: Catalytic synthesis and applications. *Cat. Rev. - Sci. Eng.* **42,** 481-510 (2000).

59. Pirard, S. L., Douven, S., Bossuot, C., Heyen, G. & Pirard, J.-P. A kinetic study of multi-walled carbon nanotube synthesis by catalytic chemical vapor deposition using a Fe-Co/$Al_2O_3$ catalyst. *Carbon* **45,** 1167-1175 (2007).

60. Lv, R. et al. Open-ended, N-doped carbon nanotube–graphene hybrid nanostructures as high-performance catalyst support. *Adv. Funct. Mater.* **21,** 999-1006 (2011).

61. van Dommele, S., de Jong, K. P. & Bitter, J. H. Nitrogen-containing carbon nanotubes as solid base catalysts. *Chem. Commun.* 4859-4861 (2006).

62. Liu, H. et al. Structural and morphological control of aligned nitrogen-doped carbon nanotubes. *Carbon* **48,** 1498-1507 (2010).

63. Serp, P. & Machado, B. *Nanostructured carbon materials for catalysis*. Royal Society of Chemistry, 2015.

64. Boehm, H. P., Diehl, E., Heck, W. & Sappok, R. Surface oxides of carbon. *Angew. Chem. Int. Ed.* **3,** 669-677 (1964).

65. Donnet, J. The chemical reactivity of carbons. *Carbon* **6,** 161-176 (1968).

66. Coughlin, R. W. Carbon as adsorbent and catalyst. *Ind. Eng. Chem. Prod. Res. Dev.* **8,** 12-23 (1969).

67. Haddon, R. Chemistry of the fullerenes: The manifestation of strain in a class of continuous aromatic molecules. *Science* **261,** 1545-1550 (1993).

68. Niyogi, S. et al. Chemistry of single-walled carbon nanotubes. *Acc. Chem. Res.* **35,** 1105-1113 (2002).

69. Haddon, R. Measure of nonplanarity in conjugated organic molecules: Which structurally characterized molecule displays the highest degree of pyramidalization? *J. Am. Chem. Soc.* **112,** 3385-3389 (1990).

70. Haddon, R. C. π-electrons in three dimensiona. *Acc. Chem. Res.* **21,** 243-249 (1988).

71. Lusk, M. T. & Carr, L. D. Nanoengineering defect structures on graphene. *Phys. Rev. Lett.* **100,** 175503 (2008).

72. Allemand, P. et al. Two different fullerenes have the same cyclic voltammetry. *J. Am. Chem. Soc.* **113,** 1050-1051 (1991).

73. Haddon, R., Palmer, R., Kroto, H. & Sermon, P. The fullerenes: Powerful carbon-based electron acceptors. *Philos. Trans. Royal Soc. A* **343,** 53-62 (1993).

74. Suenaga, K., Wakabayashi, H., Koshino, M., Sato, Y., Urita, K. & Iijima, S. Imaging active topological defects in carbon nanotubes. *Nat. Nanotechnol.* **2,** 358-360 (2007).

75. Lee, S. M., Lee, Y. H., Hwang, Y. G., Hahn, J. R. & Kang, H. Defect-induced oxidation of graphite. *Phys. Rev. Lett.* **82,** 217-220 (1999).

76. Bom, D. et al. Thermogravimetric analysis of the oxidation of multiwalled carbon nanotubes: Evidence for the role of defect sites in carbon nanotube chemistry. *Nano Lett.* **2,** 615-619 (2002).

77. Ajayan, P., Ebbesen, T., Ichihashi, T., Iijima, S., Tanigaki, K. & Hiura, H. Opening carbon nanotubes with oxygen and implications for filling. *Nature* **362,** 522-525 (1993).

78. Tsang, S. C., Harris, P. J. F. & Green, M. L. H. Thinning and opening of carbon nanotubes by oxidation using carbon dioxide. *Nature* **362,** 520-522 (1993).

79. Radovic, L. R., Silva-Tapia, A. B. & Vallejos-Burgos, F. Oxygen migration on the graphene surface. 1. Origin of epoxide groups. *Carbon* **49,** 4218-4225 (2011).

80. Radovic, L. R., Suarez, A., Vallejos-Burgos, F. & Sofo, J. O. Oxygen migration on the graphene surface. 2. Thermochemistry of basal-plane diffusion (hopping). *Carbon* **49,** 4226-4238 (2011).

81. Gómez-Navarro, C. et al. Atomic structure of reduced graphene oxide. *Nano Lett.* **10,** 1144-1148 (2010).

82. Brodie, B. C. On the atomic weight of graphite. *Philos. Trans. Royal Soc.* **149,** 249-259 (1859).

83. Staudenmaier, L. Verfahren zur darstellung der graphitsäure. *Eur. J. Inorg. Chem.* **31,** 1481-1487 (1898).

84. Hummers Jr, W. S. & Offeman, R. E. Preparation of graphitic oxide. *J. Am. Chem. Soc.* **80,** 1339-1339 (1958).

85. Mawhinney, D. B., Naumenko, V., Kuznetsova, A., Yates, J. T., Liu, J. & Smalley, R. E. Infrared spectral evidence for the etching of carbon nanotubes: Ozone oxidation at 298 K. *J. Am. Chem. Soc.* **122,** 2383-2384 (2000).

86. Bubert, H., Brandl, W., Kittel, S., Marginean, G. & Toma, D. Analytical investigation of plasma-treated carbon fibres. *Anal. Bioanal. Chem.* **374,** 1237-1241 (2002).

87. Xia, W., Jin, C., Kundu, S. & Muhler, M. A highly efficient gas-phase route for the oxygen functionalization of carbon nanotubes based on nitric acid vapor. *Carbon* **47,** 919-922 (2009).

88. Charlier, J.-C. Defects in carbon nanotubes. *Acc. Chem. Res.* **35,** 1063-1069 (2002).

89. Brunelle, J. Preparation of catalysts by metallic complex adsorption on mineral oxides. *Pure Appl. Chem.* **50,** 1211-1229 (1978).

90. Kühn, F. E. *Catalysis. From principles to applications.* Wiley Online Library, 2013.

91. Schlögl, R., Che, M., Clause, O. & Marchilly, C. *Preparation of solid catalysts*. Wiley-VCH: Weinhein, 1999.

92. Suh, D. J., Tae-Jin, P. & Son-Ki, I. Effect of surface oxygen groups of carbon supports on the characteristics of Pd/C catalysts. *Carbon* **31,** 427-435 (1993).

93. Prado-Burguete, C., Linares-Solano, A., Rodríguez-Reinoso, F. & de Lecea, C. S.-M. The effect of oxygen surface groups of the support on platinum dispersion in Pt/carbon catalysts. *J. Catal.* **115,** 98-106 (1989).

94. Rodríguez-reinoso, F. The role of carbon materials in heterogeneous catalysis. *Carbon* **36,** 159-175 (1998).

95. Matsubu, J. C. et al. Adsorbate-mediated strong metal–support interactions in oxide-supported rh catalysts. *Nat. Chem.* **9,** 120-127 (2016).

96. Lykhach, Y. et al. Counting electrons on supported nanoparticles. *Nat. Mater.* **15,** 284-288 (2016).

97. Ahmadi, M., Mistry, H. & Roldan Cuenya, B. Tailoring the catalytic properties of metal nanoparticles via support interactions. *J. Phys. Chem. Lett.* **7,** 3519-3533 (2016).

98. Arunajatesan, V. C., B.; Möbus, K.; Ostgard, D. J.; Tacke, T.; Wolf, D. *Carbon materials for catalysis- carbon-supported catalysts for the chemical industry*. John Wiley & Sons: Hoboken, 2009.

99. Perathoner, S., Ampelli, C., Chen, S., Passalacqua, R., Su, D. & Centi, G. Photoactive materials based on semiconducting nanocarbons – a challenge opening new possibilities for photocatalysis. *J. Energy Chem.* **26,** 207-218 (2017).

100. Xia, W. Interactions between metal species and nitrogen-functionalized carbon nanotubes. *Catal. Sci. Tech.* **6,** 630-644 (2016).

101. Su, D. S., Perathoner, S. & Centi, G. Nanocarbons for the development of advanced catalysts. *Chem. Rev.* **113,** 5782-5816 (2013).

102. Dong Jin, S., Tae-Jin, P. & Son-Ki, I. Effect of surface oxygen groups of carbon supports on the characteristics of Pd/C catalysts. *Carbon* **31,** 427-435 (1993).

103. Gurrath, M., Kuretzky, T., Boehm, H. P., Okhlopkova, L. B., Lisitsyn, A. S. & Likholobov, V. A. Palladium catalysts on activated carbon supports: Influence of reduction temperature, origin of the support and pretreatments of the carbon surface. *Carbon* **38,** 1241-1255 (2000).

104. Toebes, M. L., Prinsloo, F. F., Bitter, J. H., van Dillen, A. J. & de Jong, K. P. Influence of oxygen-containing surface groups on the activity and selectivity of carbon nanofiber-supported ruthenium catalysts in the hydrogenation of cinnamaldehyde. *J. Catal.* **214,** 78-87 (2003).

105. Tessonnier, J.-P., Pesant, L., Ehret, G., Ledoux, M. J. & Pham-Huu, C. Pd nanoparticles introduced inside multi-walled carbon nanotubes for selective hydrogenation of cinnamaldehyde into hydrocinnamaldehyde. *Appl. Catal., A* **288,** 203-210 (2005).

106. Plomp, A. J., Vuori, H., Krause, A. O. I., de Jong, K. P. & Bitter, J. H. Particle size effects for carbon nanofiber supported platinum and ruthenium catalysts for the selective hydrogenation of cinnamaldehyde. *Appl. Catal., A* **351,** 9-15 (2008).

107. Zheng, Y. et al. Hydrogen evolution by a metal-free electrocatalyst. *Nat. Commun.* **5,** 3783 (2014).

108. Ito, Y., Cong, W., Fujita, T., Tang, Z. & Chen, M. High catalytic activity of nitrogen and sulfur co-doped nanoporous graphene in the hydrogen evolution reaction. *Angew. Chem. Int. Ed.* **54,** 2131-2136 (2015).

109. Cuong, N. T., Fujiwara, A., Mitani, T. & Chi, D. H. Effects of carbon supports on Pt nano-cluster catalyst. *Comput. Mater. Sci.* **44,** 163-166 (2008).

110. Efremenko, I. & Sheintuch, M. Carbon-supported palladium catalysts. Molecular orbital study. *J. Catal.* **214,** 53-67 (2003).

111. Gao, W., Mueller, J. E., Anton, J., Jiang, Q. & Jacob, T. Nickel cluster growth on defect sites of graphene: A computational study. *Angew. Chem. Int. Ed.* **52,** 14237-14241 (2013).

112. Menon, M., Andriotis, A. N. & Froudakis, G. E. Curvature dependence of the metal catalyst atom interaction with carbon nanotubes walls. *Chem. Phys. Lett.* **320,** 425-434 (2000).

113. Sanz-Navarro, C. F. et al. Molecular dynamics simulations of carbon-supported ni clusters using the reax reactive force field. *J. Phys. Chem. C* **112,** 12663-12668 (2008).

114. Sanz-Navarro, C. F., Åstrand, P.-O., Chen, D., Rønning, M., van Duin, A. C. & Goddard III, W. A. Molecular dynamics simulations of metal clusters supported on fishbone carbon nanofibers. *J. Phys. Chem. C* **114,** 3522-3530 (2010).

115. Sanz-Navarro, C. F. et al. Molecular dynamics simulations of the interactions between platinum clusters and carbon platelets. *J. Phys. Chem. A* **112,** 1392-1402 (2008).

116. Yoon, Y., Rousseau, R., Weber, R. S., Mei, D. & Lercher, J. A. First-principles study of phenol hydrogenation on Pt and Ni catalysts in aqueous phase. *J. Am. Chem. Soc.* **136,** 10287-10298 (2014).

117. Rinaldi, A. et al. Dissolved carbon controls the initial stages of nanocarbon growth. *Angew. Chem. Int. Ed.* **50,** 3313-3317 (2011).

118. Wang, X., Li, N., Webb, J. A., Pfefferle, L. D. & Haller, G. L. Effect of surface oxygen containing groups on the catalytic activity of multi-walled carbon nanotube supported Pt catalyst. *Appl. Catal., B* **101,** 21-30 (2010).

# CHAPTER 2

# CONSIDERATIONS FOR INVESTIGATING METAL-SUPPORT INTERACTIONS: DIFFUSION LIMITATIONS IN BATCH AND FLOW REACTORS

## 2.1 Introduction

Metal-support interactions and their effect on catalytic activity are challenging to investigate due to the possible contribution of experimental artifacts (*e.g.* diffusion limitations) to the observed reactivity trends. To address this issue, it is advisable to first identify experimental conditions under which the internal and external mass transfers of the reactants to the active sites do not limit the kinetics of the reaction. For liquid-phase hydrogenation reactions, these limitations are typically associated with the poor solubility of hydrogen in the solvent. The rate of the reaction is then controlled by the availability of hydrogen, which makes it challenging to accurately compare the activity of the investigated catalysts. To address this issue, it is common to run the hydrogenation reactions in high pressure batch or packed bed reactors to increase the mole fraction of hydrogen dissolved in the liquid phase. However, this approach comes with a major tradeoff in the case of palladium catalysts as it is well-established that hydrogen dissolves in the palladium lattice at high pressure to form the β-hydride phase. The reactivity of surface (α-hydride) and sub-surface (β-hydride) hydrogen atoms is drastically different. For example, in the case of the selective hydrogenation of alkynes to alkenes, surface hydrogen was shown to selectively hydrogenate the carbon-carbon triple bond to the desired alkene double bond. In contrast, sub-surface hydrogen leads to the over-hydrogenated alkane.[1] This adds another layer of complexity when investigating metal-support interactions for Pd/C as the support may

influence the formation and the reactivity of the two hydrides differently. Therefore, we were confronted to a dilemma at the beginning of this project: chemical engineering principles motivated us to use a high pressure packed bed reactor for addressing mass transfer limitations while materials science considerations encouraged us to keep the hydrogen pressure low to prevent the formation of the β-hydride phase.

In this chapter, we apply chemical engineering principles to estimate the effects of internal and external mass transfers for two reactor configurations: a low pressure (1 bar) batch reactor and a high pressure (5 bar) packed bed flow reactor. These calculations were used to guide the experimental work throughout this thesis.

## 2.2 Batch Reactors: Internal Mass Transfer Effects

Cinnamaldehyde hydrogenation was used as the probe reaction to investigate the differences in performance of catalysts throughout this doctoral work. These hydrogenation tests were first conducted in a three-neck round bottom flask glass reactor using experimental conditions reported by other groups.[2] 100 mg of the 5 wt% Pd on carbon catalyst was added to the reactor with 40 ml dioxane (99.8% purity, Sigma-Aldrich) and 365 mg decane (internal standard; ≥ 99% purity, Sigma-Aldrich) along with a stir bar. The flask was then connected to a condenser maintained at 4 °C to allow the re-condensation of the dioxane vapors formed upon heating and thereby minimize solvent losses during the reaction. The reactor was placed in an oil bath and stirred at 500 rpm. Initially, the bath temperature was maintained at room temperature using an IKA-RCT magnetic stir plate equipped with a PT1000 thermocouple. Bronkhorst mass flow controllers and a fine frit (10 – 20 μm porosity) were used to control gas flows to the reactor. The reactor was purged with nitrogen gas at 20 ml $min^{-1}$ for 20 min

at room temperature to remove any oxygen dissolved in the solvent. Following this, the temperature of the oil bath was ramped to 80 °C and simultaneously the gas flow was switched to hydrogen at 20 ml $min^{-1}$ at ambient pressure for 30 min. 5 g of cinnamaldehyde was dissolved in 10 ml of dioxane and added to the reactor using the third neck, which was fitted with a rubber septum and a syringe needle. This addition of cinnamaldehyde marked the start time of the reaction. The hydrogen flow rate was maintained at 20 ml $min^{-1}$ under ambient pressure throughout the experiment. 200 µl samples were withdrawn every 15 min, collected in pre-cooled glass vials, and refrigerated immediately to quench the reaction and prevent solvent losses. All catalytic tests were conducted in triplicates.

The reaction samples were diluted 15 times with dioxane and filtered using 0.22 µm nylon filters. 1 µl of this diluted sample was then injected in an Agilent 7890 A gas chromatograph (GC) equipped with an HP-5 column (30 m X 320 µm X 0.25 µm) and a flame ionization detector (FID). A split ratio of 20:1 at 20 ml $min^{-1}$, inlet heater temperature of 300 °C, total flow of 24 ml $min^{-1}$, septum purge flow of 3 ml $min^{-1}$, and column flow of 1 ml $min^{-1}$ were used. The initial temperature of the oven was maintained at 40 °C for 1 min and then increased to 180 °C with a ramp rate of 10 °C $min^{-1}$. The temperature of the FID heater was maintained at 300 °C.

Stacked cup carbon nanotube (SCCNT) catalyst support is represented by a cylindrical geometry as depicted in Figure 1. Component A is hydrogen and B is cinnamaldehyde. The molar fluxes of the components A and B are represented by $N_A$ and $N_B$ respectively. The length of the SCCNT is represented by L and its inner radius is represented by R.

The following assumptions were made while conducting the internal mass transfer analysis: i) concentration of component A ($C_A$) and concentration of component B ($C_B$) is constant in the radial direction, ii) reaction only occurs on the catalyst surface, and iii) the system is under steady state.

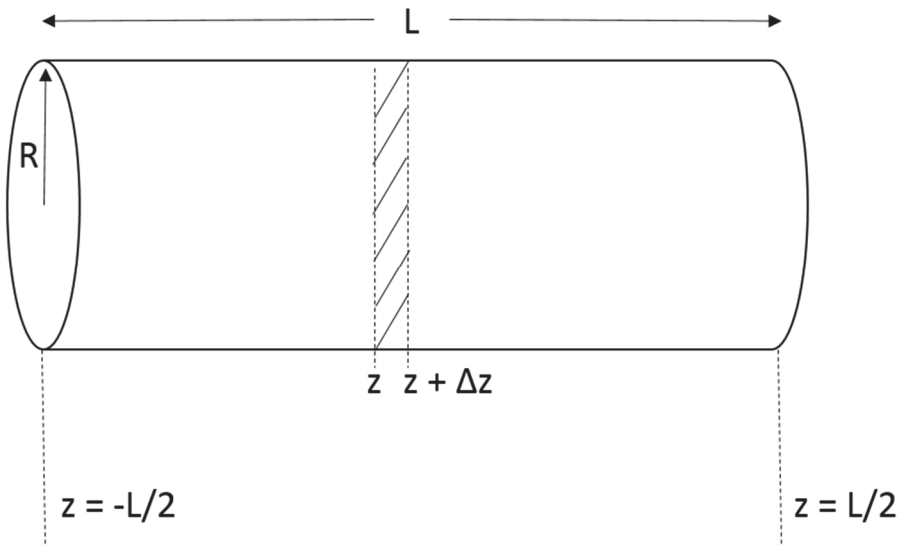


Figure 1. Representation of the cylindrical stacked cup carbon nanotube of length L and inner radius R.

Based on the kinetic trace of the reaction (Figure 2), which depicts a straight-line plot for the change in cinnamaldehyde concentration with time, the reaction was assumed to be $0^{th}$ order with respect to cinnamaldehyde. The reaction was considered to be $1^{st}$ order with respect to hydrogen, based on the common assumption for this reaction as reported in the literature.[11]

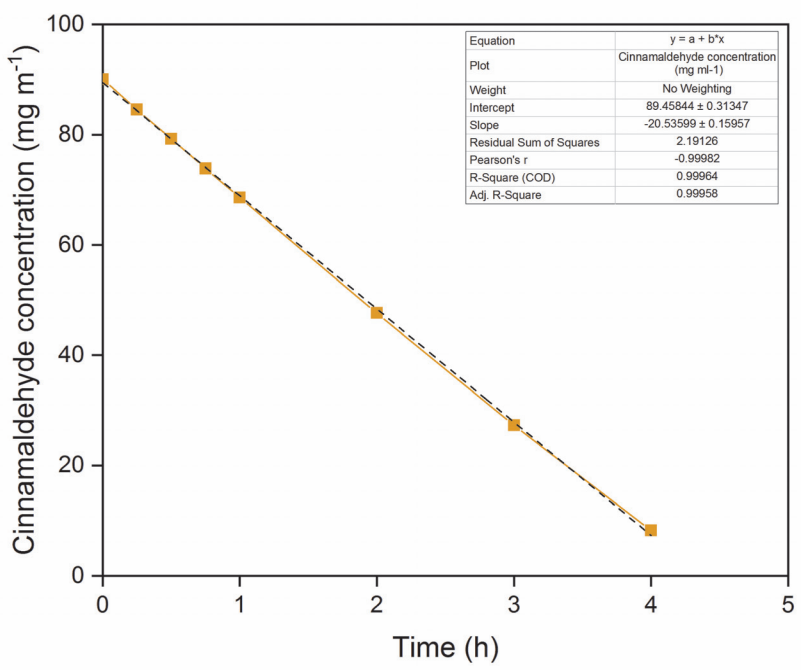


Figure S2. Catalytic trace for palladium catalyst supported on pyrolytically stripped SCCNTs conducted at 80 °C, stirring rate = 500 rpm, hydrogen flow rate = 20 ml $min^{-1}$, mass of catalyst = 100 mg, and mass of cinnamaldehyde = 5 g.

Mass balance analysis on component A is represented by equation 1:

$$(\pi R^2 N_A)\big|_z - (\pi R^2 N_A)\big|_{z+\Delta z} - k_a C_A 2\pi R \Delta z = 0 \quad (1)$$

Divide by πRΔz and take limit of Δz tending to 0, to obtain equation 2:

$$-R\frac{dN_A}{dz} - 2k_a C_A = 0 \quad (2)$$

Fick's law for molar flux of component A is defined in equation 3:

$$N_A = -D_A \frac{dC_A}{dz} \quad (3)$$

where, $D_A$ is the effective diffusion coefficient of the reactant A, which is hydrogen.

Substituting equation 3 in equation 2, we obtain equation 4:

$$RD_A \frac{d^2 C_A}{dz^2} - 2k_a C_A = 0 \quad (4)$$

where, $k_a$ is the reaction rate constant based on catalyst surface area.

In order to non-dimensionalize the equation, we define the following parameters:

$$y = \frac{C_A}{C_{AS}} \tag{5}$$

where, $C_{AS}$ is the concentration of the reactant A in the bulk of the solvent.

$$x = \frac{z}{L} \tag{6}$$

Using the parameters defined in equation 5 and 6, equation 4 can be written as:

$$RD_A \frac{C_{AS}}{L^2} \frac{d^2y}{dx^2} - 2k_a C_{AS} y = 0 \tag{7}$$

Rearranging terms to obtain:

$$\frac{d^2y}{dx^2} - \frac{2k_a L^2}{RD_A} y = 0 \tag{8}$$

We now define the Thiele modulus ($\varphi^2$), as follows:

$$\varphi^2 = \frac{2k_a L^2}{RD_A} \tag{9}$$

Substituting equation 9 in equation 8, we obtain:

$$\frac{d^2y}{dx^2} - \varphi^2 y = 0 \tag{10}$$

The solution to the differential equation described above is as follows:

$$y = c_2 \sinh(\varphi x) + c_1 \cosh(\varphi x) \tag{11}$$

The boundary conditions for this system can be defined as follows: at $x = 0$, $\frac{dy}{dx} = 0$ and at $x = \frac{1}{2}$, $y = 1$. Using these boundary conditions and the equation 11 can be written as follows:

$$y = \operatorname{sech}\left(\frac{\varphi}{2}\right) \cosh(\varphi x) \tag{12}$$

Effectiveness factor (η) is defined as the ratio of the actual rate of the reaction to the rate of reaction with no diffusion limitations, as represented below:

$$\eta = \frac{D_A \pi R^2 \left(\frac{dC_A}{dz}\right) \Big|_{z=\frac{L}{2}}}{k_a C_{AS} 2\pi R \frac{L}{2}} \tag{13}$$

Non-dimensionalizing equation 13 using the parameters defined in equation 5 and 6, and the Thiele modulus as defined in equation 9, we obtain:

$$\eta = \frac{2}{\varphi^2}\left(\frac{dy}{dx}\right) \Big|_{x=\frac{1}{2}} \tag{14}$$

Differentiating equation 12 with respect to x, we obtain:

$$\left(\frac{dy}{dx}\right) \Big|_{x=\frac{1}{2}} = \operatorname{sech}\left(\frac{\varphi}{2}\right) \varphi \sinh\left(\frac{\varphi}{2}\right) \tag{15}$$

Substituting equation 15 in equation 14, we obtain the effectiveness factor to be as follows:

$$\eta = \frac{2}{\varphi} \tanh\left(\frac{\varphi}{2}\right) \tag{16}$$

To calculate the Thiele modulus using equation 9, the value of $k_a$ was calculated by multiplying the $k_v$, the rate constant based on catalyst volume, which was obtained from the catalytic data, with the characteristic length, a, defined as follows:

$$a = \frac{Volume}{Surface\ area} \tag{17}$$

For a tubular catalyst, volume of the inner pore is $\pi R^2 L$ and the inner surface area of the pore open on both ends is $2\pi RL$. This results in the characteristic length of R/2. The values for the inner radius of the tube and the length were obtained to be 17.5 nm and 10 μm, respectively, from the literature.[12] Therefore, the value of a was 8.75 nm.

$k_v$ was obtained to be 1.07 $s^{-1}$ from the kinetic data and multiplying the $k_v$ with a, the value of $k_a$ was obtained to be $9.3625 \times 10^{-9}$ m $s^{-1}$. The effective diffusion coefficient for

hydrogen was taken to be 8.4 x $10^{-9}$ $m^2$ $s^{-1}$ based on the calculations reported by Toebes et al.[13]

Substituting these values in equation 9, the Thiele modulus ($\varphi^2$) was estimated to be 0.013. The effectiveness factor (η) was estimated to be 0.999 using equation 16 and the above obtained value of $\varphi^2$. This combination of the Thiele modulus and effectiveness factor confirms that the reaction is not mass transfer limited in hydrogen under the conditions used in this study.

For studying the internal mass transfer limitations on component B, which is cinnamaldehyde, mass balance was conducted using equation 18:

$$(\pi R^2 N_B)\big|_z - (\pi R^2 N_B)\big|_{z+\Delta z} - k_a C_A 2\pi R \Delta z = 0 \tag{18}$$

Divide by πRΔz and take limit of Δz tending to 0, to obtain equation 19:

$$-R\frac{dN_B}{dz} - 2k_a C_A = 0 \tag{19}$$

Fick's law for molar flux of component B is defined in equation 20:

$$N_B = -D_B \frac{dC_B}{dz} \tag{20}$$

where, $D_B$ is the effective diffusion coefficient of the reactant B, which is cinnamaldehyde. Substituting equation 20 in equation 19, we obtain equation 21:

$$RD_B \frac{d^2 C_B}{dz^2} - 2k_a C_A = 0 \tag{21}$$

Using equation 5 and 12 and using the value of $\varphi^2$ of 0.013 as obtained earlier, $C_A$ was obtained to be:

$$C_A = C_{AS}\cosh\left(\frac{0.114z}{L}\right) \tag{22}$$

Substituting equation 22 in 21, we obtain:

$$RD_B \frac{d^2 C_B}{dz^2} - 2k_a\, C_{AS} \cosh\left(\frac{0.114z}{L}\right) = 0 \tag{23}$$

In order to non-dimensionalize the equation, we define the following parameter:

$$\alpha = \frac{C_B}{C_{BS}} \tag{24}$$

where, $C_{BS}$ is the concentration of the reactant B in the bulk of the solvent.

Using the parameters defined in equation 6 and 24, equation 23 can be written as:

$$RD_B \frac{C_{BS}}{L^2} \frac{d^2\alpha}{dx^2} - 2k_a C_{AS} \cosh(0.114x) = 0 \tag{25}$$

Rearranging terms to obtain:

$$\frac{d^2\alpha}{dx^2} - \frac{2k_a L^2 C_{AS}}{RD_B C_{BS}} \cosh(0.114x) = 0 \tag{26}$$

We now define the Thiele modulus ($\varphi'^2$), as follows:

$$\varphi'^2 = \frac{2k_a L^2 C_{AS}}{RD_B C_{BS}} \tag{27}$$

Substituting equation 27 in equation 26, we obtain:

$$\frac{d^2\alpha}{dx^2} - \varphi'^2 \cosh(0.114x) = 0 \tag{28}$$

The solution to the differential equation described above is as follows:

$$\alpha = \frac{\varphi'^2 \cosh(0.114x)}{(0.114)^2} + c_2 x + c_1 \tag{29}$$

The boundary conditions for this system can be defined as follows: at $x = 0$, $\frac{d\alpha}{dx} = 0$ and at $x = \frac{1}{2}$, $\alpha = 1$. Using these boundary conditions and the equation 29 can be written as follows:

$$\alpha = 1 - 77.0718\varphi'^2 + \frac{\varphi'^2 \cosh(0.114x)}{(0.114)^2} \tag{30}$$

To calculate the value of $\varphi'^2$, $C_{AS}$ was estimated using the following equation obtained from the literature (Equation 3):[14]

$$\ln x_1 = -5.7347 - \frac{8.6743}{\frac{T}{100\ K}} \tag{31}$$

where, $x_1$ is the mole fraction of hydrogen in dioxane and T is the temperature of the solubility test in K.

Using equation (31), the mole fraction of hydrogen in dioxane at 80 °C was estimated to be 2.77 x $10^{-4}$.[14] This mole fraction represents a concentration of 6.47 x $10^{-6}$ g $ml^{-1}$ of hydrogen in dioxane. The concentration of cinnamaldehyde at 0% conversion was known based on the amount of reactant added and confirmed using the GC-FID analysis to be 90 mg $ml^{-1}$. At 10% conversion, the concentration of cinnamaldehyde was 81 mg $ml^{-1}$. The effective diffusion coefficient for cinnmaldehyde was taken to be 2 x $10^{-9}$ $m^2$ $s^{-1}$ based on the calculations reported by Toebes et al.[13] With the help of these values and equation 27, the Thiele modulus was estimated to be 3.846 x $10^{-6}$ and 4.273 x $10^{-6}$ at 0 and 10% conversion, respectively.

The effectiveness factor (η') is defined as the ratio of the actual rate of the reaction to the rate of reaction with no diffusion limitations, as represented below:

$$\eta' = \frac{D_B \pi R^2 \left(\frac{dC_B}{dz}\right)\Big|_{z=\frac{L}{2}}}{k_a C_{AS} 2\pi R \frac{L}{2}} \tag{32}$$

Non-dimensionalizing equation 32 using the parameters defined in equation 6 and 24, and the Thiele modulus as defined in equation 27, we obtain:

$$\eta' = \frac{2}{\varphi'^2}\left(\frac{d\alpha}{dx}\right)\Big|_{x=\frac{1}{2}} \tag{33}$$

Differentiating equation 30 with respect to x, we obtain:

$$\left(\frac{d\alpha}{dx}\right)\Big|_{x=\frac{1}{2}} = \frac{\varphi'^{2}\ 0.114\ \sinh(0.057)}{(0.114)^2} \tag{34}$$

Substituting equation 34 in equation 33, we obtain the effectiveness factor to be as follows:

$$\eta' = 2\frac{\sinh(0.057)}{0.114} \tag{35}$$

The effectiveness factor was obtained to be 1 for the values of $\varphi'^{2}$ of 3.846 x $10^{-6}$ and 4.273 x $10^{-6}$ at 0 and 10% conversion, respectively. This combination of the Thiele modulus and effectiveness factor confirms that the reaction is not mass transfer limited in cinnmaldehyde under the conditions used in this study.

**2.3 Batch Reactors: External Mass Transfer Effects**

The effects of external mass transfer in the batch reactor were estimated using the mass transfer Biot number ($Bi_m$), which allows us to compare the pore diffusion and film diffusion effects. The $Bi_m$ was estimated with the following equation:[15]

$$\mathrm{Bi_m} = \frac{\mathrm{k_m a}}{\mathrm{D_A}} \tag{36}$$

where, $k_m$ is the mass transfer coefficient and $D_A$ is the effective diffusion coefficient of reactant A.

The value of a was obtained from equation 17 but this time using the external surface area and volume of the SCCNTs. The value of the outer radius of the tube was obtained to be 40 nm resulting in the characteristic length of 20 nm.

As the value of a and $D_A$ are already known, $k_m$ is the only unknown in the equation for calculating the $Bi_m$. The value of $k_m$ was estimated using the Sherwood number (Sh) based on the Churchill Bernstein equation, as described below:

$$\mathrm{Sh} = 0.3 + \frac{0.62\mathrm{Re}^{\frac{1}{2}}\,\mathrm{Sc}^{\frac{1}{3}}}{\left[1+\left(\frac{0.4}{\mathrm{Sc}}\right)^{\frac{2}{3}}\right]^{\frac{1}{4}}}\left[1+\left(\frac{\mathrm{Re}}{282000}\right)^{\frac{5}{8}}\right]^{\frac{4}{5}} = \frac{k_m a}{D} \qquad (37)$$

where, Re is the Reynolds number, Sc is the Schmidt number, and D is the mass diffusivity.

This equation is applicable to a large range of Reynolds (Re) and Schmidt (Sc) numbers (Re.Sc > 0.4), as reported in previous studies.[16] The Re was estimated using the following equation:

$$\mathrm{Re} = \frac{\rho v L_c}{\mu} \qquad (38)$$

where, ρ is the density of dioxane, v is the linear velocity of the agitator tip = angular velocity of the agitator (ω) x radius of the agitator (r'), $L_c$ is the agitator diameter, and μ is the dynamic viscosity of dioxane.

The value of ρ and μ for dioxane at 298.15 K was taken to be 1028 kg $m^{-3}$ and 1.177 kg $m^{-1}$ $s^{-1}$, as reported in the literature.[17] The stir bar used in the experiment was cylindrical in shape with a diameter of 0.75 cm and a length of 2.5 cm. Using these dimensions, the Lc was estimated to be 0.1875 x $10^{-2}$ m and the v was obtained to be 0.049 rad m $s^{-1}$ for a stirring speed of 500 rpm. Substituting these values in equation 38, the Re was estimated to be 53.46.

Based on literature data, Sc for liquid-phase is expected to be in the range of $10^2$ to $10^4$ and the mass diffusivities are expected to be in the range of $10^{-9}$.[17-18] With the help of these values and the estimates for $D_A$ and $D_B$ as obtained earlier from the literature, the $Bi_m$ was calculated. The $Bi_m > 1$ and of $\varphi'^2 < 1$ for all values of Re > 53.46. This confirmed that the reaction was not externally mass transfer limited in hydrogen or cinnamaldehyde.

**2.4 Flow Reactors: Internal Mass Transfer Effects**

The batch reactor used in this study consists of a glass round bottom flask set-up, which results in limitations in hydrogen pressure and flow rate. In order to overcome this challenge, a three-phase packed bed upflow reactor was designed. Herein, the gas flow rate was controlled using a Brooks SLA 5850 mass flow controller connected to a Brooks 0254 control unit. The liquid flow rate was controlled using a Lab Alliance Series II HPLC PEEK pump. The PEEK material of the pump was specifically chosen due to challenges associated with the compatibility of the reactant mixture components and the stainless steel pump heads. A cinnamaldehyde concentration of 100 mg/ml in dioxane, with decane as internal standard, and a hydrogen gas pressure of 5 bar were utilized for flow reactor catalytic tests. The reactor bed temperature was maintained at 80 °C using a metallic block for uniform distribution of heat, wrapped with a HTS Amptek Mono Heating Tape (208 Watts and 120 Volts), and regulated using a Type K thermocouple connected to a CSI32K benchtop temperature controller. The reactor was connected to a condenser maintained at 4 °C to avoid evaporation of solvent. 6 ml liquid samples were collected in 20 ml glass vials. The reaction samples were diluted 15 times in dioxane, filtered using a 0.22 μm nylon filter, and analyzed using the GC-FID, using a similar method as described earlier for the batch experiments.

Stainless steel reactors of 6.5” length, a wall thickness of 0.028”, and an outer diameter of 0.25” were utilized in this study. The beds were packed with 2.5” of silica chips (4-20 mesh size), the catalyst layer, and 2.0” of glass beads (45-90 μm, acid washed with nitric acid to remove metallic impurities). Each layer was alternated with 0.5” of quartz wool to provide separation of the contents and ensure bed packing. The 45-90 μm glass beads were utilized to allow catalyst entrapment under the flow conditions. The commercial 5 wt%

palladium on activated carbon catalyst (Sigma Aldrich) was utilized for this study because it offers a control on the catalyst particle size, a factor that is constrained in the home-made SCCNT catalysts. Prior to use, the catalysts were sieved and the 45-90 μm sieve fraction was utilized for the tests. The average particle diameter and radius for this sieve fraction were calculated to be 67.5 μm and 33.75 μm, respectively.

The effects of internal mass transfer in the flow reactor were studied by estimating the Thiele modulus ($\varphi^2$) and effectiveness factor (η) using similar methods as reported in section 2.2, for spherical catalyst particles. As the particles in this case are spherical, the characteristic length (a) was considered to be equal to the average particle radius of 33.75 μm. The concentration of dissolved hydrogen at 5 bar was estimated to be $3.143 \times 10^{-4}$ g $ml^{-1}$ based on the hydrogen solubility in dioxane at high pressures as reported in the literature.[9] Cinnamaldehyde conversion of ~40% was observed for catalytic tests that were conducted using 15 mg of catalyst, 75 ml $min^{-1}$ of hydrogen flow rate, and 0.6 ml $min^{-1}$ of liquid flow rate. Based on a 40% conversion, the rate of the reaction was estimated to be 13990 g $m^{-3}$ $s^{-1}$. With the help of these parameters, a Thiele modulus of 6.04 and an effectiveness factor of 0.74 was obtained for hydrogen, indicating that the reaction was limited by internal mass transfer for hydrogen. Further, a Thiele modulus of 132.8 and an effectiveness factor of 0.24 were obtained for cinnamaldehyde indicating that the reaction was internal mass transfer limited for cinnamaldehyde as well. The non-internal mass transfer limited regime for the flow reactor system will require future tests with varying catalyst support diameter.

**2.5 Flow Reactors: External Mass Transfer Effects**

In order to obtain reaction conditions that were free from external mass transfer limitations, the gas (G) and liquid (L) flow rates were increased proportionally to the catalyst volume (v). These proportional changes ensured that the space velocity remained constant as the mass flow rate increased.[10] If the reactant conversion does not vary with the mass flow, then it can be safely concluded that the apparent reaction rate is not limited by the external transfers.[10] A pictorial representation of the theoretical method discussed above is depicted in Figure 3. In order to study the effect of external limitation in our reactor system, reactor beds were packed with increasing amounts of catalyst (10, 15, 17.5, 20, and 22.5 mg). Hydrogen gas (50, 75, 87.5, 100, and 112.5 ml $min^{-1}$) and liquid flow rate (0.4, 0.6, 0.7, 0.8, and 0.9 ml $min^{-1}$) were proportionally changed with the increasing catalyst amounts. All the tests were conducted in triplicates. The cinnamaldehyde conversion was measured and plotted against the flow rate (Figure 3). In coherence with the theoretical methods, a combination of 15 mg of catalyst, 75 ml $min^{-1}$ of hydrogen gas flow rate, and a liquid flow rate of 0.6 ml $min^{-1}$ or proportionally higher amounts depicted a non-external mass transfer limited regime (Figure 4).

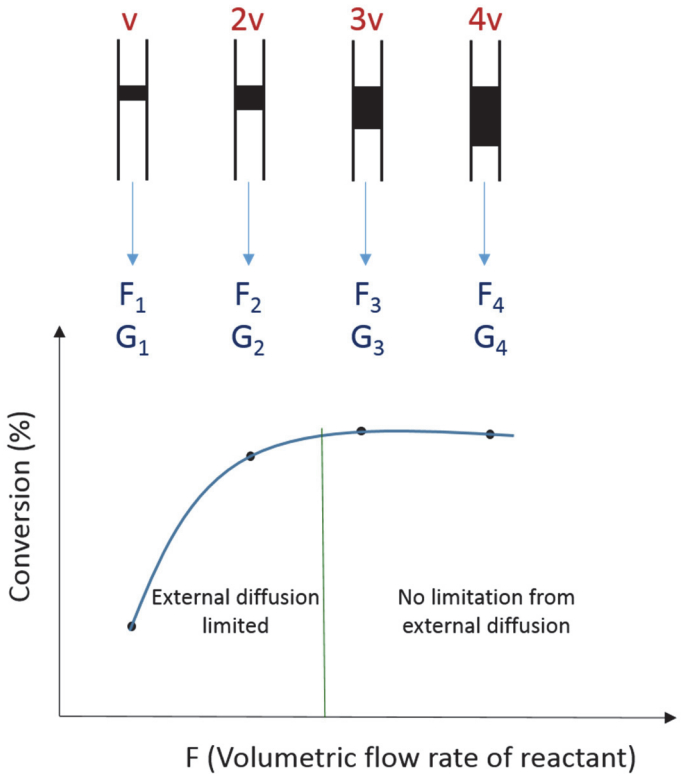


Figure 3. Representation of the theoretical method for detecting a limitation in external mass transfer in a flow reactor.[10]

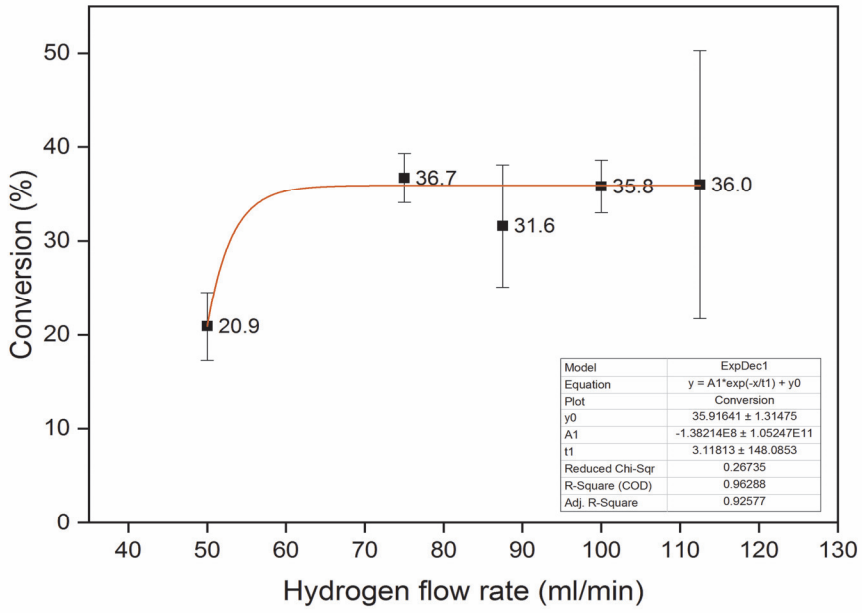


Figure 4. Experimental results for the conversion of CALD with proportional changes in catalyst amount with hydrogen and liquid flow rate.

## 2.6 Conclusions

Detailed analysis of mass transfer effects in the batch reactor under the reaction conditions of interest revealed that the system was free from internal and external diffusion limitations for both hydrogen and cinnamaldehyde. On the other hand, the high pressure flow reactor system was free from external diffusion limitation but it demonstrated internal diffusion limitations for both the reactants under the conditions utilized in this work. These results are counter-intuitive as the mole fraction of dissolved hydrogen increases with the hydrogen pressure and one would expect that the reaction becomes kinetically limited at high pressure. However, at 5 bar the reaction rate increases faster (due to the 1$^{st}$ order of the reaction with respect to hydrogen) than the amount of dissolved hydrogen, causing the reaction to become mass transfer limited.

The ambient pressure batch reactor system was selected for testing the catalytic materials developed in this work due to several reasons. Firstly, the successful elimination of diffusion limitations allowed for a direct comparison of the activity and selectivity of catalysts. Additionally, the low partial pressure of hydrogen in this system prevents the formation of the palladium β-hydride phase, which further simplifies a direct comparison of catalysts. Specifically, the absence of β-hydride ensures that the catalytic performance observed in this work can be correlated with the support properties and is not an artifact due the coexistence of multiple hydride phases.

## 2.7 References

1. Teschner, D. et al. The roles of subsurface carbon and hydrogen in palladium-catalyzed alkyne hydrogenation. *Science* **320,** 86-89 (2008).

2. Tessonnier, J.-P., Pesant, L., Ehret, G., Ledoux, M. J. & Pham-Huu, C. Pd nanoparticles introduced inside multi-walled carbon nanotubes for selective

hydrogenation of cinnamaldehyde into hydrocinnamaldehyde. *Appl. Catal., A* **288,** 203-210 (2005).

3. Tessonnier, J.-P. et al. Analysis of the structure and chemical properties of some commercial carbon nanostructures. *Carbon* **47,** 1779-1798 (2009).

4. Rawlings, J. B. & Ekerdt, J. G. *Chemical reactor analysis and design fundamentals*, 2nd edn, 2012.

5. Zhang, L., Winterbottom, J. M., Boyes, A. P. & Raymahasay, S. Studies on the hydrogenation of cinnamaldehyde over pd/c catalysts. *J. Chem. Technol. Biotechnol.* **72,** 264-272 (1998).

6. *IUPAC solubility data series hydrogen and deuterium*, vol. 5/6, 1981.

7. Toebes, M. L. et al. Support effects in hydrogenation of cinnamaldehyde over carbon nanofiber-supported platinum catalysts: Kinetic modeling. *Chem. Eng. Sci.* **60,** 5682-5695 (2005).

8. Churchill, S. & Bernstein, M. A correlating equation for forced convection from gases and liquids to a circular cylinder in crossflow. *J. Heat Transfer* **99,** 300-306 (1977).

9. Brunner, E. Solubility of hydrogen in 10 organic solvents at 298.15, 323.15, and 373.15 k. *J. Chem. Eng. Data* **30,** 269-273 (1985).

10. Le Page, J. F. *Applied heterogeneous catalysis: Design, manufacture, and use of solid catalysts*, 1988.

# CHAPTER 3

# INTERFACIAL CHARGE DISTRIBUTIONS IN CARBON-SUPPORTED PALLADIUM CATALYSTS

A paper published in Nature Communications

Radhika G. Rao[1,2], Raoul Blume[3], Thomas W. Hansen[4], Erika Fuentes[5], Kathleen Dreyer[6], Simona Moldovan[7], Ovidiu Ersen[7], David D. Hibbitts[6], Yves J. Chabal[5], Robert Schlögl[3] & Jean-Philippe Tessonnier[1,2,*]

[1] Department of Chemical and Biological Engineering, Iowa State University, Ames, IA 50011, USA

[2] NSF Engineering Research Center for Biorenewable Chemicals, Ames, IA 50011, USA

[3] Fritz Haber Institute of the, Max Planck Society, DE-14195 Berlin, Germany

[4] Center for Electron Nanoscopy, Technical University of Denmark, DK-2800 Kgs Lyngby, Denmark

[5] Department of Materials Science and Engineering, University of Texas at Dallas, Richardson, TX 75080, USA

[6] Department of Chemical Engineering, University of Florida, Gainesville, FL 32611, USA

[7] Institut de Physique et Chimie des Matériaux de Strasbourg, UMR 7504 University of Strasbourg – CNRS, FR-67200 Strasbourg, France

[*] Corresponding author

## Abstract

Controlling the charge transfer between a semiconducting catalyst carrier and the supported transition metal active phase represents an elite strategy for fine turning the electronic structure of the catalytic centers, hence their activity and selectivity. These phenomena have been theoretically and experimentally elucidated for oxide supports but

remain poorly understood for carbons due to their complex nanoscale structure. Here, we combine advanced spectroscopy and microscopy on model Pd/C samples to decouple the electronic and surface chemistry effects on catalytic performance. Our investigations reveal trends between the charge distribution at the palladium–carbon interface and the metal's selectivity for hydrogenation of multifunctional chemicals. These electronic effects are strong enough to affect the performance of large (~5 nm) Pd particles. Our results also demonstrate how simple thermal treatments can be used to tune the interfacial charge distribution, hereby providing a strategy to rationally design carbon-supported catalysts.

### 3.1 Introduction

The performance of a catalyst, hence the rate and selectivity of the reaction, can be tailored by controlling the electronic structure of its active sites[1, 2]. Common strategies to achieve the desired properties consist in adjusting the composition, crystallographic structure, particle size, and geometry of the active phase[3, 4, 5]. In homogeneous catalysis, electron-donating and electron-withdrawing ligands provide an additional route to modulate the electronic structure of metal catalysts[6]. Analogous effects where charge density is transferred between the metal and the support are known in heterogeneous catalysis since the 1960s when Schwab explained these phenomena using solid state physics[7, 8]. However, harnessing these electronic metal-support interactions (EMSI) for the rational design of heterogeneous catalysts has proven to be difficult to implement, specifically due to the reconstruction of studied catalysts under reaction conditions that obscure the desired electronic effects[2, 9, 10]. For example, the performance of Pt-group metal nanoparticles supported on reducible oxides was dominated by the partial reduction of the support followed by migration of suboxide

species onto the metal active phase, causing its encapsulation with an impermeable oxide overlayer[10]. Migration of the support onto the metal active phase is widespread for oxide scaffolds and it has created controversies on the possibility to harness charge transfer effects for the rational design of supported catalysts[2, 8, 9, 10, 11, 12]. Yet, several examples suggest that strong interactions with the support could enhance the catalytic performance of transition metals as much as the nature of the metal itself[13].

Carbon supports represent an obvious alternative to oxides to study electronic metal-support interactions and eliminate the challenges associated with atom migration and metal encapsulation[14]. However, a detailed analysis of the literature demonstrates that previous attempts to understand EMSI effects for carbons have failed due to the structural and chemical complexity of the studied materials[15]. Experiments performed on conventional activated carbons and carbon blacks did not permit to decouple electronic, polar, and acid-base interactions, and assess their individual impact on substrate adsorption and activation[16]. The structure-property relationships that link atom hybridization, structure, heteroatom concentration, and functional group composition for the support with electronic structure and catalytic activity of the metal sites are lacking, which are in turn key to establish general rules for rational catalyst design[17, 18].

Despite the challenges in establishing a fundamental understanding of carbon materials as catalyst supports, they are common in heterogeneous catalysis due to their relative inertness compared to conventional oxides. While it is true that carbons do not participate directly in the reaction being catalyzed, these supports can significantly affect the observed activity by altering the adsorption of the reactants. For example, acid-base interactions between $CO_2$ and nitrogen-functionalized carbon supports increased the rate for

$CO_2$ reduction by almost two fold[19]. In other studies, the functionalization of the carbon support with oxygen moieties altered its hydrophilic-hydrophobic character, which in turn modified the reactant's adsorption mode and the selectivity of the reaction[20]. Conversely, electronic effects such as charge transfer between the metal and carbon scaffold were not addressed,[20, 21, 22, 23] although it is now well-established that heteroatoms located at defect sites alter the electronic properties of graphene and graphenic carbons[24, 25]. Specifically, the electronic perturbations caused by nitrogen and sulphur can be significant as inert carbons became catalytically active as a result of the doping process. Recent reviews dedicated to these carbocatalysts demonstrate that their applications are widespread and span from water electrolysis to desulfurization and organic coupling reactions[15, 26]. The effect of functionalization and doping with oxygen on electronic properties has received significantly less attention, probably due to the abundance of oxygen-containing species on carbons materials stored in air and the relative inertness of these materials. Yet, in the photonics field, oxygen was shown to significantly alter the optoelectronic properties of graphene oxide by modulating its band gap[27]. Therefore, conventional carbon supports bearing oxygen functionalities may exhibit electronic properties that remain to be harnessed for catalytic applications.

Here, we demonstrate that the graphitic character and surface functionalization of model carbon supports alter their interaction with palladium (Pd) nanoparticles and affect their selectivity for the hydrogenation of cinnamaldehyde, a model α,β-unsaturated compound. X-ray photoelectron spectroscopy (XPS) using synchrotron radiation shows a charge redistribution at the Pd-carbon interface that is consistent with the observed changes in catalytic activity. Combining spectroscopy, microscopy, and chemisorption techniques

with DFT calculations further reveals a direct relationship between the oxygen concentration at the support's surface, the charge distribution at the Pd-C interface, and the catalytic activity. These results demonstrate that the oxygen functionalities commonly found on carbon-supported catalysts alter both the surface chemistry and electronic properties of the support. The charge depletion layer is large enough to influence the performance of 5 nm Pd nanoparticles although particles of this size are expected to display bulk-like properties. Our results also show that the interfacial charge distribution can be controlled using thermal treatments, thus providing a simple yet powerful method for fine-tuning the performance of the supported metal catalyst.

## 3.2 Results

### 3.2.1 Synthesis of carbon supports with tailored properties

Stacked cup carbon nanotubes (SCCNTs) were strategically chosen as supports due to their reduced structural and chemical complexity compared to conventional activated carbon and carbon black supports. SCCNTs consist of a well-defined tubular structure terminated with a layer of disordered graphenic carbon[28, 29]. This layer offers opportunities to tailor the surface properties through chemical functionalization and high temperature annealing without altering the support's morphology, surface area, and porosity. Hence diffusion and mass transfer for the corresponding catalysts are unaffected by these treatments and their performance can be easily compared[28, 29].

Two series of samples labelled PS-HHT and PS200-PS1000 were prepared to distinguish the effects of graphitization and surface functionalization, respectively. For the first series, SCCNTs were thermally annealed at 700 °C (PS), 1500 °C (LHT), and 3000 °C

(HHT) post synthesis to graphitize the graphenic carbon (Fig. 1)[28]. This process follows the well-established graphitization mechanism demonstrated by Oberlin[30] (*vide infra*). The samples were subsequently treated with nitric acid to remove any inorganic impurities resulting from the synthesis and/or annealing treatment (Supplementary Fig. 3). Raman spectroscopy and C1s XPS confirmed that the graphitic character of the support increased with the treatment temperature, reaching a quasi-graphitic state at 3000 °C (Supplementary Fig. 1 and 2 and Supplementary Table 1). The treatment with nitric acid simultaneously oxidized the surface of the SCCNTs (Supplementary Table 1). For the second series, the PS

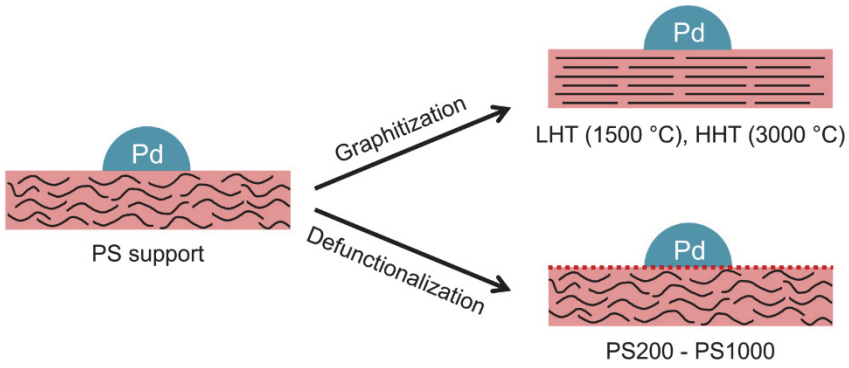


**Figure 1. Schematic representation of the studied catalysts.** The graphitic character and chemistry of the carbon surface were tailored without altering the textural properties of the support, thus enabling an accurate comparison of the catalytic performance of the studied materials. Two sample series were prepared: Pd nanoparticles were deposited onto (a) supports of increasing graphitic character (PS, LHT, HHT), and (b) PS supports partially defunctionalized through annealing at temperatures ranging between 200 °C (PS200) and 1000 °C (PS1000). The color coding matches the colors used in Figure 4, where red represents the carbon support and blue represents the palladium nanoparticles.

sample was partially defunctionalized under inert atmosphere at selected temperatures ranging between 200 °C and 1000 °C (PS200, PS400, PS600, PS800, PS1000). The PS-PS1000 support series thus obtained presented a decreasing concentration of surface oxygen functionalities as demonstrated by the O1s/C1s ratio obtained from XPS, with minor changes

in the graphitic character as confirmed by Raman spectroscopy (Supplementary Table 1). The trends observed for surface functionalization and graphitization with annealing temperature were consistent with previous studies[28, 29, 31]. It is important to note that all the supports displayed uniform textural properties despite the changes in the surface chemistry, which makes them the support material of choice in this work[28].

### 3.2.2 Hydrogenation activity of Pd on SCCNT catalysts

The Pd/SCCNT catalysts were prepared by incipient wetness impregnation of the tailored supports using an aqueous solution of palladium nitrate. This precursor was preferred over other salts as its reduction yields Pd nanoparticles free of any organic and inorganic impurities. The use of surfactants to obtain monodisperse particles was not considered either due to the possible modification of the steric and electronic properties of the metal active sites by the surfactants[32, 33, 34]. The obtained catalysts were tested for the ambient pressure and low temperature (80°C) hydrogenation of cinnamaldehyde (CALD), an α,β-unsaturated aldehyde model compound (Fig. 2, Supplementary Fig. 4). This reaction was selected for its sensitivity to the electronic properties of the metal active phase[35, 36]. Specifically, selectivity towards C=C and/or C=O hydrogenation products was shown to depend on the position of the metal's d band center,[35, 36] which depends on the nature of the metal and alteration of its electronic properties through, for example, alloying or doping. Therefore, this reaction provides an excellent platform for probing metal-support charge transfers.

CALD conversion can proceed via hydrogenation of the C=C bond (hydrocinnamaldehyde, HCALD), C=O bond (cinnamyl alcohol, CALC), or both (3-phenyl propanol, PPL), as shown in Figure 2. Pd catalysts exhibit a higher selectivity for C=C bond

hydrogenation, which is the thermodynamically favored route for this reaction[37]. However, fluctuations in selectivity were observed depending on the support, even among carbon scaffolds. Although attempts have been made in the past to identify the parameters that control the selectivity to HCALD, the role of key factors such as support polarity, metal particle size, and reaction conditions remain intertwined[21, 23].

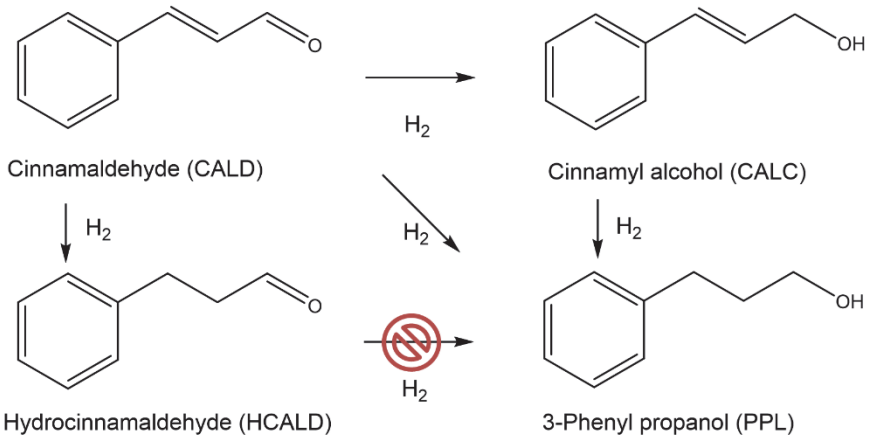


**Figure 2: Reaction scheme for the hydrogenation of cinnamaldehyde.** Reaction pathways for CALD hydrogenation as observed for Pd/C catalysts at 80 °C, 90 mg $ml^{-1}$ of CALD in dioxane, 100 mg catalyst, and 20 ml $min^{-1}$ hydrogen flow rate at ambient pressure. Only two products were formed under the reaction conditions selected in the present study: HCALD through C=C bond hydrogenation, and PPL through a hydrogenation pathway that does not involve HCALD (*i.e.* tests performed with HCALD as the reactant showed no conversion, in agreement with Jiang et. al.[35]). CALC and reaction byproducts were not detected, in agreement with the high (>97%) carbon balance (Supplementary Table 2 and 3).

Significant differences in selectivity were observed for the PS-PS800 sample series (Fig. 3, Supplementary Fig. 5). The observed increase in selectivity to HCALD with the defunctionalization temperature is consistent with previous studies that suggested a correlation exists between selectivity and surface polarity[21, 36]. Non-polar surfaces were proposed to favor the planar (*i.e.* flat) adsorption mode due to interactions between CALD's benzene ring and the delocalized pi system of the carbon support, yielding HCALD through

preferential hydrogenation of the C=C bond. Conversely, polar surfaces were proposed to favor adsorption through the terminal carbonyl functionality, thus enhancing the selectivity to PPL (on Pd) and CALC (on Pt)[21, 36]. While this interpretation is supported by *in situ* FTIR[36], it remains unclear whether the adsorption mode governs the selectivity of the reaction or, instead, is the consequence of a preferential CALD adsorption through the alkene or carbonyl functionality depending on the electronic configuration of the metal. In addition, many studies did not consider the possible contribution of artifacts—variations in the metal loading, particle size, and mass transfer limitations—to the observed trends.

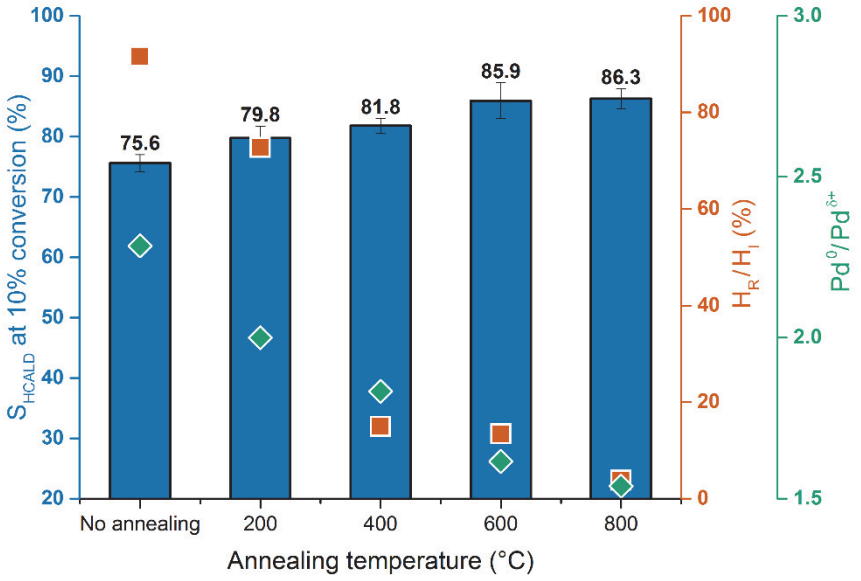


**Figure 3: Effect of carbon supports on catalytic performance.** The bar graph shows the selectivity to HCALD at 10% CALD conversion for Pd supported on the PS support (no annealing) and on PS defunctionalized at 200-800 °C (blue). The values correspond to the average selectivity calculated for three independent experiments ± the corresponding standard deviation (s.d.). The selectivity to HCALD was found to increase with the annealing temperature although the average particle size, metal loading, and normalized reaction rate were within error for the five samples. This trend was consistent with changes in the active metal phase revealed by hydrogen chemisorption (ratio of reversibly to irreversibly

chemisorbed hydrogen $H_R/H_I$, orange) and by XPS (ratio of the Pd 3d5/2 peaks for the metal to δ+ phase, $Pd^0/Pd^{\delta+}$, green).

### 3.2.3 Effect of Pd distribution and mass transfer

Despite the differences in surface oxygen concentration (Supplementary Table 1) and, thereby, in interactions between the carbon surface and Pd precursor, elemental analysis showed a consistent Pd loading of 3.7 ± 0.5 wt% for the PS-PS800 series (Supplementary Table 4). Further, similar particle sizes of 5.0 ± 0.2 nm were measured by hydrogen chemisorption using the double isotherm method (Supplementary Table 5). X-ray diffraction (XRD) and transmission electron microscopy (TEM) provided slightly larger particle sizes, in the order of 5.6 ± 1.3 nm (PS sample) and 6.9 ± 2.7 nm, respectively (Supplementary Table 5). The values obtained were within the error of measurements of the different techniques as observed in other studies as well[38]. The multiple techniques used here allowed us to minimize the limitations and errors intrinsic to each technique and thereby their impact on the interpretation of our results. The similar loading, particle sizes, and particle shapes obtained for all the catalysts indicate that the trends in catalytic performance shown in Figure 3 are not a result of particle size or shape effects (Supplementary Fig. 5, 7 and 8)[35]. Additionally, the trends are not a result of differences in mass transport either as the size, aspect ratio, surface area, and porosity of the supports were not altered by the functionalization and annealing treatments. The Pd/SCCNTs catalysts consist of mesoporous nanotubes,[28, 29] with all the metal particles located on the outer surface and inside the 30 nm mesopore that extends along the main axis of the tube (Supplementary Fig. 6 and 7). In addition, all the selectivities were reported at iso-conversion, which is critical for sequential reactions and also to ensure that the periodic withdrawal of samples has minimal impact on

the selectivity of the catalysts,[39] in coherence with the chemical reaction engineering principles[20, 21].

### 3.2.4 Support effects on the electronic structure of palladium

XPS using both lab and synchrotron radiation was used to examine the effect of the carbon support on the electronic structure of the metal active phase (Fig. 4 and Supplementary Fig. 9 and 10). These two X-ray sources provide photons with very different energies, thus allowing for a depth profiling of the catalysts. Spectra using synchrotron radiation were acquired with photon energies of 1020 eV (survey), 680 eV (O1s), 480 eV (Pd3d) and 425 eV (C1s), and with a spectral resolution of ~ 0.3 eV. The kinetic energy of the generated photoelectrons corresponds to a mean free path of ~ 6 Å and a total information depth of ~ 2 nm, that is, 95% of all detected electrons originated from $3\lambda$[40]. In contrast, the laboratory XPS instrument used a Mg source to generate photons of 1253.688 eV (Mg K$\alpha$1) and 1253.437 eV (Mg K$\alpha$2), and offered an energy resolution of ~ 0.5 eV. The ability to acquire spectra with higher energy resolution and better surface sensitivity using synchrotron radiation ensured that the measured signals are representative of the support's surface and catalytically active palladium atoms[28, 41].

The C1s and O1s spectra were analyzed using the method developed by Blume *et al.* for carbon nanomaterials[41]. This method notably allows to distinguish contributions from $sp^2$ carbon atoms in a graphene-like honeycomb environment, atoms at point-like defects, and atoms in highly disordered environments such as edges and large vacancies (Supplementary Fig. 2). The evolution of the three signals follows a pattern consistent with the graphitization mechanism proposed by Oberlin[30]. As temperature is increased to 800 °C, oxygen-containing

functional groups are thermally decomposed to CO, $CO_2$, and $H_2O$ following a sequential process that has been documented extensively in the carbon field. This process is accompanied by a re-aromatization of the corresponding sites, hence the steady decrease in point-like defects shown in Supplementary Figure 2. The concentration of disordered carbon remains constant during defunctionalization as temperatures in excess of 1000 °C are required to initiate the long-range reorganization and graphitization of graphenic carbons. Graphitization becomes evident from XPS and Raman spectroscopy above 1000 °C and a quasi graphitic state with stacked graphene sheets extending over tens of nanometers is reached after annealing at 3000 °C (Supplementary Table 1, Supplementary Fig. 2 and 8, Fig. 5). The agreement between Raman spectroscopy and synchrotron XPS, which are two techniques with very different information depths, supports that the observed trends hold for the carbon surfaces in direct contact with the Pd nanoparticles.

In agreement with the literature, Pd was observed in its various oxidation states, including contributions corresponding to bulk Pd metal (335.1 eV) and surface oxides (336.9 eV and 337.85 eV). The presence of an additional prominent signal at 335.95 eV was required to fit the spectra and largely contributed to the shoulder visible in Figure 4. This binding energy is inconsistent with the values reported in the literature for $Pd^{1+}$ (~335.5 eV) and $Pd^{2+}$ (336.3-336.9 eV, assigned to PdO)[42]. Therefore, we attributed this contribution to electron-depleted palladium atoms ($Pd^{\delta+}$) resulting from a charge transfer between the metal and the carbon support. Other groups have also reported on the presence of an additional $Pd^{\delta+}$ contribution in the spectra of commercial Pd/C catalysts but they did not comment on the origin of this contribution[38, 43]. Interestingly, in our work, the intensity ratio $Pd^0/Pd^{\delta+}$ was found to decrease with increasing annealing temperature for the Pd/PS-PS800 catalysts series

(Fig. 3 and Supplementary Table 6), suggesting a direct correlation between support properties and electronic structure of the Pd phase. These metal-support interactions are significant as they alter the metal's core (3d) electrons. This effect is comparable to a change in oxidation state. Therefore, a measurable impact on the valence electrons, hence on the catalytic performance, is expected. This hypothesis was confirmed by the consistency in trends for $Pd^{\delta+}$, HCALD selectivity, and annealing temperature for catalysts supported on PS-PS800 scaffolds (Fig. 3).

The treatment at 1000 °C marks the transition from defective graphenic carbons to highly ordered supports, as discussed erlier in this section. Starting at 1000 °C, the surface oxygen concentration further drops from 9 to 3% (Supplementary Table 1) and the structural defects are annealed until nearly all carbon atoms are in a graphitic environment (Supplementary Fig. 2). Interestingly, the trends observed for the Pd/PS-PS800 series diverged for supports annealed at temperatures above 1000 °C. HCALD selectivity reached a plateau for Pd/PS1000 and slightly decreased for the Pd/HHT sample, again following the same trend as the $Pd^{\delta+}$ contribution (Supplementary Tables 2 and 6). Therefore, it appears that an optimal support structure exists and tailoring the defect density and surface functionalization offers a powerful route to fine-tune the performance of Pd/C catalysts. It was previously proposed that defects in graphenic carbons provide anchoring points to disperse and stabilize Pd nanoparticles. While certainly true, our results suggest that additional effects must be considered to synthesize catalysts with optimal performance. Interestingly, deviation from the trends observed for the Pd/PS-PS800 series occurs when the support reaches a graphitic state and gains semi-metallic properties[44]. This observation is consistent with a charge transfer from Pd nanoparticles to the carbon support and for which

the magnitude of charge transfer depends on the defect structure, and thereby electronic properties of the carbon surface.

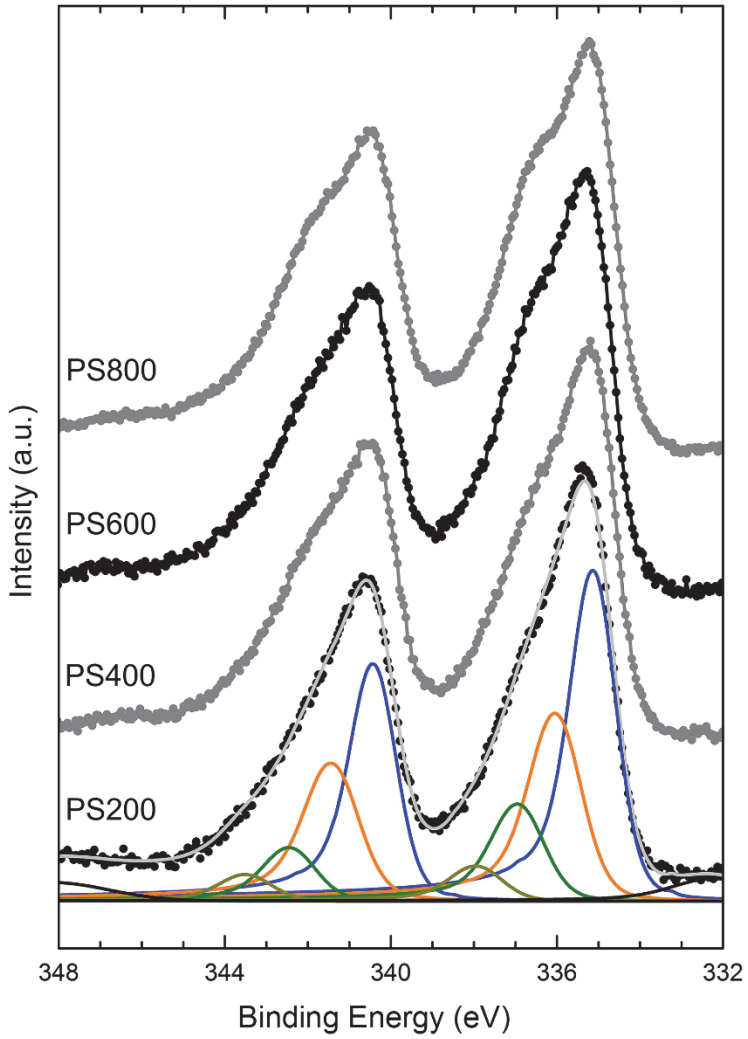


**Figure 4: Lab-source XPS spectra for Pd/PS200 to Pd/PS800 catalysts.** The deconvolved peaks were assigned to Pd metal at 335.1 eV (blue), $Pd^{\delta+}$ at 335.95 eV (orange), and Pd oxides at 336.9 eV and 337.85 eV (green). The increasing contribution of $Pd^{\delta+}$ with treatment temperature largely contributes to the shoulder that appears in the overall spectra between 336 and 337 eV.

### 3.2.5 Support effects on adsorption properties of palladium

Although there is converging indications for charge transfers at the Pd-C interface, the detected $Pd^{\delta+}$ phase may also be due to non-stoichiometric carbides or oxides. The formation of sub-surface carbon is thermodynamically favorable for 5 nm Ni and Pd nanoparticles and can occur at the metal-support interface through abstraction and diffusion of carbon atoms from the defective support[31, 45]. Therefore, we investigated the possible formation of oxides and carbides by XRD, aberration-corrected TEM, and XPS. The results revealed that this hypothesis does not hold in the present study as no carbon was inserted in the Pd lattice of the studied samples. Specifically, the lattice spacings determined by XRD and TEM image analysis were fully consistent with bulk Pd metal ($Pd^0$). No dissolution of carbon in the metal nanoparticles was observed at the interface either (Fig. 5). Larger *d* spacings were measured for the top 2-3 Pd layers but were attributed to the formation of Pd oxides upon sample storage in air, in accordance with the $Pd^{2+}$ contribution in the XPS spectra.

While the electron micrographs did not reveal any distortion of the metal lattice at the Pd-C interface, the images suggest more intimate interactions between the Pd particles and the defective PS carbon support (Fig. 5a) than with the graphitic HHT scaffold (Fig. 5b). Pd atoms at the interface follow the curvature of the wrinkled carbon layers, suggesting that they bind to topological defects and to heteroatoms decorating the amorphous $sp^3$ carbon and/or vacancies. In contrast, a defect-free grain boundary between the graphitic surface of the HHT support and Pd metal is visible in Figure 5b.

Hydrogen isotherms were measured to probe any differences in $H_2$ binding and/or spillover that may arise from changes in the electronic structure of Pd surface atoms. Each

sample was first reduced *in situ* and evacuated at 350 °C to prevent any artefacts due to surface oxides[46]. Two isotherms were successively recorded (double isotherm method) to probe the reversibility of the chemisorption process (Supplementary Fig. 11). The ratios of the reversibly ($H_R$) to irreversibly bound hydrogen ($H_I$) — $H_R/H_I$ — (Supplementary Fig. 12 and Supplementary Table 7) were coherent with the catalytic results (Fig. 3, Supplementary Table 2 and 3), graphitic character, and support functionalization, which was determined by Raman spectroscopy (Supplementary Table 1) and XPS (Supplementary Fig. 2). The higher reversibility for supports with higher surface oxygen concentration has been documented and it was assigned to ligand-like electron donating/withdrawing effect of the support's oxygen-containing functional groups[47, 48]. While this effect was only discussed for small (~2 nm) nanoparticles, our results demonstrate that similar trends hold for larger nanoparticles (~5 nm) that would otherwise be expected to demonstrate bulk-like properties[47, 49]. Our combined observations from hydrogen isotherms and XPS provide experimental evidence that supports electron transfer from the metal to the carbon surface.

Hydrogen spillover was further investigated using high-pressure infrared spectroscopy (HP-FTIR)[47, 50, 51]. All samples, both with and without Pd, showed signals characteristic of $CH_2$ symmetric and asymmetric stretching modes when measured in vacuum (Supplementary Fig. 13). These bands were assigned to the saturation of the graphenic edges with hydrogen during the reduction step at 400 °C. Introducing hydrogen gas in the cell had no effect on the spectra, which suggested that hydrogen spillover is negligible at low pressure. Spillover was observed for the Pd/SCCNT samples only above a threshold pressure of 7 bar, similar to previous investigations performed on Pd/C (Supplementary Fig. 14)[47, 50, 51].

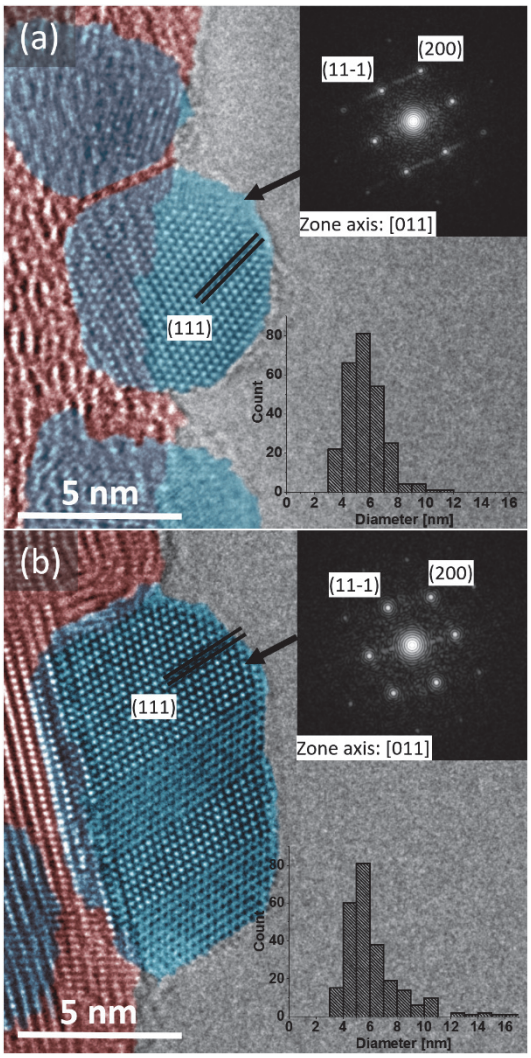


**Figure 5: Aberration corrected TEM.** The micrographs acquired for the (a) Pd/PS and (b) Pd/HHT catalysts provide an atomic-resolution view of the Pd nanoparticles (blue) and of their interface with the carbon support (red). The inserts show the fast Fourier transform results and the particle size distribution. The scale bars in the micrographs (a) and (b) represent 5 nm.

As the differences in reversibility for hydrogen chemisorption cannot be explained by spillover when the pressure is low, we examined the possible contribution of hydrogen absorption and the formation of a Pd β-hydride phase[52]. Palladium hydrides have been

studied extensively and the conditions for their formation have been established. Thermodynamically, the formation of palladium β-hydride depends on the hydrogen partial pressure, temperature, and Pd particle size[53]. Herein, the low hydrogen solubility in dioxane, the selected reaction conditions (80 °C, ambient pressure), and the interactions with the carbon support make any contribution from the β-hydride phase to the observed reactivity trends for Pd/SCCNT unlikely[37, 54, 55, 56]. This conclusion is further supported by our XPS experiments as the $Pd^{\delta+}$ contribution was observed in vacuum.

### 3.2.6 Theoretical evidence for charge transfer

Periodic density functional theory (DFT) calculations were used here to elucidate the differences in metal-support interactions observed with defunctionalization (PS-PS800) and graphitization (PS, LHT, HHT). The interaction energies and binding geometries of sixteen Pd nanoclusters on carbon supports (graphitic or functionalized with oxygen and hydroxide) were examined. The Pd nanoclusters varied in size from 38 (Fig. 6a) to 293 atoms (Fig. 6b) and had 2 to 5 metal layers orthogonal to the basal plane of carbon. Interaction energies for Pd clusters on a pure graphene support were less than 5 kJ $mol^{-1}$ $Pd^{-1}_{interface}$ whereas those on oxidized graphene ranged from 30 to 50 kJ $mol^{-1}$ $Pd^{-1}_{interface}$ (exothermic), indicating a significantly stronger interaction between the metal and the functionalized carbon support. These shifts in interaction energy were also observed in the binding geometries, as Pd clusters merely physisorb above graphene supports (as shown in Fig. 6c for a 293-atom Pd particle) while they chemisorb to the functionalized graphene (Fig. 6d for a 293-atom Pd particle), in agreement with the TEM images of the Pd-C interface (Fig. 5). These results

corroborate the Raman (Supplementary Table 1) and C1s XPS (Supplementary Fig. 2) data and suggest very weak metal-support interactions for Pd/LHT and Pd/HHT.

The binding energies of the probe adsorbates H*, O*, C*, CH*, and OH* at three-fold sites far from the Pd-support interface (shown with pink dots in Fig. 6a,b) were also shifted by changes in the underlying support, although the magnitude of their shift decreased as particles became larger (Fig. 6e). The largest particle (293 atoms) studied here using DFT is a rough hemisphere approximately 2.5 nm in diameter and ~1 nm in height, significantly smaller than the ~5 nm diameter particles catalytically tested. Smaller particles (~100 atoms) showed shifts in binding energies near 50 kJ $mol^{-1}$, indicating major changes in the catalytic behavior of these sites. These results suggest that atoms near the Pd-support interface may be significantly altered and that the magnitude of these alterations may depend on the carbon's surface chemistry, leading to changes in adsorption properties, electronic structure, and selectivity as shown in Figure 3.

QUAMBO charge analysis was performed on three particles of varying size (38, 119, and 293 atoms) bound to a functionalized graphene sheet as shown in Figure 7. Pd atoms bound to the support have median partial charges of +0.15 to +0.17, independently on particle size. This charge transfer is consistent with the appearance of the $Pd^{\delta+}$ contribution in the XPS spectra. Specifically, we estimated the thickness of the $Pd^{\delta+}$ phase based on the $Pd^0/Pd^{\delta+}$ atomic ratio determined from the XPS Pd 3d5/2 peaks (Supplementary Table 6) and assuming hemispherical particles of 5 nm in diameter (Fig. 5, Supplementary Fig. 8, Supplementary Table 5). These calculations show that the $Pd^{\delta+}$ contributions are consistent with a partial charge distributed over the first 1-2 atomic layers near the palladium-carbon interface (Supplementary Table 8), in good agreement with the QUAMBO charge analysis.

Metal atoms in the second layers of all three particles are consistently negatively charged through a compensation effect. This charge is much smaller, in the order of -0.04, and likely falls within the energy resolution of the XPS technique, making it experimentally undetectable. Metal atoms further from the support show little overall charge, indicating that these charge effects are localized and dissipate with distance from the surface, similar to the weaker shifts in binding energies observed with increasing particle size in Fig. 6e.

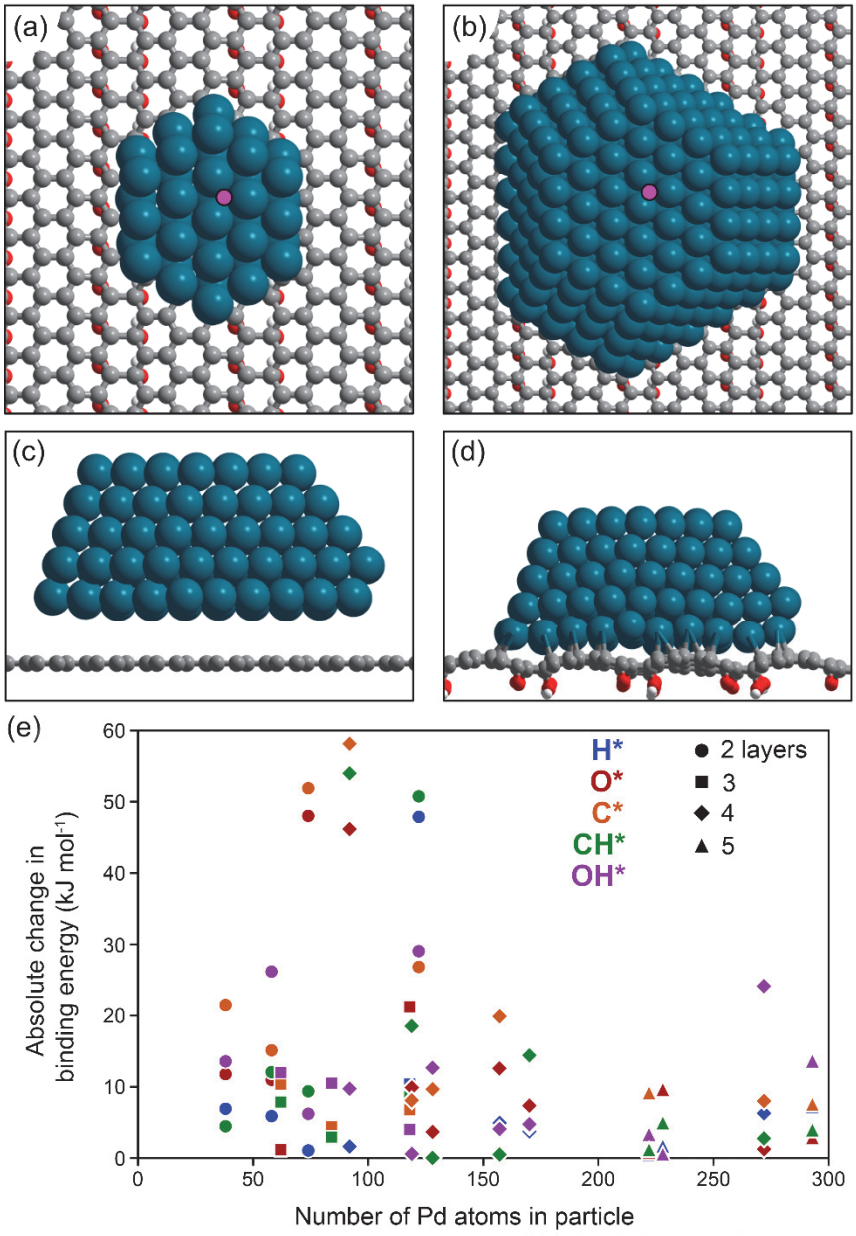


**Figure 6: Theoretical calculations for Pd/C.** (a) $Pd_{38}$ and (b) $Pd_{293}$ clusters bound to a functionalized graphene support; pink dot shows binding location of probe adsorbates. (c) Side-view of $Pd_{293}$ cluster above graphene. (d) Side-view of $Pd_{293}$ cluster bound to functionalized graphene support. (e) Absolute differences in binding energies of H* (blue), O* (red), C* (orange), CH* (green), and OH* (purple) on sites shown in pink in parts (a) and (b) on Pd particles ranging from 38 to 293 atoms and having 2 (●), 3(■), 4(◆), and 5(▲) metal layers.

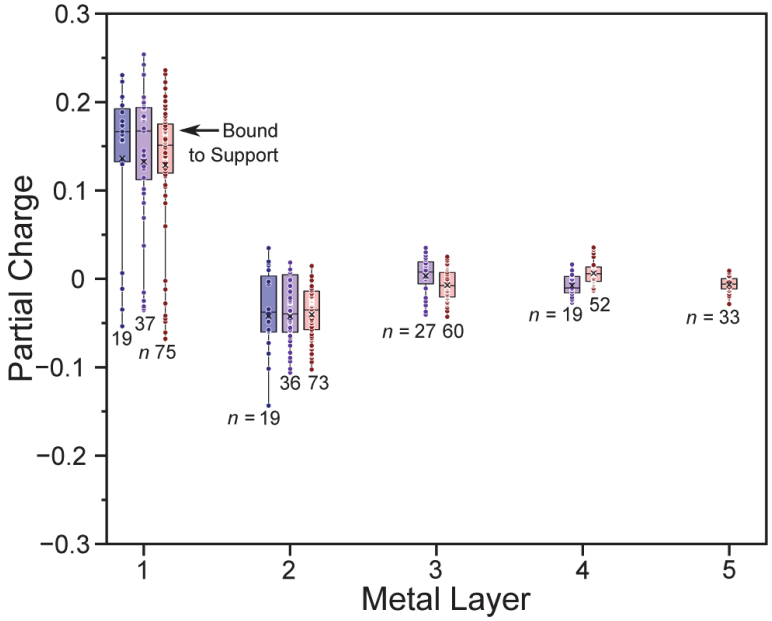


**Figure 7: Partial charge analysis.** Partial charges (QUAMBO) of each Pd atom, organized by metal layer for a 38-atom (blue, 2 layers), 119-atom (purple, 4 layers), and 293-atom (red, 5 layers).

### 3.3 Discussion

Carbon is typically considered an inert catalyst support compared to conventional oxides as it lacks Lewis acid sites and presents only weak Brønsted acid-base properties. Yet, there are numerous examples in the open and patent literatures showing that the activity and selectivity of carbon-supported catalysts are sensitive to the choice of the carbon scaffold[19, 20, 21, 31]. These support effects remain poorly understood and, in the case of cinnamaldehyde hydrogenation, they were attributed to differences in the reactant's adsorption mode depending on surface polarity[20, 21, 36]. However, this interpretation underestimates the structural and chemical complexity of carbon supports and, in particular, the electronic effects that may take place at the metal-carbon interface. Recent works on single-atom catalysis suggest that heteroatoms decorating defect sites play a role similar to ligands in homogeneous catalysis, where the activity of metal centers can be modulated through

electron donation and withdrawal[57]. Obviously, ligand effects as defined in the ligand field theory are spatially constrained as they require orbitals of the metal atom and its ligands to overlap. The impact of these electronic effects on metal nanoparticles of 5 nm size, which consist of hundreds of atoms, is negligible: assuming hemispherical nanoparticles with 11 % of the Pd atoms at the interface and an oxygen-to-carbon ratio of 0.25, at most ~2.75 % of the total Pd atoms would be altered through ligand effects. This small percentage of Pd atoms located at the interface and influenced by ligand effects is inconsistent with the $Pd^0/Pd^{\delta+}$ ratios determined by XPS and the trends we observed (Fig. 3). Yet, the correlations we established between support properties and hydrogenation performance demonstrate that carbon scaffolds play a non-innocent role on the catalytic activity of large nanoparticles. The detailed characterization of our catalysts allowed us to rule out common artefacts related to variations in metal loading, particle size, particle shape, and mass transfer limitations. The reaction conditions we selected also allowed us to exclude contributions from hydrogen spillover and palladium β-hydride. Finally, correlations between catalytic activity, chemisorption, XPS, TEM, Raman spectroscopy, and the differences in their respective measurement conditions (different temperatures, pressures, and gas/vacuum environments) are consistent with a charge transfer from the metal to the carbon scaffold for Pd supported on the PS-PS800 SCCNT series. Our theoretical calculations also corroborate this interpretation. The QUAMBO charge analysis indicates strong EMSI that alter 20 % of the Pd atoms, in agreement with the $Pd^0/Pd^{\delta+}$ atomic ratio determined by XPS. While the partial charge seems to be only distributed on the metal atoms near the interface with the support, these effects dissipate over several layers, as indicated by the calculations performed with probe adsorbates (Fig. 6).

The correlations between $Pd^{\delta+}$ intensity and support surface functionalization can be explained by the changes in electronic properties of the support. The decrease in the work function (Φ) of carbon scaffolds with decreasing oxygen functionalities has been shown[58, 59]. Theoretical calculations have revealed that common oxygen functionalities (epoxy, carbonyl, hydroxyl) cause an increase of up to 60 % of graphene's computed work function due to the formation of C-O dipoles[59]. The shift in Φ was found to depend on oxygen concentration and the nature of the O-containing functional groups, hence the intensity of the corresponding dipole moment. For the present study, the decrease in oxygen concentration with annealing temperature (Supplementary Table 1) would progressively lower Φ of the graphenic layer in the studied SCCNTs, thus increase the difference between the Φ of Pd (5.2-5.6 eV) and the support. This difference has been reported to influence charge transfer in the case of metal oxide supports with EMSI effects[10, 11]. The interpretation is further supported by previous studies on cinnamaldehyde hydrogenation, which demonstrated that the selectivity towards C=C or C=O bond hydrogenation scales with the position of the d band center of the metal active phase. Metals with a d band center far from the Fermi level (*e.g.* Pt) are selective towards CALC while Pd is more selective towards HCALD. This selectivity can be further modulated through ligands and promoters. For example, it was shown that the addition of Co, an electropositive element, provides electron density to Pt, hence lowers its d band center (more negative) and further enhances the selectivity to CALC due to the preferential formation of di-σ metal C-O bond[35]. Here, the increase in HCALD selectivity with $Pd^{\delta+}$, thus the electron depletion of the metal active phase and the up-shift of its d band center, is fully consistent with this interpretation.

The above analysis does not only correlate changes in selectivity with the electronic properties of the studied supports, but the results for the PS-PS800 series also pave the way for a quantitative control of these effects in order to achieve a desired selectivity. Specifically, this study shows that the catalytic activity of a desired metal can be controlled by selectively functionalizing or defunctionalizing (*e.g.* by annealing) the surface of the carbon support.

In summary, the influence of support surface functionalization and graphitization on electronic and adsorption properties of the active metal phase was elucidated in this work. The correlations between support functionalization, charge distribution at the metal-carbon interface, and catalytic selectivity were established. These correlations provide insights into how carbon support can be utilized for tuning the electronic properties of the metal decorating its surface through Schwab effects, hence its catalytic performance. The present work is expected to set the foundations of general rules that will enable the rational design of carbon-supported catalysts.

## 3.4 Methods

### 3.4.1 Catalyst synthesis

Stacked cup carbon nanotubes (SCCNTs) were obtained from Pyrograf Products, Inc (Ohio, USA). The SCCNTs were synthesized by chemical vapor deposition (CVD) and annealed at 700, 1500, 3000 °C post-synthesis to obtain, respectively, the pyrolytically stripped (PS), low heat treated (LHT), and high heat treated (HHT) supports. Detailed characterization of the SCCNTs can be found elsewhere[28]. 10 g of SCCNTs were functionalized using 500 ml of trace metal grade concentrated nitric acid at 100 °C for 4 h,

followed by washing with 5 L of deionized water and drying overnight at 110 °C. The PS SCCNTs were divided into separate batches and thermally defunctionalized in flowing nitrogen at 200, 400, 600, 800, 1000 °C for 30 min to obtain the PS200-PS1000 series of supports. The increased treatment temperature for the PS200-PS1000 series removes oxygen functionalities of the supports.

Pd was deposited on the supports in the form of nanoparticles using incipient wetness impregnation. Typically, 125 mg of palladium (II) nitrate dihydrate was dissolved in 8.4 ml of deionized water (at pH 4.0, adjusted using nitric acid) and the solution was added dropwise to 1 g of the supports, followed by sonication for 5 min. The samples were dried overnight at 65 °C followed by drying at 80 °C for 8 h in an oven. The impregnated and dried SCCNTs were then placed in a tube furnace and calcined in air (200 ml $min^{-1}$) while heating at 2 °C $min^{-1}$ to 250 °C and held at this temperature for 2 h. The calcined catalysts were cooled down to room temperature and were flushed with nitrogen gas for 30 min and subsequently reduced under hydrogen (200 ml $min^{-1}$) at 400 °C for 2 h. The gas flow rates were controlled using Brooks mass flow controllers.

### 3.4.2 Raman spectroscopy

The nitric acid-treated SCCNTs supports were characterized using Raman spectroscopy to estimate the ratio of graphitic to defective carbon of the supports. A Renishaw inVia Raman Microscope equipped with a coherent Argon ion laser was used for the analysis. Each sample was analyzed at 3 different spots to ensure homogeneity of the sample. 10 accumulations with a 30 s acquisition time, 25 mW power of a laser line at 488 nm were used for each analysis. The measurement range from 800 $cm^{-1}$ to 2000 $cm^{-1}$ was

used for analysis. The data analysis was conducted using the method described by Knauer et. al.[60] According to this method, a multi-component baseline fit and deconvolution was used: bands at 1580 $cm^{-1}$ (G-band), 1350 $cm^{-1}$ ($D_1$-band), 1620 $cm^{-1}$ ($D_2$-band), and 1200 $cm^{-1}$ ($D_4$-band) were fit with Lorentzian peaks while the contribution at 1500 $cm^{-1}$ ($D_3$-band) was fit with a Gaussian peak (Supplementary Fig. 1). The Lorentzian peak at 1350 $cm^{-1}$ ($D_1$) is characteristic of the defective carbon atoms within a graphene layer and the peak at 1580 $cm^{-1}$ (G) represents the in-plane stretching of the $sp^2$ hybridized carbon in the honeycomb carbon structure. The ratio of the graphitic to the defective carbon bands was estimated using the G and D1 peaks (Supplementary Table 1). The peaks D2 and D4 were attributed to the non-graphitic basic structural units (BSUs) while the D3 peak was attributed to the non-graphitic or molecular carbon content of the samples by Knauer et. al. in their work[60]. Since these peaks are not representative of the graphitic core but were a part of the amorphous carbon layer present on the surface, they were not considered for calculating the graphitic character of the supports in the present work.

### 3.4.3 Inductively coupled plasma optical emission spectroscopy

The bulk homogeneity of the metal loading on the carbon supports was confirmed by analyzing the samples using Inductively coupled plasma-optical emission spectroscopy (ICP-OES) with a Perkin Elmer Optima 8000 instrument. Prior to the analysis, 30 mg of each catalyst was placed in different crucibles and treated in a muffle furnace at 1000 °C for 6 h to burn off the carbon supports. The residual contents of the crucibles were soaked overnight in 5 ml aqua regia (1:3 volume ratio of nitric acid:hydrochloric acid) for dissolving the Pd. The aqua regia with the dissolved Pd was then carefully transferred to a 50 ml volumetric flask

and the total volume was made up to 50 ml using DI water. The standards for the calibration curve were prepared using a 10 vol% aqua regia in water solution and the Pd ICP standard (1000 ppm). Each catalyst was analyzed in quadruplicates.

### 3.4.4 Scanning electron microscopy

The catalysts were characterized at the micro- and nano- scale by studying the catalyst morphology using a FEI Quanta 250 instrument operated at 10 kV. The catalyst samples were placed in aluminum pans mounted on carbon stubs. A solution of sticking tape soaked in hexane was added on the catalyst samples and the sample was levelled off to decrease the surface roughness. The samples were imaged at different magnifications and in different regions using both the secondary electron (SE) and back-scattered electron (BSE) detectors.

### 3.4.5 Transmission electron microscopy

Transmission electron microscopy (TEM) analysis was conducted using a JEOL 2100 FEG S/TEM microscope operated at 200 kV equipped with a spherical aberration corrector on the probe forming lens. The samples were dispersed in ethanol and deposited on a holey carbon coated TEM grid. For scanning transmission electron micrsocopy (STEM) high-angular annular dark field (HAADF) analysis, a spot size of 0.13 nm, a current density of 140 pA, a camera focal length of 8 cm, corresponding to inner and outer diameters of the annular detector of about 73 mrad and 194 mrad, were used.

Aberration corrected TEM was conducted using an FEI Titan 80-300 operated at 300 kV equipped with a Gatan US1000 CCD camera. The samples were dispersed in ethanol and deposited on a holey carbon coated TEM grid.

### 3.4.6 X-ray diffraction

X-ray diffraction (XRD) analysis was conducted using a Siemens D-500 instrument equipped with a copper X-ray tube, a diffracted beam monochromator, and a scintillation detector. The measurements were conducted using a gold holder and a medium resolution slit. The samples were scanned from 10 to 70 degrees two-theta with a step size of 0.05 degrees and a dwell time of 3 s per step. Jade software was used to analyze the data and the Scherrer equation was used to estimate the crystallite size.

### 3.4.7 Hydrogen chemisorption

Hydrogen chemisorption adsorption isotherm studies were conducted using a Micromeritics ASAP 2020C instrument. 50 mg of the sample was loaded in a chemisorption tube and packed using quartz wool. The sample was reduced in-situ at 350 °C followed by long evacuation steps to remove the adsorbed hydrogen. Hydrogen was then re-introduced in the system at increasing pressures (2-450 mm Hg) under isothermal conditions (35 °C) for studying the first adsorption isotherm and the amount of total adsorbed hydrogen ($H_T$) was calculated. A long evacuation step was then applied to remove the weakly or reversibly bound hydrogen and then a second adsorption isotherm was recorded to estimate the reversibly adsorbed hydrogen ($H_R$). The size of the Pd nanoparticles was obtained using $H_T$ and the ratio of the $H_R/H_I$ was calculated to compare the catalysts.

### 3.4.8 X-Ray photoelectron spectroscopy

Lab source X-ray photoelectron spectroscopy (XPS) studies were conducted using a Kratos Amicus ESCA 3400 instrument. The anode used for the analysis was Mg (240 W) with the photon energy of K alpha 1 peak at 1253.688 eV and K alpha 2 peak at 1253.437 eV. The samples were loaded on an indium foil used here as an internal standard. A dwell time of 1 s, step size of 50 meV, and a pass energy of 150 eV were used. 5 sweeps were recorded for each sample. Sputtered In foil and HOPG samples were used as standards for data analysis for Pd and C. Data analysis was conducted using the Fitt-win software.

Synchrotron radiation studies were conducted during single bunch mode at the ISISS beamline of the Fritz Haber Institute located at the BESSY II synchrotron facility in Berlin. The high pressure setup consists mainly of a reaction cell attached to a set of differentially pumped electrostatic lenses and a differential-pumped analyzer (Phoibos 150 Plus, SPECS GmbH), as described elsewhere[61]. The spectra were collected in normal emission in vacuum with a probe size of ≈ 150μm x 80μm. Sample contamination was checked by survey spectra at the beginning of each experiment. For XPS analysis, the photoelectron binding energy (BE) is referenced to the Fermi edge, and the spectra are normalized to the incident photon flux. The photoionization cross section was considered according to the calculations of Yeh and Lindau[62]. Background correction was performed by using a Shirley background[63]. The spectra were fitted following the Levenberg-Marquardt algorithm to minimize the $\chi^2$. Peak shapes were modeled by using asymmetric Doniach-Sunjic functions convoluted with Gaussian profiles[64]. The accuracy of the fitted peak positions is ≈ 0.05 eV.

### 3.4.9 High pressure Fourier transform infrared spectroscopy

In-situ Fourier transform infrared (FTIR) studies were conducted to determine the interaction between hydrogen and the Pd/C catalysts using a Nicolet 6700 Thermo Scientific spectrometer. Approximately 0.7 mg of the catalyst powder was pressed onto a KBr pellet of 1 cm diameter and 2 mm thickness. The sample was then placed in a high-pressure high-temperature cell (P/N 5850c, Specac Ltd, UK) at the focal point of the spectrometer sample compartment. The samples (Pd catalysts supported on PS, LHT, HHT, PS200, PS600, and PS1000) were activated under 1 atm of hydrogen at 100 °C for at least for 1 h then cooled down to room temperature for the IR measurements. The IR spectra were recorded after each heating cycle. The resulting spectra were analyzed to monitor changes in adsorbate concentrations. The pressures used for the analyses were 15, 100, and 200 psi (1, 7, and 14 bar).

### 3.4.10 Catalytic tests

The catalytic performance was probed for the liquid phase hydrogenation of cinnamaldehyde. 100 mg of Pd/C catalyst, 40 ml dioxane, and 365 mg decane (internal standard) were added to a 100 ml 3-neck flask with a stir-bar. The flask was connected to a condenser with water at 4 °C. The reaction mixture was magnetically stirred at 500 rpm and heated using an oil bath kept at 80 °C using an IKA-RCT magnetic stir plate equipped with a PT1000 thermocouple. Nitrogen and hydrogen were provided to the solution using a gas dispersion tube equipped with a fine frit (10-20 μm porosity). The gas flow rate was controlled using a Bronkhorst mass flow controller. A rubber septum was connected to the third neck of the flask and an 18 gauge, 6 inch needle was inserted in it for sampling. The top

end of the needle was wrapped with parafilm to avoid any losses due to evaporation of dioxane. In a typical experiment, nitrogen was sparged through the flask at 20 ml $min^{-1}$ for 20 min at room temperature to remove any air from the system. The gas flow was then switched to hydrogen at 20 ml $min^{-1}$ and the temperature of the oil bath was raised to 80 °C and maintained at this temperature for 30 min. 5 g of trans-cinnamaldehyde dissolved in 10 ml dioxane was then added to the flask and this time was marked as the beginning of the reaction. Samples were withdrawn at specific time intervals using a glass syringe in pre-cooled glass vials and placed in the refrigerator immediately to quench the reaction.

The reaction samples were diluted 15 times with dioxane, filtered using 0.22 μm nylon filters, and analyzed using an Agilent 7890A gas chromatograph (GC-FID) with an HP-5 column (30m x 320 μm x 0.25μm). An injection volume of 1 μl with a split ratio of 20:1 at 20ml $min^{-1}$ was used. The inlet heater temperature was maintained at 300 °C with a total flow of 24 ml $min^{-1}$ and a septum purge flow of 3 ml $min^{-1}$. A column flow of 1 ml $min^{-1}$ was used. The oven initial temperature of 40 °C was held for 1 min followed by ramping to 180 °C at 10 °C $min^{-1}$. The detector heater temperature was maintained at 300 °C.

The product selectivities were calculated using Equation 1:

$$Selectivity\ (\%) = \frac{(Moles\ of\ product\ produced\ at\ t)}{(Moles\ of\ reactant\ converted\ at\ t)}\ X\ 100 \qquad (1)$$

where, the moles of the product produced and the moles of reactant converted were calculated for same time t for the reaction.

### 3.4.11 Density functional theory calculations

Plane-wave density functional theory calculations were performed using the Vienna ab initio simulation package (VASP)[65] to calculate interaction energies between Pd particles

and C-supports (with and without functionalization) and binding energies of probe adsorbates (H*, O*, C*, OH*, and CH*). Plane-waves were constructed using an energy cutoff of 400 eV with projector augmented wave potentials[66]. The revised Perdew–Burke–Ernzerhof (RPBE) form of the generalized gradient approximation (GGA) was used to determine exchange and correlation energies[67, 68]. Wavefunctions were converged to within $10^{-6}$ eV and forces were computed using a fast Fourier transform (FFT) grid with a cutoff of twice the planewave cutoff. A 1 × 1 × 1 Γ-point sampling of the first Brillouin zone (k-point mesh) was used and structures were relaxed until forces on unconstrained atoms were <0.05 eV $Å^{-1}$. Converged wavefunctions were transformed into a set of localized quasiatomic orbitals (QUAMBOs)[69] and used to carry out Löwdin population analyses[70] to determine the charges on the individual atoms.

Pd particles were modeled as cubo-octahedral particles which are composed of (100) and (111) surfaces. The dimensions of these surfaces were varied to generate sixteen particles ranging from 38 to 293 Pd atoms arranged in 2-5 metal layer orthogonal to the C-support supported on a single graphene sheet.

The C-support was modeled as either a single-layer graphene sheet, a two-layer graphene sheet, or a functionalized graphene sheet (which has 0.125 ML of O* and 0.125 ML of OH* adsorbed). The lattice parameters for the functionalized graphene sheet were 8.702 and 2.512; those for an equivalent pure graphene sheet were 8.523 and 2.46, indicating that functionalization of the graphene sheet is associated with an expansion in C–C bonds. The functionalized graphene sheet, furthermore, is curved in a periodic manner, further increasing C–C bond lengths in a manner consistent with the rehybridization of C-atoms from $sp^2$ to $sp^3$.

Probe adsorbates H*, O*, C*, OH*, and CH* were modeled on the Pd particles at sites far from the Pd-C interface (at the center-most three-fold site on the (111) surface opposite the Pd-support interface). Binding energies for these adsorbates were compared when the support was pure graphene and when the support was functionalized graphene using Equation 2:

$$\Delta BE = |E[\text{adsorbate on Pd on functionalized graphene}] - E[\text{Pd on functionalized graphene}] - (E[\text{adsorbate on Pd on graphene}] - E[\text{Pd on graphene}])| \quad (2)$$

where, ΔBE represents the absolute value of the shift in binding energy of the probe adsorbate.

### 3.5 References


1. Matsubu, J. C. et al. Adsorbate-mediated strong metal–support interactions in oxide-supported Rh catalysts. *Nat. Chem.* **9,** 120-127 (2016).

2. Willinger, M. G., Zhang, W., Bondarchuk, O., Shaikhutdinov, S., Freund, H. J. & Schlögl, R. A case of strong metal–support interactions: Combining advanced microscopy and model systems to elucidate the atomic structure of interfaces. *Angew. Chem. Int. Ed.* **53,** 5998-6001 (2014).

3. Norskov, J. K., Bligaard, T., Rossmeisl, J. & Christensen, C. H. Towards the computational design of solid catalysts. *Nat. Chem.* **1,** 37-46 (2009).

4. Calle-Vallejo, F. et al. Finding optimal surface sites on heterogeneous catalysts by counting nearest neighbors. *Science* **350,** 185-189 (2015).

5. Lee, I., Delbecq, F., Morales, R., Albiter, M. A. & Zaera, F. Tuning selectivity in catalysis by controlling particle shape. *Nat. Mater.* **8,** 132-138 (2009).

6. Copéret, C., Chabanas, M., Petroff Saint-Arroman, R. & Basset, J.-M. Homogeneous and heterogeneous catalysis: Bridging the gap through surface organometallic chemistry. *Angew. Chem. Int. Ed.* **42,** 156-181 (2003).

7. Schwab, G. M. Boundary-layer catalysis. *Angew. Chem. Int. Ed.* **6,** 375-375 (1967).

8. Gunasooriya, G. T. K. K., Seebauer, E. G. & Saeys, M. Ethylene hydrogenation over $Pt/TiO_2$: A charge-sensitive reaction. *ACS Catal.* **7,** 1966-1970 (2017).

9. Tauster, S. J. Strong metal-support interactions. *Acc. Chem. Res.* **20,** 389-394 (1987).

10. Fu, Q. & Wagner, T. Interaction of nanostructured metal overlayers with oxide surfaces. *Surf. Sci. Rep.* **62,** 431-498 (2007).

11. Ahmadi, M., Mistry, H. & Roldan Cuenya, B. Tailoring the catalytic properties of metal nanoparticles via support interactions. *J. Phys. Chem. Lett.* **7,** 3519-3533 (2016).

12. Haller, G. L. & Resasco, D. E. Metal–support interaction: Group VIII metals and reducible oxides. In: Eley DD, Pines H, Weisz PB (eds). *Advances in catalysis*, vol. 36. Academic Press, 1989, pp 173-235.

13. Behrens, M. et al. The active site of methanol synthesis over $Cu/ZnO/Al_2O_3$ industrial catalysts. *Science* **336,** 893-897 (2012).

14. Auer, E., Freund, A., Pietsch, J. & Tacke, T. Carbons as supports for industrial precious metal catalysts. *Appl. Catal., A* **173,** 259-271 (1998).

15. Su, D. S., Perathoner, S. & Centi, G. Nanocarbons for the development of advanced catalysts. *Chem. Rev.* **113,** 5782-5816 (2013).

16. Zhu, J., Holmen, A. & Chen, D. Carbon nanomaterials in catalysis: Proton affinity, chemical and electronic properties, and their catalytic consequences. *ChemCatChem* **5,** 378-401 (2013).

17. Perathoner, S., Ampelli, C., Chen, S., Passalacqua, R., Su, D. & Centi, G. Photoactive materials based on semiconducting nanocarbons – a challenge opening new possibilities for photocatalysis. *J. Energy Chem.* **26,** 207-218 (2017).

18. Xia, W. Interactions between metal species and nitrogen-functionalized carbon nanotubes. *Catal. Sci. Tech.* **6,** 630-644 (2016).

19. Arrigo, R. et al. New insights from microcalorimetry on the $FeO_x$/CNT-based electrocatalysts active in the conversion of $CO_2$ to fuels. *ChemSusChem* **5,** 577-586 (2012).

20. Toebes, M. L., Prinsloo, F. F., Bitter, J. H., van Dillen, A. J. & de Jong, K. P. Influence of oxygen-containing surface groups on the activity and selectivity of carbon nanofiber-supported ruthenium catalysts in the hydrogenation of cinnamaldehyde. *J. Catal.* **214,** 78-87 (2003).

21. Toebes, M. L. et al. Support effects in the hydrogenation of cinnamaldehyde over carbon nanofiber-supported platinum catalysts: Characterization and catalysis. *J. Catal.* **226,** 215-225 (2004).

22. Tessonnier, J.-P., Pesant, L., Ehret, G., Ledoux, M. J. & Pham-Huu, C. Pd nanoparticles introduced inside multi-walled carbon nanotubes for selective

hydrogenation of cinnamaldehyde into hydrocinnamaldehyde. *Appl. Catal., A* **288,** 203-210 (2005).

23. Plomp, A. J., Vuori, H., Krause, A. O. I., de Jong, K. P. & Bitter, J. H. Particle size effects for carbon nanofiber supported platinum and ruthenium catalysts for the selective hydrogenation of cinnamaldehyde. *Appl. Catal., A* **351,** 9-15 (2008).

24. Zheng, Y. et al. Hydrogen evolution by a metal-free electrocatalyst. *Nat. Commun.* **5,** 3783 (2014).

25. Ito, Y., Cong, W., Fujita, T., Tang, Z. & Chen, M. High catalytic activity of nitrogen and sulfur co-doped nanoporous graphene in the hydrogen evolution reaction. *Angew. Chem. Int. Ed.* **54,** 2131-2136 (2015).

26. Su, D. S. et al. Metal-free heterogeneous catalysis for sustainable chemistry. *ChemSusChem* **3,** 169-180 (2010).

27. Loh, K. P., Bao, Q., Eda, G. & Chhowalla, M. Graphene oxide as a chemically tunable platform for optical applications. *Nat. Chem.* **2,** 1015-1024 (2010).

28. Tessonnier, J.-P. et al. Analysis of the structure and chemical properties of some commercial carbon nanostructures. *Carbon* **47,** 1779-1798 (2009).

29. Tessonnier, J.-P. et al. Influence of the graphitisation of hollow carbon nanofibers on their functionalisation and subsequent filling with metal nanoparticles. *Chem. Commun.* 7158-7160 (2009).

30. Oberlin, A. Carbonization and graphitization. *Carbon* **22,** 521-541 (1984).

31. Rinaldi, A. et al. Dissolved carbon controls the initial stages of nanocarbon growth. *Angew. Chem. Int. Ed.* **50,** 3313-3317 (2011).

32. Liu, P., Qin, R., Fu, G. & Zheng, N. Surface coordination chemistry of metal nanomaterials. *J. Am. Chem. Soc.* **139,** 2122-2131 (2017).

33. Kwon, S. G. et al. Capping ligands as selectivity switchers in hydrogenation reactions. *Nano Lett.* **12,** 5382-5388 (2012).

34. Kahsar, K. R., Schwartz, D. K. & Medlin, J. W. Control of metal catalyst selectivity through specific noncovalent molecular interactions. *J. Am. Chem. Soc.* **136,** 520-526 (2014).

35. Jiang, F., Cai, J., Liu, B., Xu, Y. & Liu, X. Particle size effects in the selective hydrogenation of cinnamaldehyde over supported palladium catalysts. *RSC Adv.* **6,** 75541-75551 (2016).

36. Durndell, L. J., Parlett, C. M. A., Hondow, N. S., Isaacs, M. A., Wilson, K. & Lee, A. F. Selectivity control in Pt-catalyzed cinnamaldehyde hydrogenation. *Sci. Rep.* **5,** 9425 (2015).

37. Ide, M. S., Hao, B., Neurock, M. & Davis, R. J. Mechanistic insights on the hydrogenation of α, β-unsaturated ketones and aldehydes to unsaturated alcohols over metal catalysts. *ACS Catal.* **2,** 671-683 (2012).

38. Cárdenas-Lizana, F. et al. Selective gas phase hydrogenation of p-chloronitrobenzene over Pd catalysts: Role of the support. *ACS Catal.* **3,** 1386-1396 (2013).

39. Davis, R. J. Reaction engineering concepts for the catalytic conversion of biorenewable molecules. In: Behrens M, Datye AK (eds). *Catalysis for the conversion of biomass and its derivatives*: Berlin, Germany, 2013.

40. Seah, M. Data compilations: Their use to improve measurement certainty in surface analysis by AES and XPS. *Surf. Interface Anal.* **9,** 85-98 (1986).

41. Blume, R., Rosenthal, D., Tessonnier, J.-P., Li, H., Knop-Gericke, A. & Schlögl, R. Characterizing graphitic carbon with X-ray photoelectron spectroscopy: A step-by-step approach. *ChemCatChem* **7,** 2871-2881 (2015).

42. Zhao, Z. et al. Synthesis of stable shape-controlled catalytically active β-palladium hydride. *J. Am. Chem. Soc.* **137,** 15672-15675 (2015).

43. Arrigo, R. et al. Pd supported on carbon nitride boosts the direct hydrogen peroxide synthesis. *ACS Catal.* **6,** 6959-6966 (2016).

44. Dresselhaus, M. S., Dresselhaus, G. & Saito, R. Electronic band structure of graphites. In: Delhaès P (ed). *Graphite and precursors*, vol. 1. Gordon and Breach Science Publishers, Amsterdam, 2000, pp 25-44.

45. Teschner, D. et al. Alkyne hydrogenation over Pd catalysts: A new paradigm. *J. Catal.* **242,** 26-37 (2006).

46. Ghimbeu, C. M. et al. Understanding the mechanism of hydrogen uptake at low pressure in carbon/palladium nanostructured composites. *J. Mater. Chem.* **21,** 17765-17775 (2011).

47. Liu, X. M. et al. Evidence for ambient-temperature reversible catalytic hydrogenation in pt-doped carbons. *Nano Lett.* **13,** 137-141 (2013).

48. Coloma, F., Sepulveda-Escribano, A., Fierro, J. L. G. & Rodriguez-Reinoso, F. Preparation of platinum supported on pregraphitized carbon blacks. *Langmuir* **10,** 750-755 (1994).

49. Stuckert, N. R., Wang, L. & Yang, R. T. Characteristics of hydrogen storage by spillover on Pt-doped carbon and catalyst-bridged metal organic framework. *Langmuir* **26,** 11963-11971 (2010).

50. Dibandjo, P. et al. Hydrogen storage in hybrid nanostructured carbon/palladium materials: Influence of particle size and surface chemistry. *Int. J. Hydrogen Energy* **38,** 952-965 (2013).

51. Blackburn, J. L. et al. Spectroscopic identification of hydrogen spillover species in ruthenium-modified high surface area carbons by diffuse reflectance infrared fourier transform spectroscopy. *J. Phys. Chem. C* **116,** 26744-26755 (2012).

52. García-Mota, M., Bridier, B., Pérez-Ramírez, J. & López, N. Interplay between carbon monoxide, hydrides, and carbides in selective alkyne hydrogenation on palladium. *J. Catal.* **273,** 92-102 (2010).

53. Johansson, M., Skulason, E., Nielsen, G., Murphy, S., Nielsen, R. M. & Chorkendorff, I. Hydrogen adsorption on palladium and palladium hydride at 1bar. *Surf. Sci.* **604,** 718-729 (2010).

54. Amorim, C. & Keane, M. A. Palladium supported on structured and nonstructured carbon: A consideration of pd particle size and the nature of reactive hydrogen. *J. Colloid Interface Sci.* **322,** 196-208 (2008).

55. Brunner, E. Solubility of hydrogen in 10 organic solvents at 298.15, 323.15, and 373.15 K. *J. Chem. Eng. Data* **30,** 269-273 (1985).

56. Bhat, V. V., Contescu, C. I. & Gallego, N. C. The role of destabilization of palladium hydride in the hydrogen uptake of Pd-containing activated carbons. *Nanotechnology* **20,** 204011 (2009).

57. Cheng, N. et al. Platinum single-atom and cluster catalysis of the hydrogen evolution reaction. *Nat. Commun.* **7,** 13638 (2016).

58. Lin, Y.-J. & Zeng, J.-J. Tuning the work function of graphene by ultraviolet irradiation. *Appl. Phys. Lett.* **102,** 183120 (2013).

59. Kumar, P. V., Bernardi, M. & Grossman, J. C. The impact of functionalization on the stability, work function, and photoluminescence of reduced graphene oxide. *ACS Nano* **7,** 1638-1645 (2013).

60. Knauer, M., Schuster, M. E., Su, D., Schlögl, R., Niessner, R. & Ivleva, N. P. Soot structure and reactivity analysis by raman microspectroscopy, temperature-programmed oxidation, and high-resolution transmission electron microscopy. *J. Phys. Chem. A* **113,** 13871-13880 (2009).

61. Bluhm, H., Hävecker, M., Knop-Gericke, A., Kiskinova, M., Schloegl, R. & Salmeron, M. In situ X-ray photoelectron spectroscopy studies of gas-solid interfaces at near-ambient conditions. *MRS Bull.* **32,** 1022-1030 (2007).

62. Yeh, J. & Lindau, I. Atomic subshell photoionization cross sections and asymmetry parameters: $1 \leqslant z \leqslant 103$. *At. Data Nucl. Data Tables* **32,** 1-155 (1985).

63. Shirley, D. A. High-resolution X-ray photoemission spectrum of the valence bands of gold. *Phys. Rev. B* **5,** 4709 (1972).

64. Doniach, S. & Sunjic, M. Many-electron singularity in X-ray photoemission and X-ray line spectra from metals. *J. Phys. Condens. Matter* **3,** 285 (1970).

65. Kresse, G. & Hafner, J. Ab initio molecular dynamics for liquid metals. *Phys. Rev. B* **47,** 558 (1993).

66. Blöchl, P. E. Projector augmented-wave method. *Phys. Rev. B* **50,** 17953 (1994).

67. Perdew, J. P., Burke, K. & Ernzerhof, M. Generalized gradient approximation made simple. *Phys. Rev. Lett.* **77,** 3865 (1996).

68. Hammer, B., Hansen, L. B. & Nørskov, J. K. Improved adsorption energetics within density-functional theory using revised perdew-burke-ernzerhof functionals. *Phys. Rev. B* **59,** 7413 (1999).

69. Lu, W., Wang, C., Schmidt, M., Bytautas, L., Ho, K. & Ruedenberg, K. Molecule intrinsic minimal basis sets. I. Exact resolution of ab initio optimized molecular orbitals in terms of deformed atomic minimal-basis orbitals. *J. Chem. Phys.* **120,** 2629-2637 (2004).

70. Löwdin, P. O. On the non-orthogonality problem connected with the use of atomic wave functions in the theory of molecules and crystals. *J. Chem. Phys.* **18,** 365-375 (1950).

### 3.6 Acknowledgements

We acknowledge the financial support from the National Science Foundation Grant Number EEC-0813570. We thank Dr. Dapeng Jing and Dr. Scott Schlorholtz of the Materials Analysis and Research Laboratory at Iowa State University for their help with the X-ray photoelectron spectroscopy and X-ray diffraction studies, respectively.

### 3.7 Author contributions

R.G.R and J.P.T designed the study. R.G.R synthesized the catalysts, performed the catalytic tests, and characterized the samples unless stated otherwise. R.B. conducted the XPS studies using synchrotron radiation and analyzed the XPS data acquired with both lab and synchrotron sources. S.M. and O.E. characterized the samples using TEM. T.W.H. acquired and analyzed the high magnification aberration-corrected TEM images of the samples. E.F. and Y.J.C. conducted the high-pressure Fourier transform infrared spectroscopy studies. K.D. and D.D.H. performed the theoretical calculations. All authors contributed to the writing of the manuscript.

### 3.8 Supplementary information

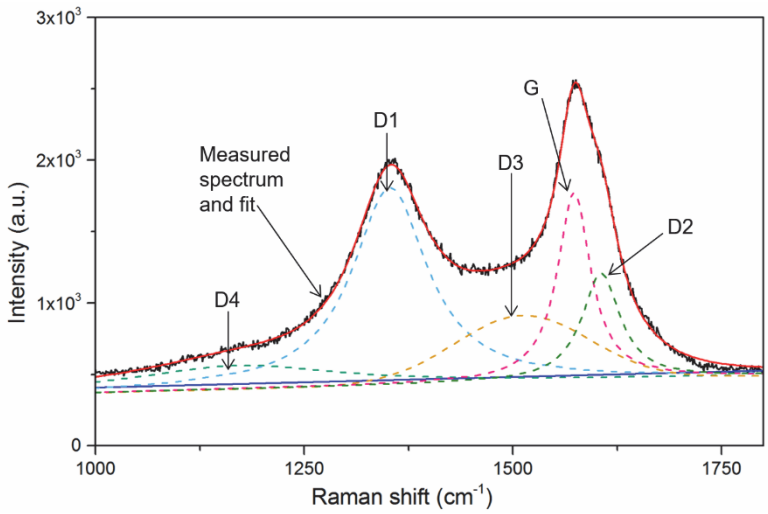


**Supplementary Figure 1. Raman spectra analysis to determine the graphitic character of carbon supports.** Raman spectrum obtained for the PS support post nitric acid treatment. Peak fitting was conducted using the method developed by Knauer et. al. consisting of 5 peaks—D1: disordered graphitic lattice carbon; D2: non-graphitic basic structural unit vibrations; D3: non-graphitic or molecular carbon; D4: non-graphitic basic structural unit vibrations; G: ideal graphitic lattice.[1]

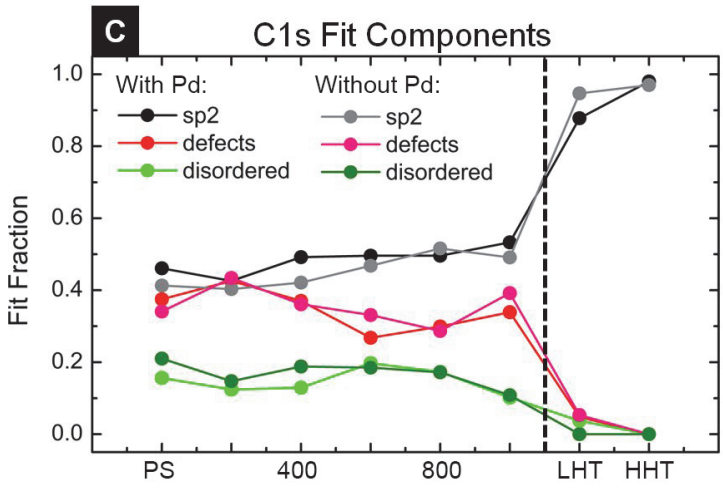


**Supplementary Figure 2. Defect and graphitic character analysis of carbon supports using XPS.** Evolution of the C1s fit components corresponding to $sp^2$ carbon, defective carbon (point-like defects), and disordered carbon (at edges and large vacancies) with annealing temperature. The data is based on deconvolved C1s spectra of the carbon supports with and without Pd acquired using synchrotron radiation for higher energy resolution and surface sensitivity. The fit fractions are normalized to the sum of all three fit components shown here.

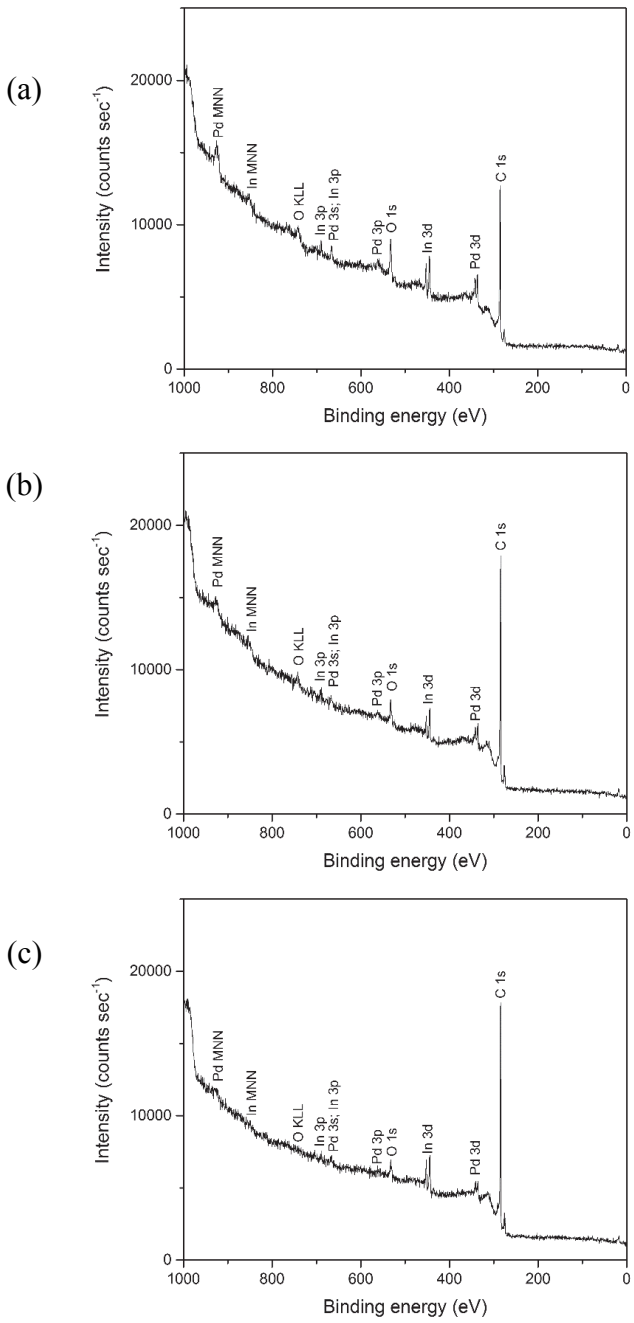


**Supplementary Figure 3. XPS survey spectra of the supports after treatment with nitric acid.** The detected signals correspond to C, O, Pd, and In (used as sample holder and internal standard) for the (a) PS, (b) LHT, and (c) HHT supports. The spectra confirm that the nitric acid treatment removed any inorganic impurities resulting from the synthesis and/or graphitization of the carbons supports.

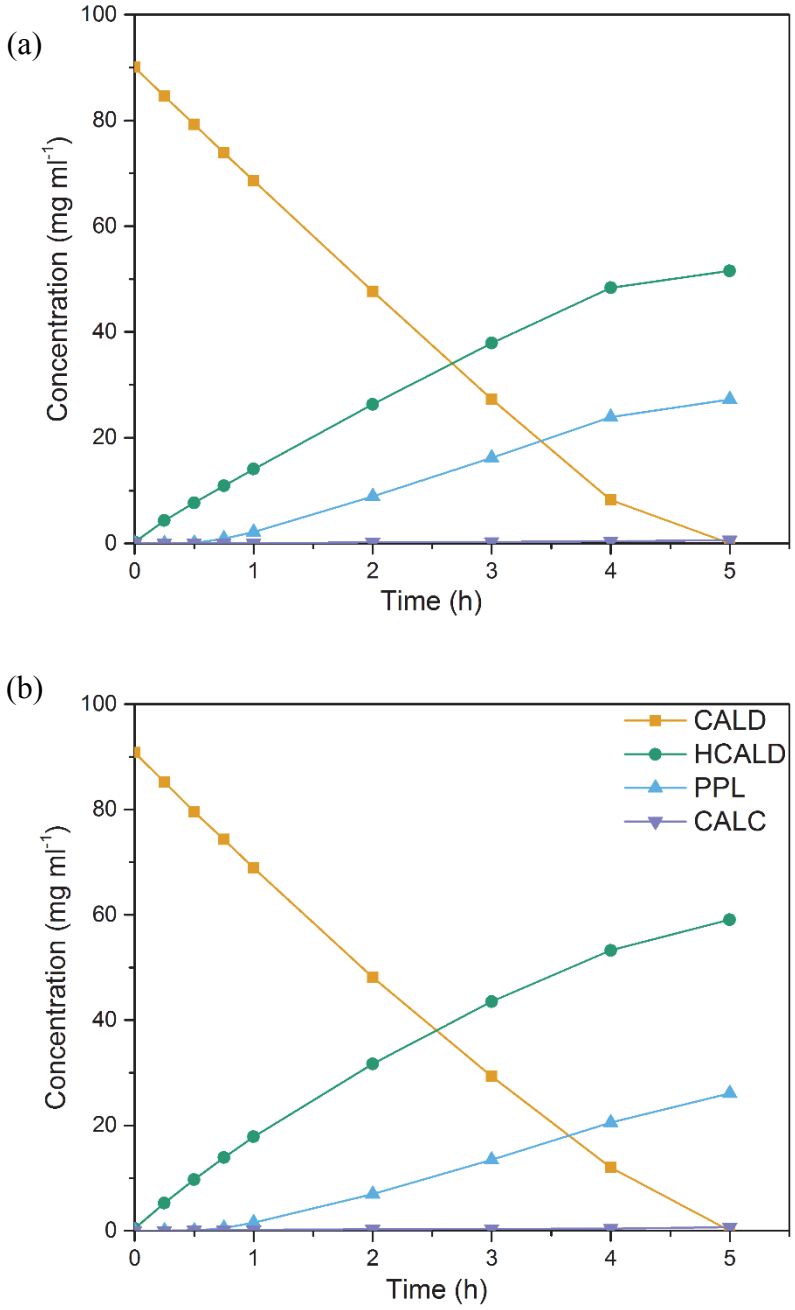


**Supplementary Figure 4. Catalytic reaction profiles for CALD hydrogenation.** Catalytic traces for (a) Pd/PS and (b) Pd/HHT catalysts for the batch reaction at 80 °C, hydrogen flowrate = 20 ml $min^{-1}$, stirring rate = 500 rpm, mass of catalyst = 100 mg, mass of cinnamaldehyde = 5 g.

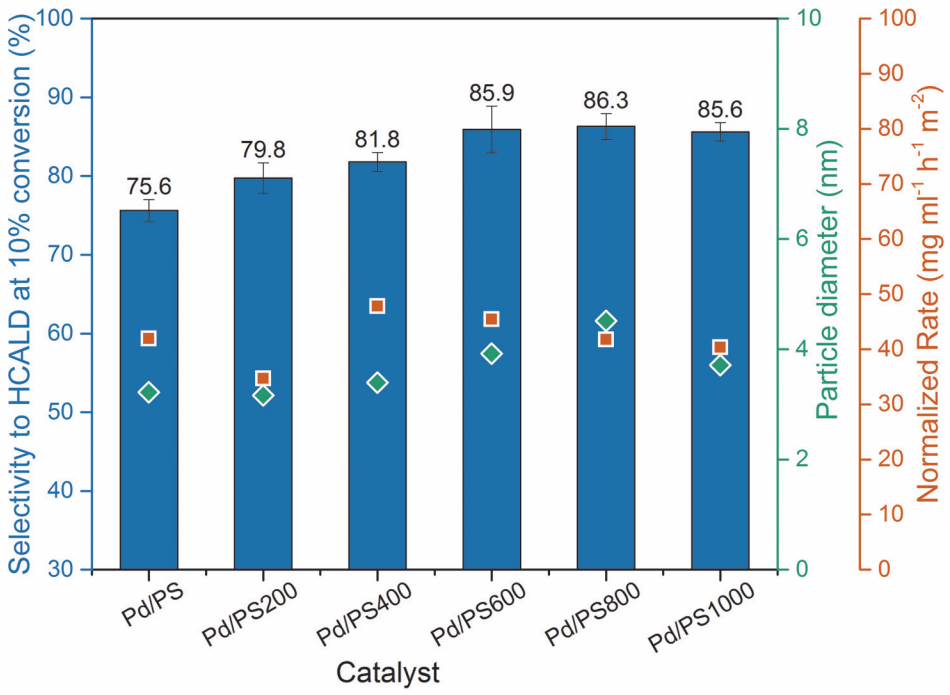


**Supplementary Figure 5. Trends in HCALD selectivity for Pd supported on PS-PS1000.** Selectivity to HCALD at 10% conversion of CALD for Pd supported on PS support and on PS defunctionalized at 200-1000 °C (blue). The values correspond to the average selectivity calculated for three independent experiments ± the corresponding standard deviation (s.d.). Comparing the selectivity results with Pd particle size (green) and normalized rate for CALD conversion (orange) shows no clear trend, indicating that the observed differences in selectivity are not due to obvious artefacts such as particle size effects.

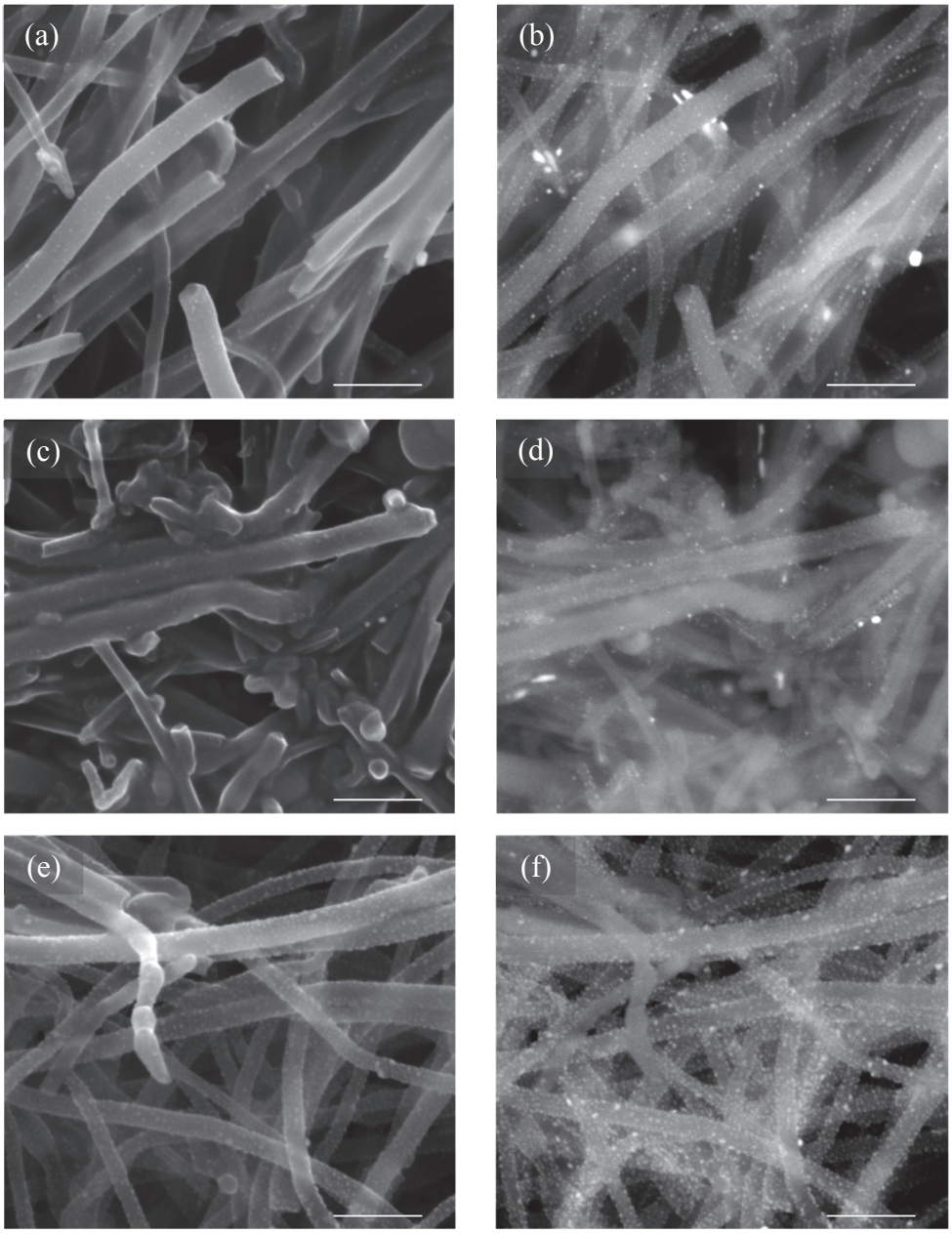


**Supplementary Figure 6. Distribution of palladium nanoparticles on carbon supports.** Scanning electron microscopy (SEM) images of the (a,b) Pd/PS400, (c,d) Pd/PS600, (e,f) Pd/PS800 showing the Pd dispersions typically achieved for the studied catalysts. Each region was imaged with both the secondary electron (SE) and back scattered electron (BSE) detectors for higher Z-contrast. A few large Pd particles were occasionally observed in these samples in BSE mode due to the higher sensitivity to heavy elements of this detector. Because of their low number and surface-to-volume ratio, these particles play an insignificant role in the present work. Scale bars in the images represent 500 nm.

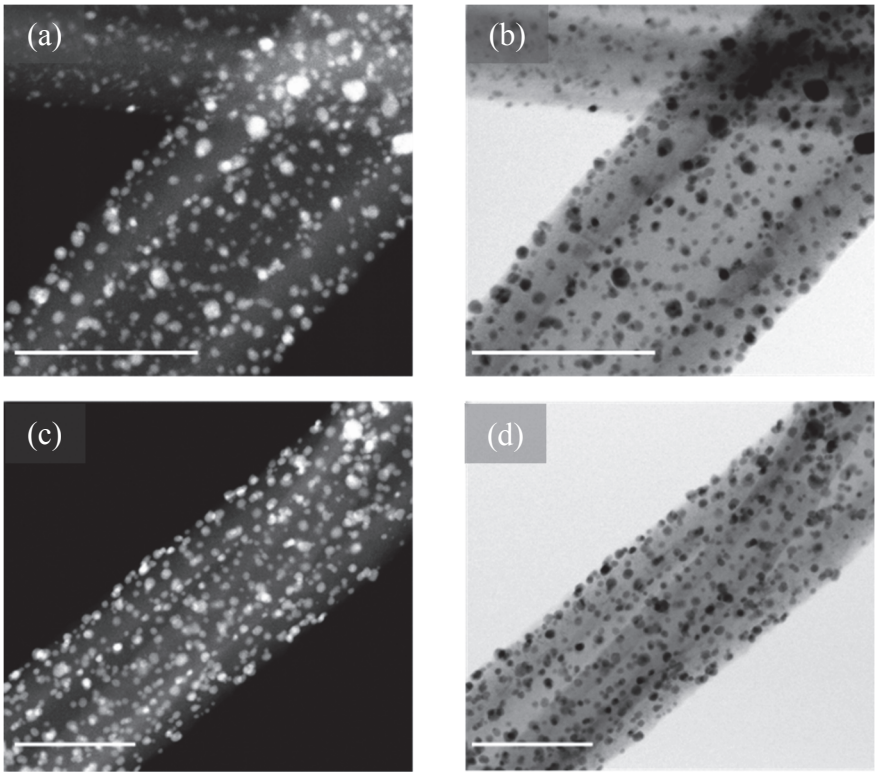


**Supplementary Figure 7. Representative transmission electron microscopy micrographs of Pd/SCCNT catalysts.** High resolution transmission electron microscopy (HRTEM) micrographs of (a,b) Pd/PS and (c,d) Pd/LHT acquired in high-angle annular dark-field (HAADF)-scanning transmission electron microscopy (STEM) mode (a,c) and bright field (BF)-STEM mode (b,d). Scale bars in the images represent 100 nm.

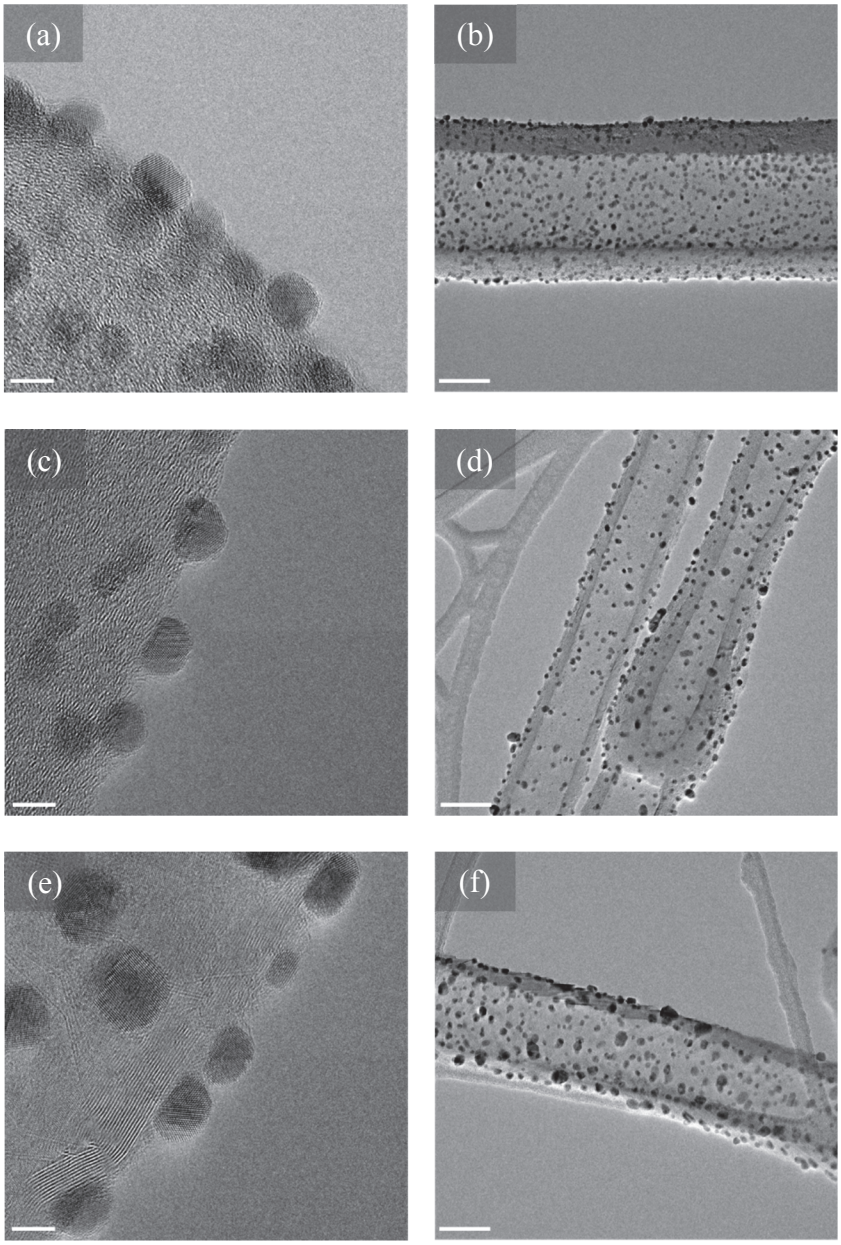


**Supplementary Figure 8. Representative transmission electron microscopy micrographs of supported Pd nanoparticles.** HRTEM micrographs of Pd nanoparticles supported on the (a,b) PS, (c,d) LHT, (e,f) HHT supports. Most Pd nanoparticles were hemispherical. Scale bars in the images represent 5 nm (a, c, and e) and 50 nm (b, d, and f).

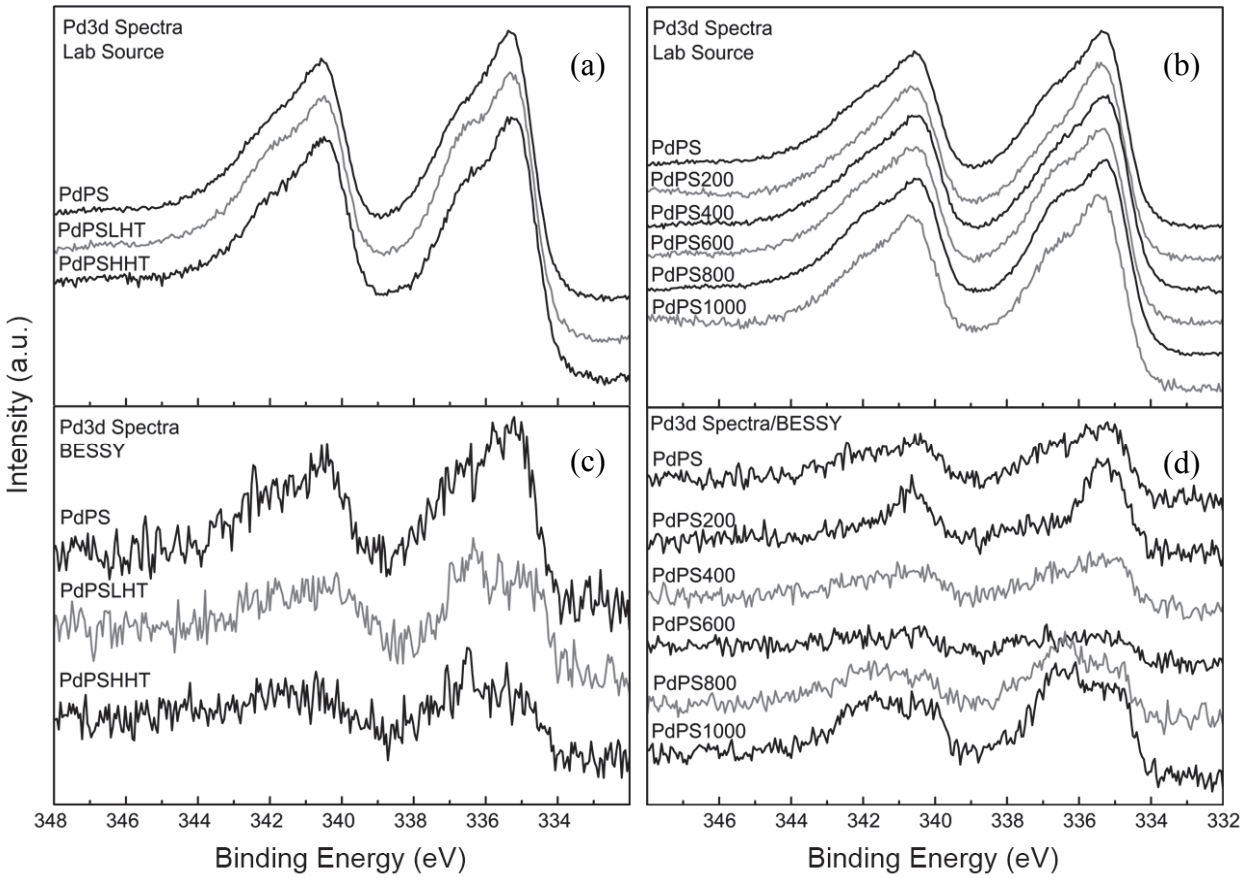


**Supplementary Figure 9. Lab source and synchrotron radiation based X-ray photoelectron spectra.** X-ray photoelectron spectra of Pd 3d using lab source (a, b) and synchrotron radiation (c, d). The spectra correspond to the Pd/PS-HHT series (a, c) and the Pd/PS200-PS1000 series (b, d). Note that single bunch operation uses a significantly lower ring fillings resulting in a beam current of ≤ 20 mA, which accounts for the relatively low signal-to-noise ratio for the synchrotron experiments.

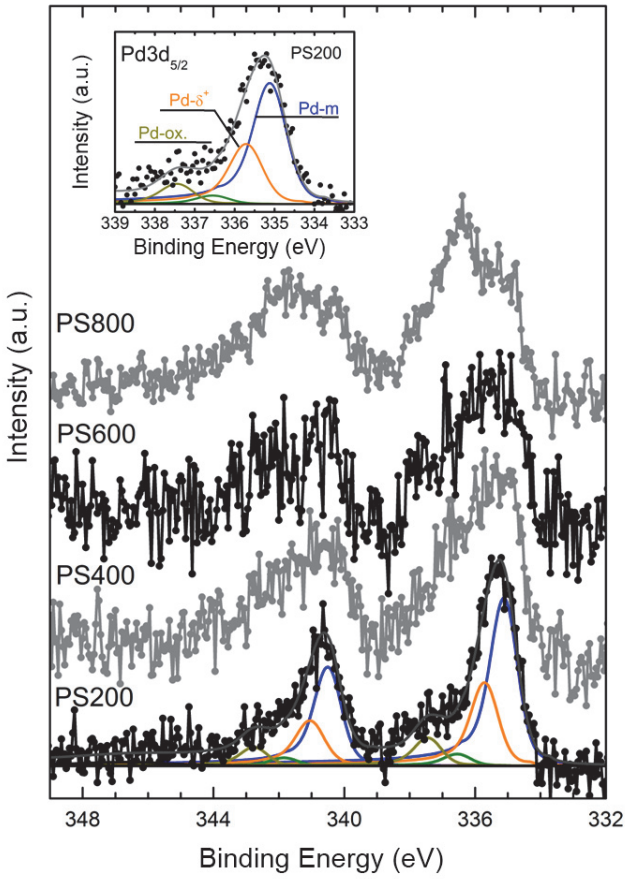


**Supplementary Figure 10. Synchrotron based X-ray photoelectron spectra.** X-ray photoelectron spectra of Pd/PS200 – Pd/PS800 catalysts using synchrotron radiation. The peak deconvolution for the Pd 3d 5/2 and 3/2 demonstrate the presence of Pd metal (blue), PdO and $PdO_2$ (green), and $Pd^{\delta+}$ (orange). Note that single bunch operation uses a significantly lower ring fillings resulting in a beam current of ≤ 20mA which accounts for the relatively low signal-to-noise ratio.

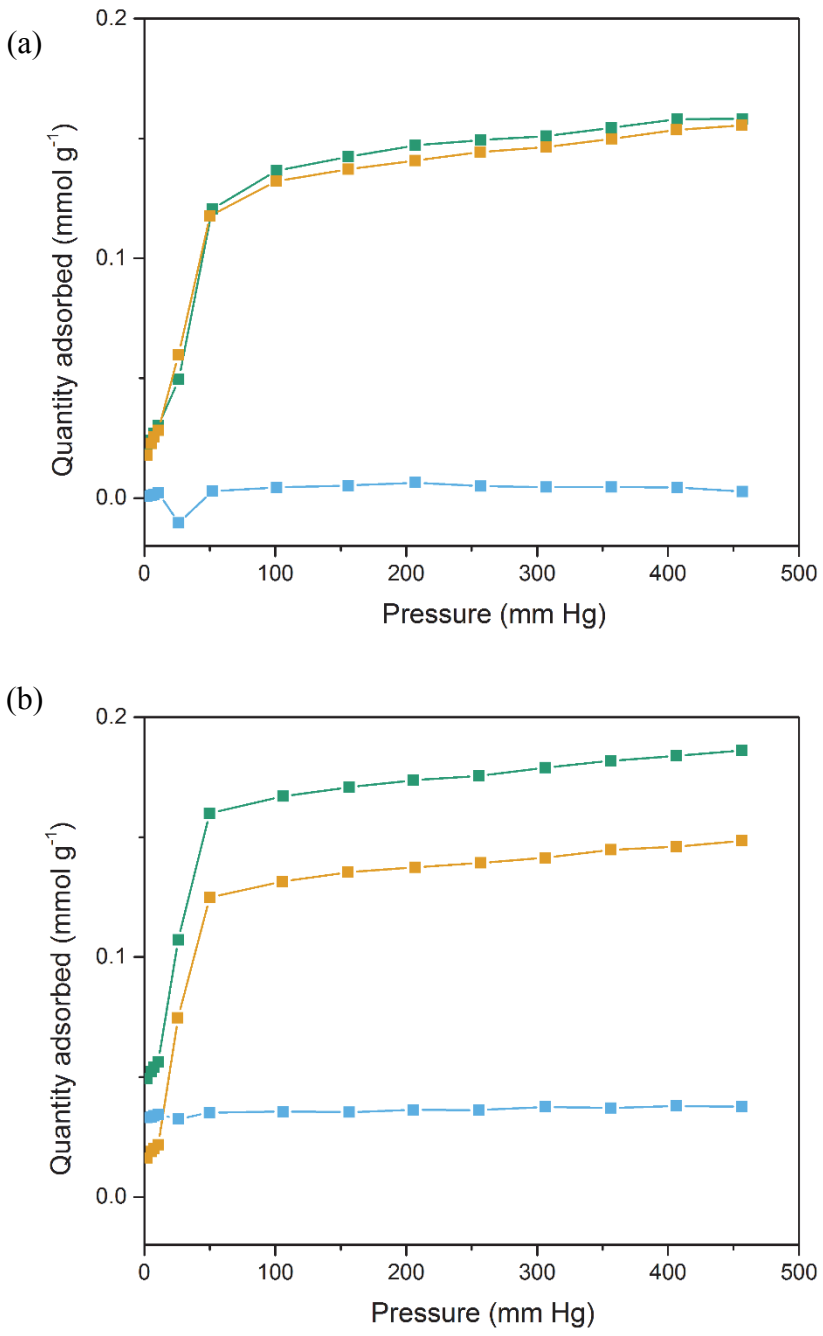


**Supplementary Figure 11. Support effects on hydrogen adsorption isotherms.** Hydrogen adsorption isotherms for (a) Pd/PS and (b) Pd/HHT catalysts. The graphs show the 1st adsorption isotherm (green), 2nd adsorption isotherm (orange), and the difference results (blue). Differences in reversibility can be observed for the Pd/PS and Pd/HHT catalysts. The ratios of the reversibly to irreversibly adsorbed hydrogen are given in the Supplementary Figure 12.

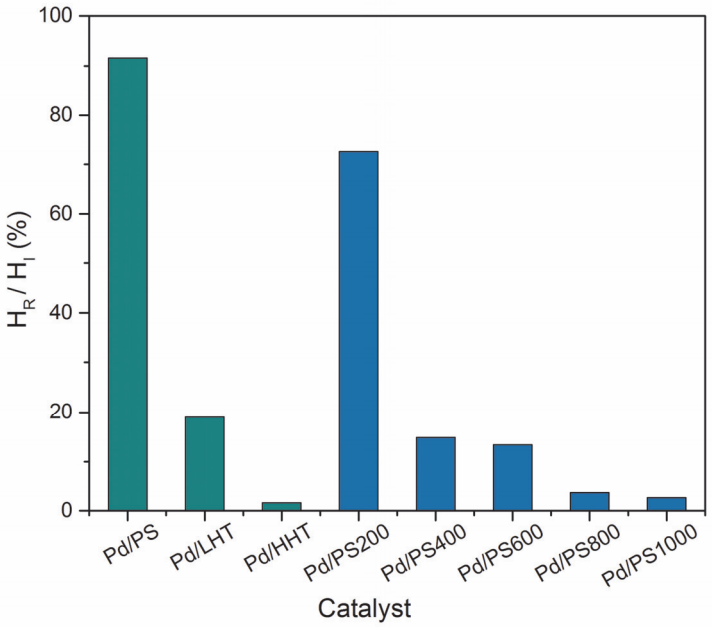


**Supplementary Figure 12. Differences in hydrogen adsorption properties for the studied catalysts.** Ratios of reversibly ($H_R$) and irreversibly adsorbed hydrogen ($H_I$) for the synthesized Pd/C catalysts.

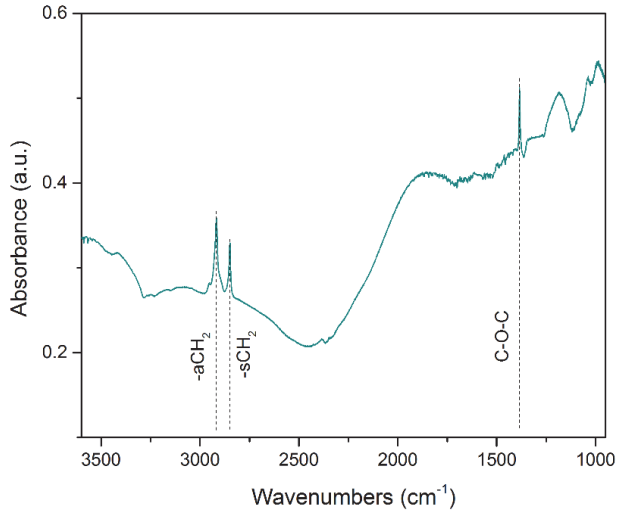


**Supplementary Figure 13. Representative infrared spectrum of Pd/SCCNT in the absence of $H_2$.** Infrared (IR) spectrum of the Pd/PS catalyst, recorded prior to $H_2$ exposure at room temperature, and referenced to the blank KBr pellet. The $–CH_2$ symmetric and asymmetric modes are observed at 2844 $cm^{-1}$ and 2916 $cm^{-1}$ and the C-O-C mode at 1385 $cm^{-1}$. The sample was activated under 1 bar of hydrogen at 100 °C for 1 h, then cooled down to room temperature for the IR measurements.

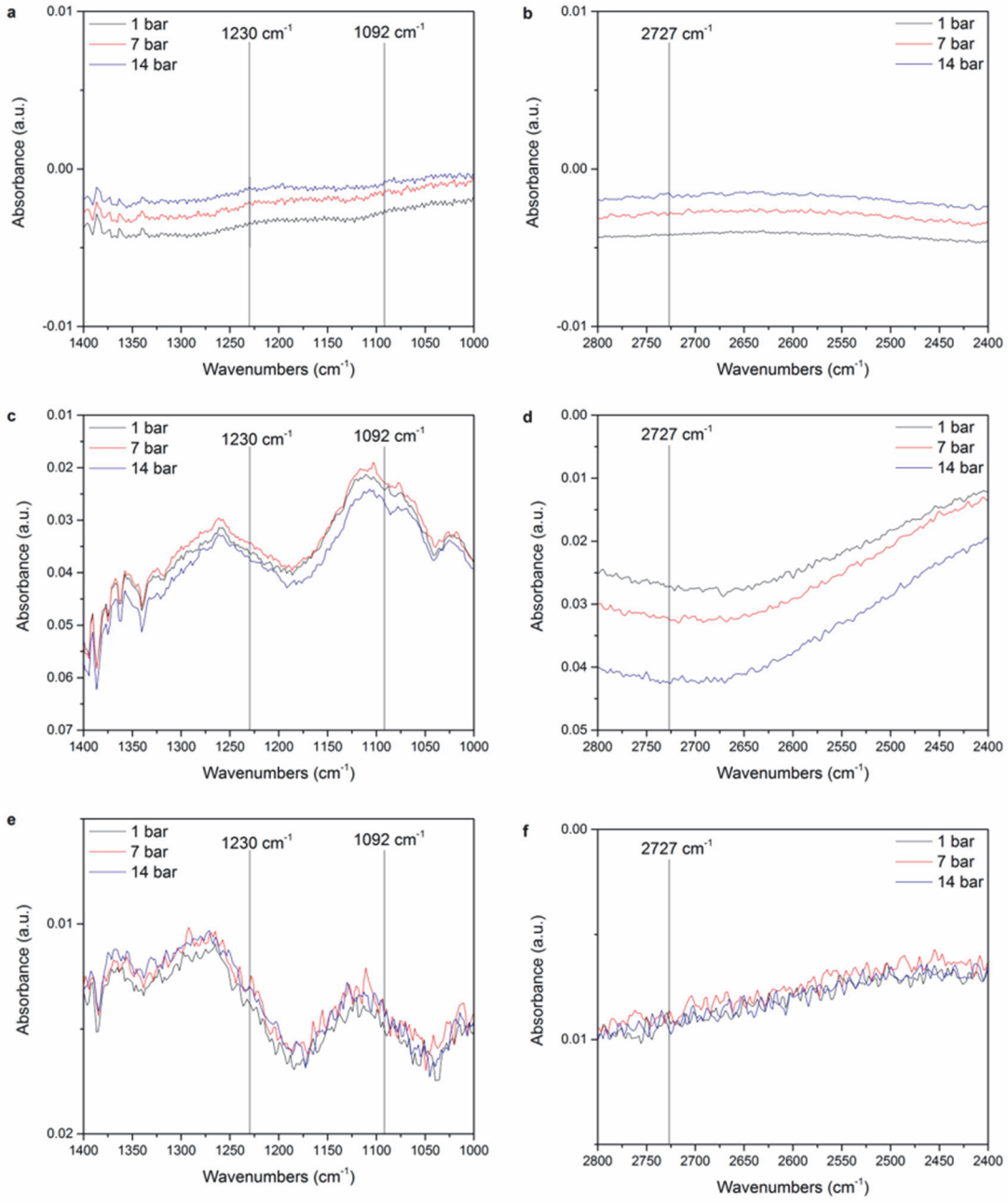
a
1 bar
7 bar
14 bar
1230 cm-1
1092 cm-1
Absorbance (a.u.)
Wavenumbers (cm-1)
b
2727 cm-1
c
d
e
f

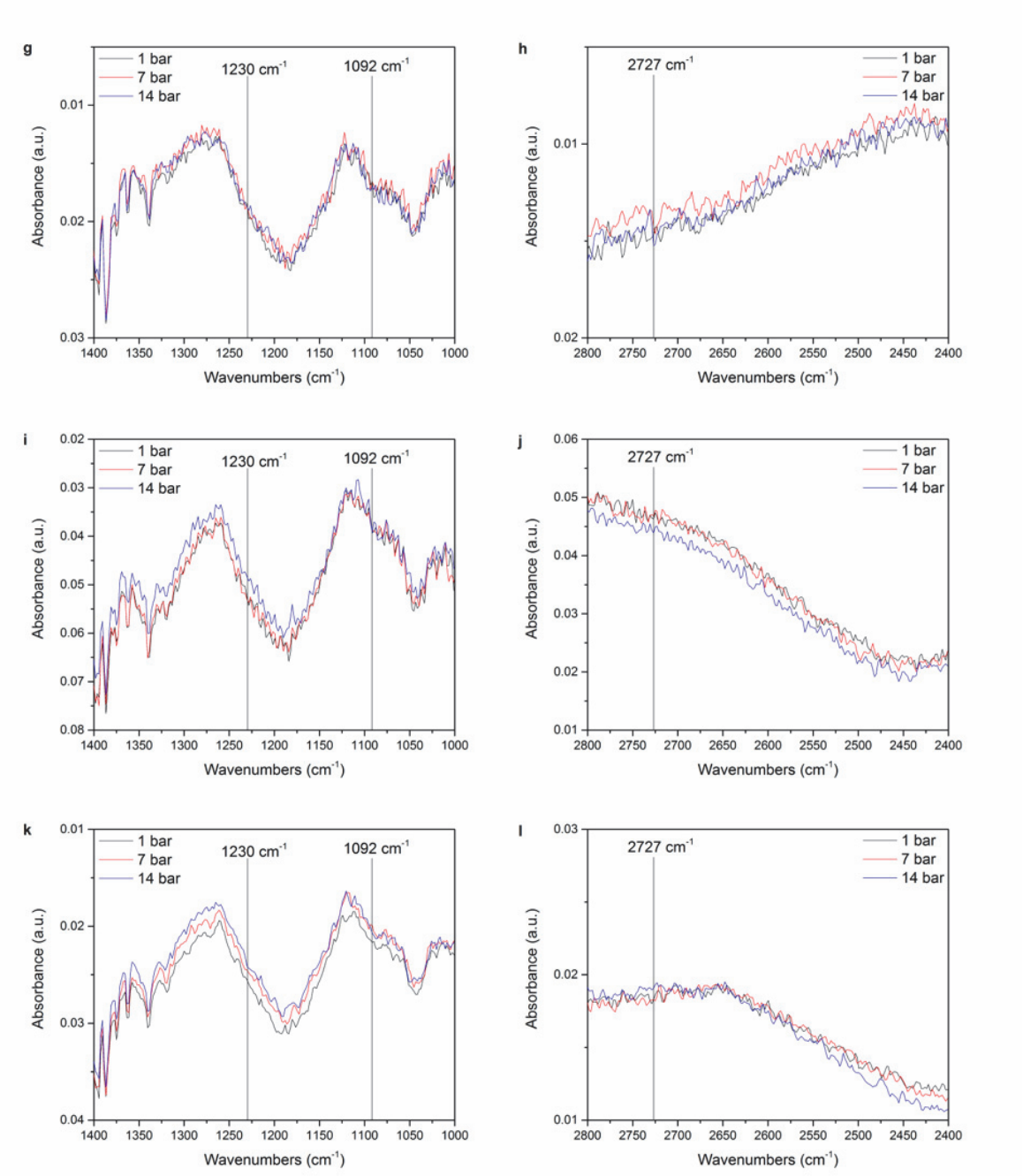


**Supplementary Figure 14. High-pressure infrared spectra (HP-FTIR) of Pd/SCCNT in the presence of $H_2$.** IR spectra of (a, b) Pd/PS, (c, d) Pd/LHT, (e, f) Pd/HHT, (g, h) Pd/PS200, (i, j) Pd/PS600, (k, l) Pd/PS1000 catalyst recorded under 1 (black), 7 (red), and 14 (blue) bar of hydrogen gas and subtracted from the corresponding spectrum recorded before exposure to $H_2$ at room temperature. Signals characteristic of the C-H modes at 2727 $cm^{-1}$, 1230 $cm^{-1}$, and 1092 $cm^{-1}$ are observed at 14 bar only. The signal-to-noise ratios for all modes are too low to determine if there is any hydrogen spillover at 7 bar. Prior to these measurements, the samples were activated under 1 bar of hydrogen at 100 °C for 1 h, then cooled down to room temperature for IR measurements.

**Supplementary Table 1. Effect of thermal treatments on the supports' graphitic character and functionalization.** Raman G-band/D1-band intensity ratios for the studied carbon supports and corresponding O1s/C1s ratios calculated from the highest intensity of the XPS spectra acquired using synchrotron radiation (BESSY II). These Raman and XPS results show the impact of annealing on the graphitic character and surface chemistry of the supports.

| Support | IG/ID[a] | O1s/C1s |
|---|---|---|
| PS | 0.43 | 0.24 |
| LHT | 1.25 | 0.06 |
| HHT | 5.83 | 0.03 |
| PS200 | 0.38 | 0.23 |
| PS400 | 0.40 | 0.23 |
| PS600 | 0.51 | 0.11 |
| PS800 | 0.62 | 0.15 |
| PS1000 | 0.62 | 0.09 |

[a] IG and ID represent the intensity of the G-band and D1 band respectively.

**Supplementary Table 2. Catalytic performance of the synthesized Pd/SCCNT samples at 10% conversion.** Hydrocinnamaldehyde (HCALD) selectivity, yield, and carbon balance at 10% cinnamaldehyde (CALD) conversion. The values correspond to the average calculated for three independent experiments ± the corresponding standard deviation (s.d.).

| Catalyst | HCALD Selectivity (%) | HCALD Yield (%) | Carbon balance (%) |
|---|---|---|---|
| Pd/PS | 75.6 ± 1.4 | 7.6 ± 0.1 | 99.4 ± 0.1 |
| Pd/LHT | 83.5 ± 2.7 | 8.3 ± 0.3 | 99.5 ± 0.9 |
| Pd/HHT | 83.2 ± 2.8 | 8.3 ± 0.3 | 99.7 ± 0.4 |
| Pd/PS200 | 79.8 ± 1.9 | 8.0 ± 0.2 | 99.6 ± 0.1 |
| Pd/PS400 | 81.8 ± 1.2 | 8.2 ± 0.2 | 99.7 ± 0.1 |
| Pd/PS600 | 85.9 ± 3.0 | 8.6 ± 0.3 | 99.9 ± 0.2 |
| Pd/PS800 | 86.3 ± 1.6 | 8.6 ± 0.2 | 99.8 ± 0.1 |
| Pd/PS1000 | 85.6 ± 1.2 | 8.6 ± 0.1 | 99.6 ± 0.1 |

**Supplementary Table 3. Catalytic performance of the synthesized Pd/SCCNT samples at 100% conversion.** Hydrocinnamaldehyde (HCALD) selectivity, yield, and carbon balance at 100% cinnamaldehyde (CALD) conversion.

| Catalyst | HCALD Selectivity (%) | HCALD Yield (%) | Carbon balance (%)[a] |
|---|---|---|---|
| Pd/PS | 58.4 | 58.4 | 96.5 |
| Pd/LHT | 73.0 | 73.0 | 101.8 |
| Pd/HHT | 67.4 | 67.4 | 101.0 |
| Pd/PS200 | 65.4 | 65.4 | 97.5 |
| Pd/PS400 | 66.4 | 66.4 | 105.2 |
| Pd/PS600 | 71.6 | 71.6 | 99.8 |
| Pd/PS800 | 72.4 | 72.4 | 106.7 |
| Pd/PS1000 | 75.7 | 75.7 | 103.3 |

[a] Carbon balance values calculated by accounting for the decrease in volume and moles due to sampling.

**Supplementary Table 4. Palladium metal loading on carbon supports.** Pd metal loadings determined by inductively coupled plasma-optical emission spectroscopy (ICP-OES).

| Catalyst | Pd metal loading (%)[a] |
|---|---|
| Pd/PS | 3.3 ± 0.3 |
| Pd/LHT | 4.2 ± 0.6 |
| Pd/HHT | 4.7 ± 0.2 |
| Pd/PS200 | 3.2 ± 0.3 |
| Pd/PS400 | 3.3 ± 0.1 |
| Pd/PS600 | 3.9 ± 0.2 |
| Pd/PS800 | 4.6 ± 0.5 |
| Pd/PS1000 | 3.9 ± 0.3 |

[a] All samples were analysed in quadruplicates to obtain the standard deviation.

**Supplementary Table 5. Palladium nanoparticles size.** Average particle sizes obtained from hydrogen chemisorption adsorption isotherms, aberration corrected transmission electron microscopy (TEM), and X-ray diffraction (XRD).

| Catalyst | Hydrogen chemisorption (nm) | TEM (nm) | XRD (nm) |
|---|---|---|---|
| Pd/PS | 4.86 | 5.6 ± 1.3 | 4.2 ± 0.3 |
| Pd/LHT | 5.04 | 8.2 ± 2.5 | 6.7 ± 0.3 |
| Pd/HHT | 2.99 | 6.2 ± 2.2 | 7.7 ± 0.4 |
| Pd/PS200 | 4.94 | - | 5.8 ± 0.4 |
| Pd/PS400 | 5.08 | - | 6.9 ± 0.4 |
| Pd/PS600 | 4.98 | - | 9.9 ± 0.6 |
| Pd/PS800 | 4.89 | - | 7.8 ± 0.6 |
| Pd/PS1000 | 4.81 | - | 6.7 ± 0.5 |

**Supplementary Table 6. Analysis of the charge transfer between the metal and carbon support.** Ratio of the $Pd^0/Pd^{\delta+}$ phase as observed from synchrotron based X-ray photoelectron spectroscopy (XPS) Pd 3d 5/2 peak components normalized to highest intensity.

| Catalyst | $Pd^0/Pd^{\delta+}$ |
|---|---|
| Pd/PS | 2.29 |
| Pd/LHT | 2.75 |
| Pd/HHT | 2.43 |
| Pd/PS200 | 2.00 |
| Pd/PS400 | 1.83 |
| Pd/PS600 | 1.62 |
| Pd/PS800 | 1.54 |
| Pd/PS1000 | 2.00 |

**Supplementary Table 7. Hydrogen chemisorption adsorption isotherms.** Hydrogen chemisorption results: amount of hydrogen adsorbed for the 1st and 2nd isotherm, difference results for Pd/C catalysts at 400 mm Hg hydrogen pressure, amount of reversibly adsorbed hydrogen, and ratio of reversibly to irreversibly adsorbed hydrogen.

| Catalyst | 1st adsorption isotherm- amount of hydrogen adsorbed (mmol $g^{-1}$) | 2nd adsorption isotherm- amount of hydrogen adsorbed (mmol $g^{-1}$) | Difference results (mmol $g^{-1}$) | Hreversible (mmol $g^{-1}$) | Hreversible/ Hirreversible |
|---|---|---|---|---|---|
| Pd/PS | 0.15812 | 0.15364 | 0.00448 | 0.00058 ± 0.00147 | 91.7 |
| Pd/LHT | 0.15603 | 0.14138 | 0.01465 | 0.00261 ± 0.00173 | 19.0 |
| Pd/HHT | 0.1839 | 0.14601 | 0.03789 | 0.03372 ± 0.00028 | 1.6 |
| Pd/PS200 | 0.1602 | 0.15352 | 0.00668 | 0.00072 ± 0.00138 | 72.7 |
| Pd/PS400 | 0.1529 | 0.14605 | 0.00685 | 0.00325 ± 0.00162 | 14.9 |
| Pd/PS600 | 0.16112 | 0.14593 | 0.01519 | 0.00367 ± 0.00140 | 13.4 |
| Pd/PS800 | 0.15294 | 0.13731 | 0.01563 | 0.01130 ± 0.00081 | 3.8 |
| Pd/PS1000 | 0.13679 | 0.12029 | 0.0165 | 0.01449 ± 0.00083 | 2.8 |

**Supplementary Table 8. Number of $Pd^{\delta+}$ atomic layers based on XPS.** The ratio of the $Pd^0/Pd^{\delta+}$ phase as observed from synchrotron based X-ray photoelectron spectroscopy (XPS) Pd 3d 5/2 peak components (Supplementary Table 6) was used to estimate the number of atomic layers impacted by the $Pd^{\delta+}$ phase in Pd nanoparticles. The values were calculated based on the following assumptions:

(a) the Pd nanoparticles are hemispherical and have a diameter of 5 nm, which corresponds to ~9 atomic layers (Supplementary Table 5)
(b) the particles are homogeneously covered with 2 atomic layers (~0.5 nm) of surface oxides
(c) the penetration depth of XPS under these conditions is ~2 nm
(d) all the Pd atoms at the interface are in the $Pd^{\delta+}$ state.

| Catalyst | Number of atomic layers impacted by $Pd^{\delta+}$ |
|---|---|
| Pd/PS | 1.56 |
| Pd/LHT | 1.34 |
| Pd/HHT | 1.50 |
| Pd/PS200 | 1.70 |
| Pd/PS400 | 1.80 |
| Pd/PS600 | 1.95 |
| Pd/PS800 | 2.01 |
| Pd/PS1000 | 1.70 |

### 3.9 Supplementary references

1. Knauer, M., Schuster, M. E., Su, D., Schlögl, R., Niessner, R. & Ivleva, N. P. Soot structure and reactivity analysis by raman microspectroscopy, temperature-programmed oxidation, and high-resolution transmission electron microscopy. *J. Phys. Chem. A* **113,** 13871-13880 (2009).

# CHAPTER 4

# EVIDENCE FOR TUNABLE ELECTRONIC METAL-SUPPORT INTERACTIONS IN CARBON-SUPPORTED PALLADIUM CATALYSTS

A manuscript in preparation for submission to Nature Catalysis

Radhika G. Rao[1,2], Raoul Blume[3], Mark Greiner[3], Axel Knop-Gericke[3], Robert Schlögl[3], Thomas W. Hansen[4], Kathleen Dreyer[5], David D. Hibbitts[5], & Jean-Philippe Tessonnier[1,2,*]

[1] Department of Chemical and Biological Engineering, Iowa State University, Ames, IA 50011, USA

[2] NSF Engineering Research Center for Biorenewable Chemicals, Ames, IA 50011, USA

[3]Max Planck Institute for Chemical Energy Conversion, Heterogeneous Reactions Group, DE-45470 Mülheim an der Ruhr, Germany

[4]Center for Electron Nanoscopy, Technical University of Denmark, DK-2800 Kgs. Lyngby, Denmark

[5]Department of Chemical Engineering, University of Florida, Gainesville, Florida 32611, USA

[*] Corresponding author

## Abstract

Synergies between the metal active phase and its oxide support were shown to enhance the rate of numerous reactions through electronic metal-support interactions (EMSI) or direct contribution of the support to the reaction, *i.e.* adsorption and activation of the reactant. Such effects are unknown for carbon scaffolds and, in many studies, carbon is chosen as a support due to its expected inertness. Here, we report that conventional carbonaceous materials do present EMSI effects that alter the intrinsic rate of precious metal atoms at the interface by up to two orders of magnitude compared to the corresponding bulk

metal. We also demonstrate that oxygen-containing functional groups that are ubiquitous on carbon surfaces act as surface dipoles that alter the electronic properties of the surface. Controlling the scaffold's surface chemistry allows to tune the work function from 5.1 eV to 4.5 eV and, hereby, the intensity of the charge redistribution at the metal-carbon interface and the catalytic activity of the corresponding metal atoms.

## 4.1 Introduction

Tailoring the electronic structure of a catalyst support offers unique avenues for fine-tuning the activity of the metal nanoparticles decorating its surface.[1-2] These phenomena, which occur at the interface are responsible for the so-called metal support interactions (MSI), are well-documented for the metal-graphene systems. While the understanding of strong metal support interactions (SMSI) for oxides and their impact on catalytic activity have been well-established, similar translation of MSI effects to catalytic performance for carbon nanomaterials still remains elusive.[1-4] Carbon supported catalysts have been reported to demonstrate differences in selectivity when compared with the conventional oxide supports, such as silica and alumina.[5-8] These differences in catalytic performance have been attributed to the non-innocent role that carbon scaffolds play on the supported metal active phase.[7-8] Conventionally, these effects are associated with MSI, an umbrella term that encompasses the current gaps in knowledge but the factors that govern these interactions still need to be investigated in detail. Additionally, although hundreds of commercial carbons with controlled graphitic character, surface chemistry, and porosity have been developed, the choice of a specific carbon support for a target reaction is typically based on empirical criteria due to the co-existence of electronic and chemical (hydrophilic/hydrophobic) effects.[9-10] These challenges act as a major roadblock for the rational design of carbon

supported catalysts, which is vital for the production of specialty and fine chemicals through renewables routes. Specifically, noble metal nanoparticle catalysts supported on carbon materials are of prime importance due to their applications in hydrogenation reactions, which represent a multi-billion dollar industry for the petroleum-based production of chemicals and are expected to play a similar role in the bio-based chemical industry.[7-8, 11-13] Due to this impact of carbon-supported catalysts, there is a pressing need for understanding the MSI effects that govern their performance.

Several studies in the past have reported the presence of MSI effects for hydrogenation catalysts with carbon scaffolds. Despite these efforts, the reports heavily focused on the chemical effects, such as adsorption and polarity, of supports on catalytic performance but the electronic interactions were not analyzed in sufficient depth.[14-18] However, it is now well-established that the presence of heteroatoms can change the local electronic properties of graphene and graphenic carbons. This understanding invoked curiosity for further scrutiny of the impact of support properties on the metal active-phase by revisiting the Pd/C catalyst. A detailed analysis of the literature demonstrates that due to the structural and chemical complexity of the materials, previous attempts could not completely deconvolve the electronic, polar and acid-base interactions to assess their impact on substrate adsorption and activation.[19-20] Decoupling the electronic and chemical interactions is a pre-requisite for understanding the structure-property relationships that link atom hybridization, structure, and functional group compositions to MSI and catalytic activity, which is in turn key to establish general rules for rational catalyst design. Recently, our group successfully deconvolved the correlations between the graphitic character and chemical nature of carbon supports and unraveled their influence on the catalytic performance of Pd nanoparticles

decorating their surface.[21] While the study offered elite strategies for tuning the electronic metal-support interaction (EMSI) effects, the utilization of this knowledge for the rational design of carbon-supported catalysts requires a deeper understanding of these interactions. Specifically, clearly identifying the active site of the reaction and elucidating the influence of support properties on these sites is vital for designing novel catalysts. Therefore, developing new routes that can help in understanding and controlling the interactions between the support and the metal active site are required.

In order to develop a more sophisticated handle on the properties of the catalyst and thereby its performance, herein the structure of the support and metal nanoparticles was controlled at the nanoscale using simple thermal treatments. Firstly, stacked cup carbon nanotube (SCCNT) supports were annealed for tuning the amorphous carbon content on their surface along with the support graphitization. These alterations in the support properties were coupled with modifications in the Pd particle size for elucidating the influence of EMSI effects at the interface and nanoparticle surface. Testing the catalysts for the liquid-phase hydrogenation of α,β-unsaturated aldehyde – cinnamaldehyde, revealed correlations between the annealing temperatures, support properties, metal nanoparticle size, MSIs, and catalyst performance. The strategies developed in this work allowed us to clearly identify the active sites for the hydrogenation of cinnamaldehyde. Our work provides deeper insights into the EMSI effects and offers routes for engineering next-generation α,β-unsaturated aldehyde hydrogenation catalysts. The results of our study are expected to be applicable for the development of a variety of hydrogenation catalysts and thereby lead to a broader impact in several domains such as biomass conversion, organic chemistry, and green chemistry.

## 4.2 Results

### 4.2.1 Initial Considerations on Metal-support Interactions in Pd/C Catalysts

Trends between catalytic activity and the support's surface chemistry have been established for carbon-supported precious metal catalysts. However, the mechanisms by which topological defects and heteroatom-containing functional groups alter the catalytic activity of the supported metal atoms are still debated. Several groups proposed that polar functional groups alter the hydrophilic-hydrophobic character of the surface, hereby influencing the reactants' adsorption mode and, as a result, the rate and selectivity of the reaction. For the hydrogenation of cinnamaldehyde, an $\alpha,\beta$-unsaturated model compound, this interpretation is supported by infrared spectroscopy measurements, which revealed a strong correlation between the support's surface polarity, cinnamaldehyde's adsorption mode, and the C=C/C=O selectivity for the hydrogenation reaction. However, theoretical calculations that support this causal connection are still missing. Therefore, it cannot be excluded that the observed switch in cinnamaldehyde's adsorption mode is the *consequence* of a change in the electronic structure of the metal active phase rather than the *cause* of the observed differences in selectivity.

Alternatively, several groups have instead proposed that the observed differences in catalytic activity are due to ligand effects. The oxygen-containing functional groups that decorate the structural defects of carbon surfaces could bind to the metal active phase and alter its electronic structure through charge transfer.[22] In the ligand field theory, electronic density can either flow from the ligand to the metal or from the metal to the ligand depending on the position of its molecular orbitals, hence the nature of the ligand. This interpretation is also consistent with the shifts in binding energy observed by XPS for Pd and Pt nanoparticles

supported on functionalized carbons.[23] However, for the ligand field theory to apply, the orbitals of the transition metal atoms and of the ligands must overlap. This implies that each transition metal atom must be within metal-ligand bonding distance of at least one functional group, which becomes increasingly unlikely as the O/C ratio at the surface decreases. However, we have recently demonstrated that carbon support effects remain relevant upon annealing at 600 °C, *i.e.* a temperature at which the thermal decomposition of oxygen-containing functional groups is significant. Therefore, we conclude that none of the interpretations proposed so far accurately describe the chemical and electronic effects that take place at the metal-carbon interface. Moreover, in the case of studies performed for precious metals supported on activated carbon, diffusion limitations and confinement in the support's micropores may also contribute to the differences in catalytic activity that have been reported.[24]

### 4.2.2 Design of a Carbon Platform for the Experimental and Theoretical Investigation of Metal-carbon Support Interactions

Stacked-cup carbon nanotubes (SCCNTs) provide key advantages over other carbon supports for investigating metal-carbon interfacial phenomena and their impact on catalysis.[21] In contrast to activated carbon, which presents a complex 3-dimensional pore system with a large fraction of micropores, SCCNTs exhibit a tubular shape with a single cylindrical ~40 nm mesopore extending along the main axis of the nanotube.[25] From a reactivity standpoint, this morphology enables a fast diffusion of reactants and products and an excellent access to the metal nanoparticles decorating the carbon surface, making it easy to compare the performance of SCCNT-supported catalysts. From an advanced

characterization perspective, the smooth carbon surface also facilitates the high-resolution imaging of the metal nanoparticles and of the metal-carbon interface. But SCCNTs' key advantage is that these nanotubes consist of a graphitic core wrapped with a pyrolytic carbon shell (Figure 1). This shell consists of highly defective 1-2 nm sheets similar to the basic structural units found in activated carbon and carbon black, and that self-assembled on the graphitic core to form an homogeneous ~10 nm layer (PS sample). This layer can be thermally annealed until reaching a nearly defect free graphitic state at 3000 °C (HHT sample). Hence, the structure and surface chemistry of the selected SCCNTs can be tuned without altering their morphology, specific surface area, and porosity,[25-27] hereby offering a unique platform for studying metal-carbon support interactions. This platform also presents advantages for theoretical calculations as the system can be accurately modeled as a defective graphenic sheet for which defect density and concentration of oxygen-containing groups decorating the defects can be easily modulated.

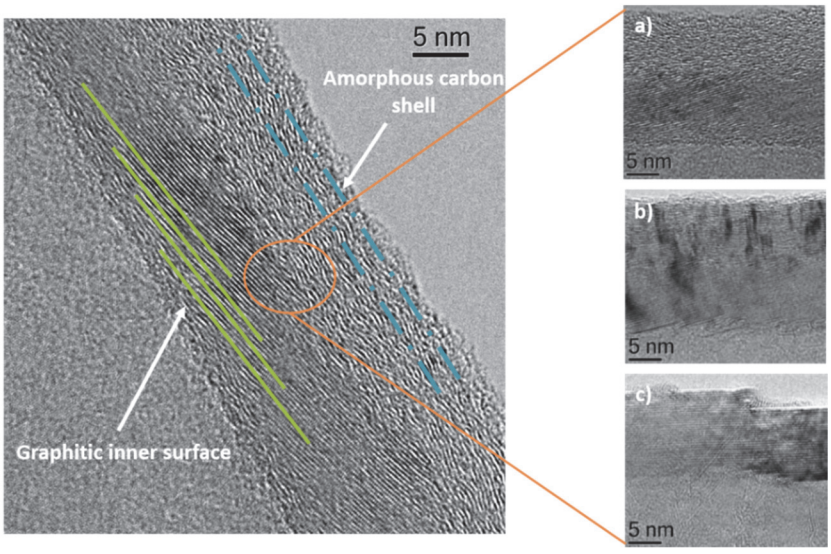


**Figure 1.** Transmission electron microscopy image of SCCNT catalysts depicting its dual structure. The supports demonstrate an increase in the graphitic inner surface with annealing temperature of a) 700 °C, b) 1500 °C, and c) 3000 °C

### 4.2.3 Evidence for Electronic Metal-carbon Support Interactions and Interfacial Charge Redistribution

We built the present study on intriguing catalytic results obtained for cinnamaldehyde hydrogenation using Pd/SCCNTs with different levels of carbon surface functionalization.[21] These early results revealed strong correlations between the scaffold's surface chemistry, the selectivity to the C=C hydrogenation product hydrocinnamaldehyde, the reversibility of the hydrogen chemisorption process (double isotherm method), and the presence of an electron-depleted $Pd^{\delta+}$ contribution in the X-ray photoelectron spectra (XPS) of the tested catalysts. Theoretical calculations shed light on these correlations as QUAMBO charge analysis revealed that Pd atoms bound to oxidized carbon supports are positively charged as a result of a charge redistribution at the metal-carbon interface. However, these correlations remained qualitative at best and the contribution of a non-stoichiometric palladium suboxide ($PdO_x$) phase could not be ruled out using *ex situ* XPS due to the exposure of the samples to air. Therefore, we started the present work with an *in situ* near ambient pressure XPS (NAP-XPS) investigation of the Pd active phase under reducing conditions.

Palladium was deposited on defective SCCNTs (PS support) prior to the NAP-XPS experiment. We preferred the incipient wetness impregnation method over other deposition techniques in order to minimize the number of chemicals and ligands that may subsequently influence the catalytic activity of the metal sites. Hence, all the samples were prepared with a nominal loading of 5 wt.% Pd using an aqueous solution of palladium nitrate. This precursor decomposes at low temperature, below 200 °C,[28] and yields ~5 nm $Pd^0$ nanoparticles free of contaminants (*e.g.* chlorides) upon reduction in hydrogen at 400 °C (Supporting Information).[29]

For the NAP-XPS experiment, the catalyst precursor $Pd(NO_3)_2$/PS was first calcined in 0.3 mbar of oxygen at 250 °C, cooled down in vacuum, then treated in 0.3 mbar of hydrogen at 80 °C and ramped to 400 °C at 10 °C/min to reproduce the conditions used in laboratory experiments. The high flux of photons supplied by the BESSY II synchrotron enabled us to continuously monitor the evolution of the carbon support (C1s, O1s) and of the palladium active phase (Pd3d) over the course of the experiment, hence identify relationships between the metal's oxidation states and the support's surface chemistry. As for most nitrates, the palladium precursor decomposed a low temperature, ~80 °C, leaving Pd atoms in various oxidation states on the scaffold's surface upon calcination in oxygen. Further heating in $H_2$ converted the metal oxides to metallic $Pd^0$, as confirmed by the lack of signal 336.1 eV in the Pd3d spectra and the sharp drop in signal at 530.2 eV in the O1s spectra (Figure S1). Upon reduction at 400 °C, the Pd3d spectra showed a main contribution at 335.1 eV (Figure 2a) consistent with the binding energy reported in the literature for bulk $Pd^0$.[30] However, an additional signal at 335.95 eV was needed to fit the spectra. This binding energy is inconsistent with the values reported for $Pd^+$ (~335.5 eV) and $Pd^{2+}$ (336.3-336.9 eV), for both Pd oxides and carbides. In addition, the chemical shift for the $3d_{5/2}$ core level is +0.85 eV, hence significantly higher than the +0.18 eV observed for Pd hydride.[31] The valence band spectra were also lacking the states with substantial d character at 8 eV that were reported for PdH.[32] These results, along with the changes in intensity of the 335.95 eV signal observed with increasing temperature, support the presence of a $Pd^{\delta+}$ phase that arises from a charge redistribution at the Pd-C interface and that is sensible to the concentration of oxygen-containing functional groups decorating the scaffold's surface.

Our previous DFT calculations and QUAMBO charge analysis revealed that these electronic effects are the strongest within the first two atomic layers near the interface and decay rapidly with increasing distance. However, the electronic perturbation remains strong enough to extend throughout ~2.5 nm Pd nanoparticles and alter the chemisorption of hydrogen and oxygen at the apex of the metal particle by 50 kJ $mol^{-1}$.[21] Therefore, it remained unclear whether the experimentally detected $Pd^{\delta+}$ phase is solely present near the interface or is more broadly distributed, *e.g.* forming a shell around a $Pd^0$ core. To address this question we performed an *in situ* XPS depth profiling analysis by varying the energy of the incident photons from 780 eV to 480 eV, which corresponds to varying analysis depth (Figure 2b). Deconvolution of the corresponding XPS spectra revealed an increase in the $Pd^{\delta+}/Pd^0$ ratio from 0.44 to 0.5 with increasing analysis depth, consistent with strong interfacial phenomena that decay with increasing distance from the support. These electronic effects are significant near the interface as they alter the atom's core electrons and induce a perturbation similar to a change in oxidation state.

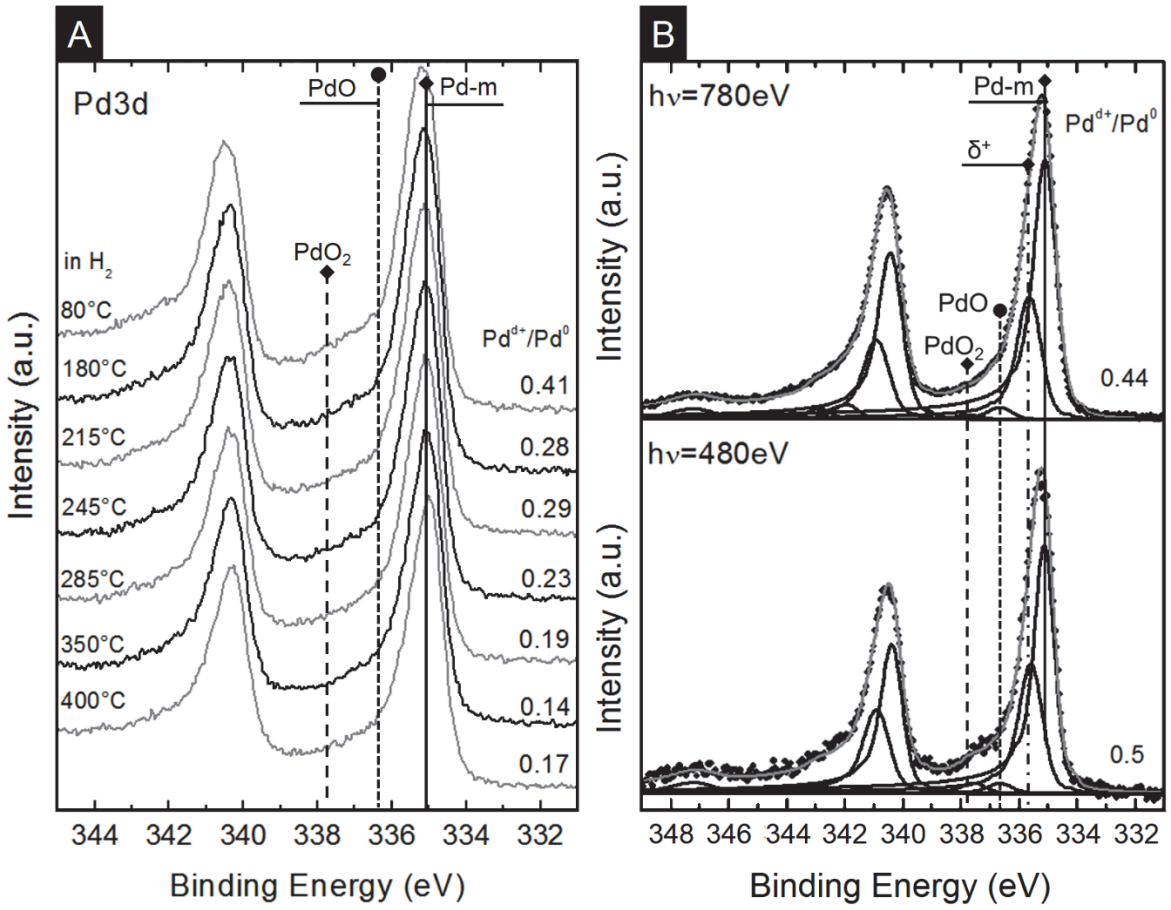


**Figure 2.** (a) Synchrotron XPS Pd3d spectra of the $Pd(NO_3)_2$/PS catalyst precursor collected during *in situ* calcination in 0.3 mbar $O_2$ and heating at 10 °C/min in 0.3 mbar $H_2$. The corresponding $Pd^{\delta+}/Pd^0$ ratio is marked next to each spectrum. (b) XPS depth profiling spectra of the Pd/PS sample after reduction in $H_2$ at 400 °C. The corresponding $Pd^{\delta+}/Pd^0$ ratio for each analysis depth is marked next to each spectrum.

### 4.2.4 Consequences on Palladium's Catalytic Activity

We started this part of the work by investigating how the interfacial charge distribution affect the rate of the reaction. To this end, Pd nanoparticles were deposited on oxidized SCCNTs (Pd/PS sample) and the particle size was tailored by subsequent annealing in nitrogen for 2 hours at temperatures ranging from 400 to 850 °C. The variations in the annealing temperature and thereby the particle size were introduced to strategically control the metal-support interactions and identify the reactive sites. Approaches involving the

variations in metal loading or ligand-based synthesis were not considered for tuning the particle size due to the challenges associated with these techniques, such as steric effects of the ligands.[33-34]

Comparing the reaction rates of the obtained catalysts at 10% CALD conversion revealed a strong dependence on the particle size obtained from hydrogen chemisorption (Figure 3). The observed change in rate cannot be explained by geometric effects, *i.e.* a change in metal surface area, as normalizing the rates with the Pd surface area determined by hydrogen chemisorption only had a marginal effect on the trend (Figure 3). These differences in rates were not a result of variations in palladium loading either as elemental analysis confirmed that the metal loading was uniform across all samples (Table S1). This result was unexpected as cinnamaldehyde hydrogenation was demonstrated to be a structure insensitive reaction, meaning that particle shape and local coordination number of surface atoms have no effect on turnover frequency (TOF) when the metal nanoparticles decorate an inert support such as silica.[35] For annealing temperatures ≥850 °C, the drop in reaction rate may be explained by the partial encapsulation of the metal nanoparticles with carbon. Aberration-corrected transmission electron microscopy (ac-TEM) performed on samples annealed at 850 and 1000 °C revealed that carbon atoms from the defective support become mobile at high temperature and migrate onto the metal nanoparticles (Figure S2). This phenomenon also explains that chemisorption overestimated the metal particle size compared to XRD for these two samples. However, at lower annealing temperatures, the metal surface was found to be free of carbon and the observed drop in normalized rates was free from artifacts. In contrast, annealing the support in inert atmosphere *prior* to Pd deposition had no effect on the normalized rates (Figure 3). These results suggest more complex support effects that solely

take place at the Pd-C interface and that are directly correlated to the area of the metal-carbon contact.

As our NAP-XPS depth profiling experiment revealed the presence of a $Pd^{\delta+}$ phase at the interface between the metal nanoparticles and the support, we further studied the contribution of the $Pd^{\delta+}$ phase to the observed catalytic activity for the two Pd/SCCNT sample series with pre- and post-synthetic annealing. We have already demonstrated that when annealing is performed prior to Pd deposition, the $Pd^{\delta+}/Pd^0$ ratio increases with the annealing temperature and is directly correlated with the concentration of oxygen-containing functional groups decorating the scaffold's surface.[21] Assuming hemispherical particles, a simple calculation using the relative ratio of $Pd^{\delta+}$ and $Pd^0$ contributions in the Pd3d spectra showed that only the first 1-2 atomic layers near the interface are impacted by the charge transfer for ~5 nm particles. Hence, the variations in the $Pd^{\delta+}/Pd^0$ ratio are not sufficient to significantly alter the number of $Pd^{\delta+}$ atoms at the interface and the rate of the reaction remains unaltered throughout this sample series (Figure 3). However, when the annealing step is carried out after Pd deposition, the thermal treatment also favors the sintering of the Pd nanoparticles, increasing their average size from 4.6 to 23.9 nm. The inverse dependence between particle size and Pd atoms at the interface leads to a sharp drop in the $Pd^{\delta+}/Pd^0$ ratio and of the interfacial effects on catalytic activity. This explains why the TOF drops rapidly for samples annealed at 400 and 550 °C but remains within error bars for higher annealing temperatures. These results implicitly confirm that cinnanmaldehyde hydrogenation is structure insensitive when the support is inert or has a minimal effect on the metal active phase, in agreement with previous works, and reveals that the charge redistribution at the Pd-C interface boosts the catalytic activity.

This interpretation is further supported by hydrogen chemisorption results using the double isotherm method. For both sample series, the ratio of reversibly and irreversibly chemisorbed hydrogen ($H_{irrev}/H_{rev}$) followed the exact same upward trend as $Pd^{\delta+}/Pd^{0}$ with increasing annealing temperature, which indicates that $Pd^{\delta+}$ binds hydrogen more strongly than $Pd^{0}$. The strong hydrogen binding did not alter the rate of the reaction (*vide infra*) but altered the selectivity of the reaction by preventing the over-hydrogenation of cinnamaldehyde to phenylpropanol. Conversely, for samples prepared by post-synthetic annealing, hydrogen chemisorption became more reversible with increasing annealing temperature, in agreement with the decreasing $Pd^{\delta+}/Pd^{0}$ ratio. As discussed previously, the interfacial charge distribution plays a minor role for this sample series and the metal's adsorption properties as well as rate and selectivity are essentially the same as for bulk Pd. The influence of the $Pd^{\delta+}$ phase also explains the contradiction between our trends and the results of Jiang et al on particle size effects for $Pd/Al_2O_3$ catalysts.[36] In contrast to the δ+ phase for Pd/C catalysts, $Al_2O_3$ supported catalysts exhibit a $Pd^{\delta-}$ phase, which based on our interpretation would bind hydrogen more weakly and lead to a lower selectivity to hydrocinnaldehyde.[36-37]

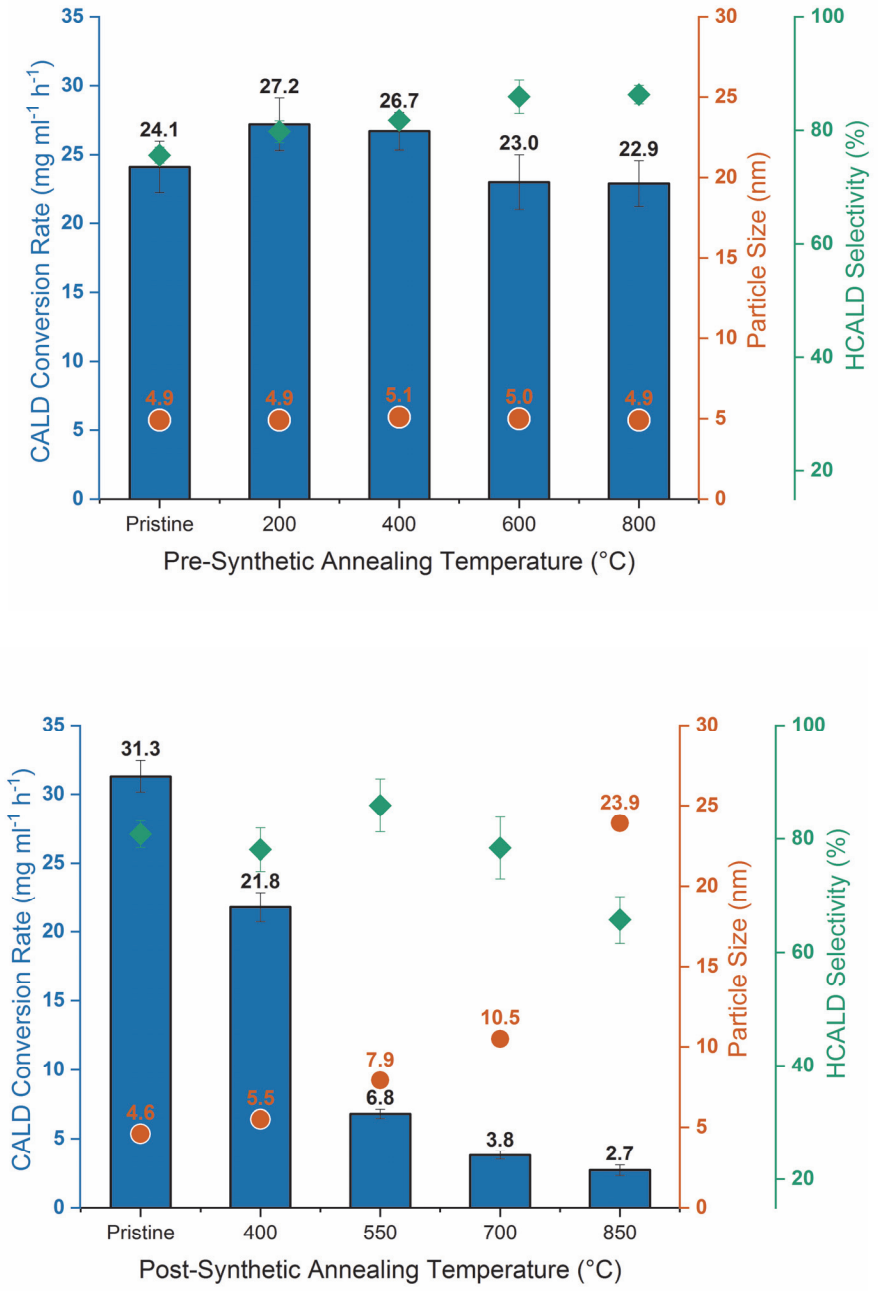


**Figure 3.** CALD conversion rates and selectivity with Pd particle size obtained from hydrogen chemisorption

### 4.2.5 Spatial Distribution of the $Pd^{\delta+}$ Phase and Intrinsic Rate of Charge-depleted Pd

The results obtained thus far prove that strong correlations exist between the EMSI effects, catalyst selectivity, reaction rate. Overall, the TOF decreases with the total perimeter and surface area as depicted in Figure 4. However, as the correlation between the perimeter and TOF dominates that over the surface area, the reaction is expected to predominantly occur at the interface of Pd and carbon. Resasco, Haller, and Omotoso et al have reported similar conclusions in the past for $Rh/TiO_2$ catalysts.[38-39] Differences in activity for various types of atoms (edge, face, defect) in Pd, Pt, and Rh nanoparticles have also been reported for other hydrogenation and dehyrogenation reactions.[40-41] However, in these studies, the influence of geometric and electronic effects on the catalytic activity have been observed for metal particles smaller than 3 nm in diameter. It is commonly considered that particles in excess of 5 nm demonstrate bulk like behavior and the geometric effects do not play for them since the ratio of defect to face atoms does not change drastically after this. Despite this, our results demonstrate that the activity is affected by the particle size and specifically the atoms at the perimeter for particles larger than 5 nm.

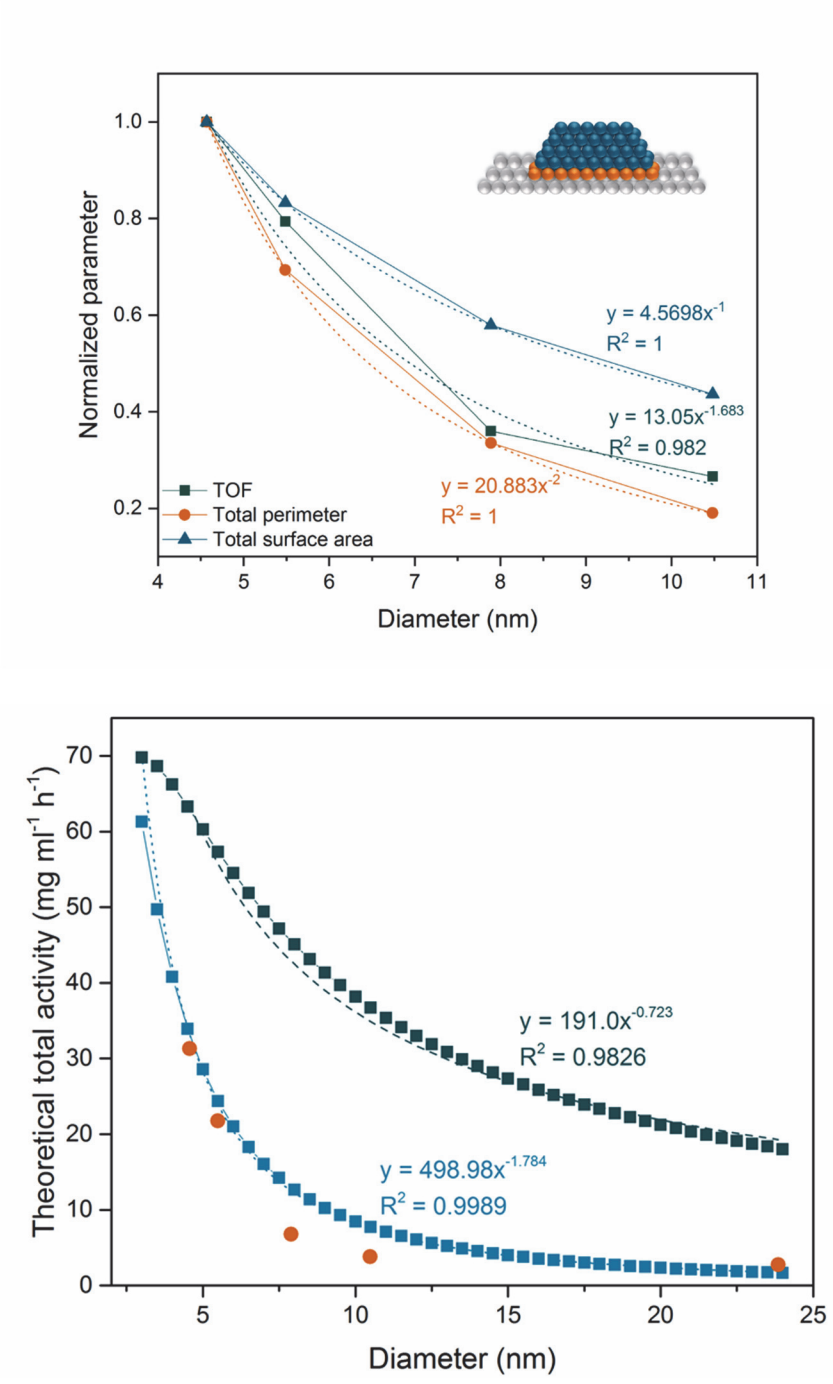


**Figure 4.** Turnover frequencies, total perimeter, and total surface area plotted against the diameter for the PdPS catalysts from no annealing to annealed at 700°C. The data are normalized to the highest value of each type of parameter.

In order to understand the variations in catalytic activity with Pd nanoparticles larger than 5 nm and their predominant dependence on the atoms at the interface, a model representing our catalytic system was developed. Firstly, the $Pd^0/Pd^{\delta+}$ ratio obtained from XPS was analyzed for defining the basic parameters of the model system. Using this experimental data, the height (x) as depicted in Figure S3, which represents the part of the nanoparticle near the interface that is affected by the charge transfer, was estimated. For Pd nanoparticles supported on the PS SCCNTs in the range of 5 to 8 nm, the value of x was observed to be approximately 0.25. Using this x value, the Pd surface area that will be affected by the $Pd^0$ and $Pd^{\delta+}$ phase was estimated and then multiplied by an intrinsic reaction rate of 2 and 600 moles $m^{-2}$ $h^{-1}$ for the two phases, respectively. The total activity was calculated and plotted against the particle diameter to represent our model system (Figure 3). Consequently, the observed reaction rate was also plotted with the diameter as obtained from experimental CALD hydrogenation data and hydrogen chemisorption (Figure 4). The plots obtained from the model system and the experimental data depict similar trends, suggesting that the intrinsic rates at the interfacial atoms and surface atoms in the Pd/C catalysts could indeed be different.

### 4.2.6 Theoretical Insights into the Reactions at the Pd-C Interface

EMSI effects are typically thought to be minimal for C-supported particles, particularly for large particles. Here, we use DFT calculations to examine reactions on $Pd_{119}$ and $Pd_{293}$ hemispherical cubo-octahedral particles supported on functionalized graphene supports (details in Methods). Specifically, we examine the H*-addition to 2-butenal, a model $\alpha,\beta$-unsaturated compound that is analogous to cinnamaldehyde without the phenyl

group; this simpler model compound allows for a closer assessment of the effects of support and location on its hydrogenation without steric influences of the phenyl group. Prior work indicated that metal atoms covalently bound to the C-support have significantly higher partial charge (~0.15 $e^-$) but that support effects are rapidly screened by the metal particle, such that metal atoms one-layer removed were slightly negatively charged, on average (−0.04 $e^-$) with continued decreases in absolute charge with increasing distance between the C-support and the metal atoms, as expected.[21]

Metal surfaces are often treated as a series of non-interacting identical sites by Langmuirian models, in direct contrast to the well-described effects of particle size and shape on turnover rates [R]. These impacts of particle morphology are typically described as altering a distribution of metal atoms in low-index terraces, undercoordinated edge and corner sites, and present in step-edge defect sites.[42-44] High coverages of spectating or reactive species, furthermore, also influence the nature of active sites and these co-adsorbate interactions can also influence reaction rates beyond the site-blocking effects captured by Langmuirian surface models. Recently, non-ideal Langmuir-Hinshelwood kinetic models were used to describe CO-$H_2$ reaction rates on Ru catalysts whose surfaces are essentially saturated in CO* at all practical CO pressures.[45] That work described low-coverage (non-interacting coverages of CO*) as 'ideal' in the context of surface reactions and deviations from that ideality were described with activity coefficients to capture observed deviations from Langmuirian behavior. Finally, surface-support interactivity has been previously described for CO* oxidation and other reactions [R] in which reactants convert directly at metal-support interfaces, often transferring from the support to the metal.[46-48] Here, we will describe heterogeneity among metal surface sites by demonstrating that metal atoms in low-

index planes are directly affected by their proximity to the underlying support—even for reactions that do not directly react with or bind to support atoms.

Figure 5 shows the average binding energies of CH*, O*, and H* adsorbates and how that average binding energy varies on a $Pd_{119}$ cluster. These adsorbates were bound to sites with distinct surface indices (111 or 100), undercoordinated corner/edge atoms, and proximity to the underlying support (modeled as graphene sheets and graphene functionalized by O* and OH* groups, as described in the methods). These three adsorbates (CH*, O*, and H*) were chosen because they are small adsorbates that bind consistently to hollow sites (three-fold and four-fold) on 111 and 100 surfaces and they describe how many hydrocarbons and oxygenates interact with metal surfaces via scaling relationships. The average binding energy for these three species on the 100 surface was −421 kJ $mol^{-1}$, slightly lower that on the 111 surface (−414 kJ $mol^{-1}$). On 111 surfaces, species were bound more weakly to 'hcp' three-fold sites (−418 kJ $mol^{-1}$), which have a metal atom directly beneath them in the subsurface, than to 'fcc' three-fold sites (−410 kJ $mol^{-1}$). CH*, OH*, and H* adsorbed more weakly to Pd particles on functionalized graphene (−410 kJ $mol^{-1}$) than to Pd particles on pristine graphene (−423 kJ $mol^{-1}$) across the same ensemble of binding sites, indicating that the electron withdrawing effects of the support rendered Pd atoms more chemically inert. This is also seen be average binding energies across the surface of the two particles (Figure 5), which show that binding energies at interfacial sites are significantly weaker (less exothermic) than binding energies to the top surface. Sites are not only influenced by the coordination number or interfacial properties of their metal atoms; the average binding energy to an fcc three-fold site on the top of the particle is −425 and −419 kJ $mol^{-1}$ for Pd on pristine and functionalized graphene, respectively, whereas an equivalent fcc

three-fold site on the side of the particle binds CH*, OH*, and H* with an average energy of −436 and −429 kJ mol$^{-1}$, respectively. These increases in binding strength of ~10 kJ mol$^{-1}$ can only be caused by the proximity to the underlying support and not because of direct changes in the coordination numbers of the metal atoms or whether those metal atoms were covalently bound to the support. These data (Figure 5) show the heterogeneity of a relatively small metal particle whose sites often involve undercoordinated metal atoms.

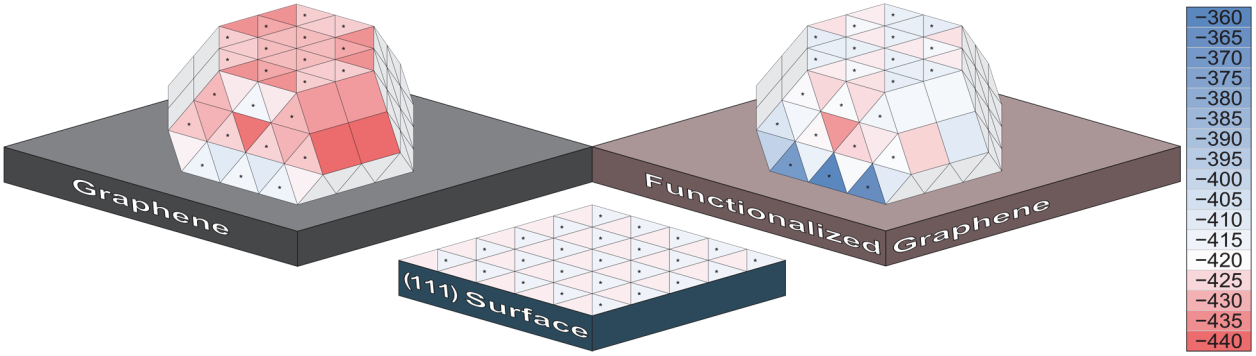


**Figure 5.** Average binding energy (kJ mol$^{-1}$) for CH*, OH*, and H* on a Pd(111) surface and $Pd_{119}$ clusters on pristine and functionalized graphene supports. Dots indicate hcp three-fold sites. Gray squares indicate unexamined binding sites.

Next, we examined a $Pd_{293}$ cluster (Figure 6) which has larger terraces and thus contains more sites, which lack the corner/edge atoms which conflate the effects of the underlying support on metal reactivity. These calculations are still in progress, but they will involve the clusters pictured below only we will only look at the sites, which do not have undercoordinated metal atoms (shown in green in Figure 6).

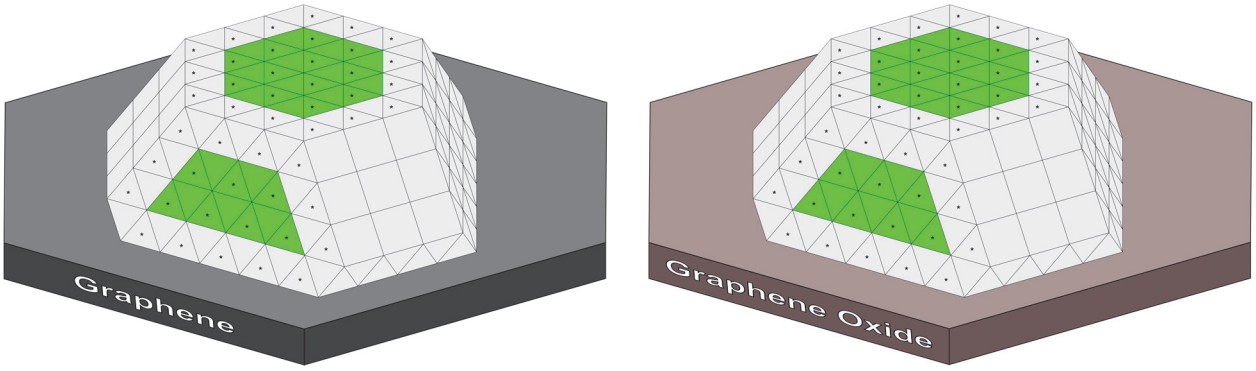


**Figure 6.** $Pd_{293}$ clusters used to get more insights into the change in binding energy with particle size. These calculations are still in progress.

Cinnamaldehyde hydrogenation can form two distinct primary products, an enol and an aldehyde. Here, we model the hydrogenation of a cinnamaldehyde proxy, crotonaldehyde (but-2-enal), which can also form two primary products (butanal and butenol) from hydrogenation. Reactivity trends observed for cinnamaldehyde hydrogenation on Pd/C catalysts suggest that C=C bonds are selectively hydrogenated at low conversions. Crotonaldehyde hydrogenation was modeled to complete saturation (forming 1-butanol) on Pd(111) surfaces to determine kinetically-relevant steps in the formation of butenal and in the direct formation of 1-butanol. Activation and reaction free energies suggest that butenal is formed via sequential H-addition to the C3 atom (adjacent to the $–CH_3$ group) followed by H-addition to the C2 atom; in which the first H-addition (to C3) is the rate determining step. This reaction was then modeled on top of the $Pd_{119}$ cluster and on the side of the $Pd_{119}$ cluster (near but not binding to the support or the interfacial Pd atoms of the particle). The average intrinsic activation barrier for H-addition to crotonaldehyde was 71 kJ $mol^{-1}$ when the reaction was modeled on four distinct sites on top of the $Pd_{119}$ particle (ranging from 68 to 74 kJ $mol^{-1}$); however, when this same reaction was modeled at seven distinc sites on the sides of the same $Pd_{119}$ particle on functionalized graphene, the average intrinsic barrier was 63 kJ

$mol^{-1}$ (with values ranging from 56 kJ $mol^{-1}$ to 71 kJ $mol^{-1}$). This decrease in the activation barrier by 8 kJ $mol^{-1}$ for reactions occurring near the interface is consistent with increased reactivity of those sites as inferred from kinetic data in previous sections. The transition states used to calculate these barriers do not involve edge/corner atoms and thus these shifts only represent the impacts of proximity to the underlying carbon support.

The heterogeneity of a metal surface is therefore caused by the distinct crystal facets (e.g. 111 vs 100), the metal-atom coordination of the binding ensemble, and the proximity to the underlying support. These proximity effects are demonstrated here for large metal particles (>100 clusters) on a non-covalent and covalently interacting carbon supports. The support can shift binding energies of small model adsorbates (CH*, OH*, and H*) as well as alter activation barriers for key reactions, and thus may directly influence rates without directly binding to or interacting with reacting species. These electronic effects may be screened for many sites on large metal particles, but sites near the interface will be influenced by carbon supports for any particle size, even if those sites are not directly at the interface.

### 4.2.7 Elucidation of the Driving Forces Behind the Charge Redistribution at the Pd-C Interface

We subsequently investigated the origin of these electronic effects using ultra-violet photoelectron spectroscopy (UPS).[49] The analysis of the collected spectra revealed that the work function (WF) of the SCCNT support was significantly shifted compared to pristine graphite (WF = 4.0 eV) and was a function of the concentration of surface oxygen-containing functional groups. The shift was the largest for PS SCCNTs after oxidation with nitric acid (WF = 5.0 eV) and the WF decreased to 4.5 eV quasi linearly with the annealing temperature,

hence the C/O ratio at the surface (Table S2), in agreement with recent studies on the optoelectronic properties of reduced graphene oxide. Therefore, our results suggest that the $Pd^{\delta+}$ phase observed by XPS arises from the difference in position of the Fermi levels of the functionalized carbon supports (WF = 4.5-5.0 eV) and the palladium nanoparticles (WF ca. 5.3 eV).

**4.3 Discussion**

We have previously demonstrated that carbons are not inert supports but, instead, that they can substantially alter the activity of a metal active phase decorating their surface. In contrast to the ligand-like effects reported for single-atom catalysts, these MSI are significantly more complex in the case of metal nanoparticles as they remain strong at low oxygen coverage, when the number of metal atoms at the interface outnumbers the potential ligands. We have also demonstrated that these effects as strong enough to shift the binding energy of Pd's core electrons by 0.85 eV. As this shift is of the same order of magnitude than a change in oxidation state and as Pd may reoxidize when handing the sample in air prior to XPS analysis, it was important to repeat the calcination-reduction process in situ. The NAP-XPS experiments performed in the first part of this study now provide direct evidence that the Pd nitrate precursor decomposes at low temperature to form PdO in oxygen, and is further reduced to metallic Pd in hydrogen. As expected from temperature programmed reduction studies reported by others, this reduction takes place at ~80 °C for 5 nm Pd nanoparticles. However, in contrast to Pd on oxide supports, a substantial fraction of the Pd atoms remain in a $Pd^{\delta+}$ state, even after reduction at 400 °C in hydrogen. Analysis of the O1s and C1s spectra revealed that Pd oxides and Pd carbides can be excluded under these

conditions. In addition, this $Pd^{\delta+}$ phase was also detected during depth profiling in vacuum, *i.e.* conditions under which Pd hydrides are unstable. Depth profiling also revealed that in contrast to core-shell structures for which significant changes in composition are detected depending on the analysis depth, the $Pd^{\delta+}/Pd^0$ ratio varied only slightly from 0.44 to 0.5. This result is consistent with a $Pd^{\delta+}$ phase present only at the interface with the carbon support.

As the samples were annealed and the Pd particle size increased, we observed a progressive decrease in $Pd^{\delta+}/Pd^0$ consistent with a larger number of Pd atoms present in the bulk of the metal nanoparticle. This change in composition altered the rate of the reaction. However, the decrease in rate was inconsistent with simple geometric effects as the turnover frequency dropped with particle size. This observation suggested that the intrinsic rate of the Pd atoms depend on their position in the metal particle and that $Pd^{\delta+}$ atoms near the interface may be significantly more active than $Pd^0$ atoms. To further test this hypothesis, we developed a simple mathematic model to predict the evolution of the reaction with particle size. When Pd atoms all show the same intrinsic rate, the overall activity decreases with an inverse $1^{st}$ order trend inconsistent with the experimental data. Using the $Pd^{\delta+}/Pd^0$ ratio provided by XPS, we then attributed different intrinsic rates to the two phases to change their weighted contributions to the overall reactivity. We found that to fit the experimental data, Pd atoms near the interface must show an intrinsic rate about two orders of magnitude higher than bulk $Pd^0$ atoms. This intrinsic rate is consistent with the DFT calculations as the energy barrier for butenal hydrogenation to butanal is about 10 kJ $mol^{-1}$ lower for Pd atoms near the interface that in Pd atoms (111) terraces further away. These results also explain the increase in selectivity observed for supports annealed prior to Pd deposition. As the $Pd^{\delta+}$ contribution

increases with the annealing temperature for this sample series, the formation of HCALD is kinetically favored over PP due to the lower energy barrier for Pd atoms near the interface.

Finally, we confirmed the presence of EMSI using UPS. This technique allows a direct measure of the work function of the supports and catalysts, hereby providing direct evidence for changes in the electronic structure of the support and its effect on the active phase. Although UPS characterizes an integral change in support properties (not just the Pd-C interface), the linear correlation observed between WF, $Pd^{\delta+}$ contribution, and selectivity was intriguing.

In summary, we demonstrated the existence of EMSI effects for Pd/C that can be modulated through simple thermal treatments. These effects are strong enough to change the electronic structure of Pd atoms near the interface and, consequently, their adsorption properties and catalytic activity.

## 4.4 Methods

### 4.4.1 Catalyst Synthesis

Commercial stacked cup carbon nanotube (SCCNT) supports were purchased from Pyrograf Products Inc. (Ohio, USA). The SCCNTs were synthesized by chemical vapor deposition (CVD) and annealed at 700 post synthesis to give the pyrolytically stripped (PS) supports. This annealing process removes the polyaromatic hydrocarbons from the fiber surface without altering the morphology and textural properties of the nanotubes.[25] Prior to use, the obtained supports were treated with trace metal grade concentrated nitric acid (65% $HNO_3$, Fisher scientific) at 100 °C for 4 h in order to remove any impurities and to functionalize the carbon surface. The nitric acid to SCCNT ratio was set to 500 ml for 10 g of

carbon for consistency with previous works.[25, 50-51] Following this treatment, the oxidized SCCNTs were rinsed with 5 L of deionized water (18 MΩ, Millipore) and dried overnight at 110 °C.

Palladium was deposited onto the oxidized SCCNTs by incipient wetness impregnation. Palladium nitrate dihydrate (~40% Pd, Sigma-Aldrich) was chosen as the metal precursor due to its ease of decomposition and absence of impurities in the catalyst post synthesis. 187.5 mg of the palladium precursor was dissolved in 12.6 ml deionized water adjusted to pH 4.0 using nitric acid. The precursor solution was added dropwise to 1.5 g of oxidized supports and the mixture was then sonicated for 5 min in order for the solution to homogeneously wet the carbon surface. The impregnated supports were then dried at room temperature for 8 h, at 65 °C overnight, and at 80 °C for an additional 8 h. The impregnated samples were subsequently transferred to a quartz reactor placed in the center of a tube furnace for calcination and reduction. The dried samples were first calcined in flowing synthetic air (200 ml $min^{-1}$; Airgas) at 250 °C for 2 h using a 2 °C $min^{-1}$ ramp to decompose the metal precursor. After returning to room temperature, the gas atmosphere was switched to nitrogen (200 ml $min^{-1}$; Airgas) for 30 minutes and then to hydrogen (200 ml $min^{-1}$; Airgas) and the samples were reduced at 400 °C for 2 h using a 2 °C $min^{-1}$ ramp. Post reduction, the reactor was kept at 400 °C, flushed with nitrogen for 30 min, and the samples were further annealed under nitrogen at 400, 550, 700, 850, or 1000 °C using a 10 °C/min ramp and a dwell time of 30 min. The samples thus obtained were labeled as PdPS Annealed-T, where PS represents the type of SCCNT support and T represents the annealing temperature.

### 4.4.2 Catalyst Characterization

The actual palladium content of each catalyst was measured by inductively coupled plasma-optical electron spectroscopy (ICP-OES, Perkin Elmer Optima 8000) and used to normalize the reaction rates. Prior to the analysis, the carbon supports of each sample were burned off by heating 30 mg of catalyst in air at 1000 °C for 6 h. The remnant materials were soaked overnight in 5 ml aqua regia to dissolve the palladium metal. The solution was then diluted with 45 ml deionized water and analyzed. Each catalyst was analyzed in quadruplicates.

The catalyst morphology and metal dispersion were imaged using a FEI Quanta 250 scanning electron microscope (SEM) operated at 10 kV. The catalyst samples were placed in aluminum cups and maintained with a solution of sticking tape soaked in hexane. The aluminum cups were mounted on carbon stubs and the samples were imaged using both the secondary and back-scattered electron detectors (for enhanced Z-contrast).

Surface adsorption properties and palladium particle size were probed by hydrogen chemisorption using a static volumetric system attached to a Micromeritics ASAP 2020C instrument. 70 to 80 mg of catalyst was packed in a U-shaped chemisorption tube using quartz wool and re-reduced in situ under hydrogen at 350 °C to remove any palladium surface oxides. The tube was then evacuated, cooled down, and hydrogen was progressively reintroduced to record the adsorption isotherm under isothermal conditions (35 °C). Following this step, a vacuum was applied to remove the weakly bound hydrogen and a second adsorption isotherm was conducted. The adsorptions in the first and second isotherms represent the total ($H_{tot}$) and reversibly ($H_{rev}$) bound hydrogen, respectively. The size of the

Pd nanoparticles was obtained from $H_{tot}$ and the adsorption properties of the catalysts were compared using the $H_{rev}/(H_{tot}-H_{rev})$ ratio.

The average palladium particle size and particle size distribution were also measured for each sample using aberration corrected transmission electron microscopy (TEM). The samples were dispersed in ethanol on a holey carbon coated TEM grid and analyzed at 300 kV using a FEI Titan 80 – 300 equipped with a Gatan US1000 CCD camera.

X-ray diffraction (XRD) analysis was conducted to estimate the Pd crystallite size and characterize any phase change with increasing annealing temperature. A Siemens D-500 instrument with a copper X-ray tube, diffraction beam monochromator, a scintillation detector, a gold holder, and a medium resolution slit was used for the analysis. Two-theta values from 15 to 75 ° were scanned with a step size of 0.05 ° and a dwell time of 3 s per step. The data analysis and crystallite size estimation was conducted using the Jade software and the Scherrer equation.

X-ray photoelectron spectroscopy (XPS) studies were performed using a PHI ESCA 5500 instrument. The samples were irradiated with 225 W monochromated Al Kα X-rays and the pass energy was set at 188 eV for survey scans, 47 eV for high resolution scans, and 59 eV for valence band scans.

The in-situ XPS experiments were performed at the ISSIS beamline of the FHI located at the BESSY II synchrotron facility in Berlin. The high pressure setup consists mainly of a reaction cell attached to a set of differentially pumped electrostatic lenses and a differential- pumped analyzer (Phoibos 150 Plus, SPECS GmbH), as described elsewhere.[52] The spectra were collected in normal emission in vacuum with a probe size of ~ 150μm x 80μm.

The samples were heated from the back to 180°C using an external IR-laser (cw, 808 nm) to compensate for charging. The temperature was controlled via a K-type thermocouple in direct contact with the sample surface.

Gases were introduced in the reaction cell using calibrated mass flow controllers (Bronkhorst). The gas flows and the products released in the gas phase were simultaneously monitored by a differentially pumped quadrupole mass spectrometer (Pfeiffer) connected via a leak valve to the experimental cell.

Sample contamination was checked by survey spectra at the beginning of each experiment. The photo electron spectra were taken at photon energies of 480, 680 and 780 eV (Pd3d) as well as 680 eV (O1s) and 425 eV (C 1s), respectively, with a spectral resolution of 0.3 eV. The low electron kinetic energies of the Pd3d, O1s and C1s regions correspond to an electron mean free path of ≈ 8 Å while the higher electron kinetic energies of the Pd3d region corresponds to ≈ 10 Å. The total XPS information depth is ≈ 2 nm, that is, 95% of all detected electrons originate from 3λ.[53] For XPS analysis, the photoelectron binding energy (BE) is referenced to the Fermi edge, and the spectra are normalized to the incident photon flux. Background correction was performed by using a Shirley background.[54] The spectra were fitted following the Levenberg-Marquardt algorithm to minimize the $\chi^2$. Peak shapes were modeled by using asymmetric Doniach-Sunjic functions convoluted with Gaussian profiles.[55] The accuracy of the fitted peak positions is ≈ 0.05 eV.

Ultraviolet photoelectron spectroscopy (UPS) and work function measurements were performed on a Specs Phoibos NAP-150 hemispherical analyzer with a monochromated Al K-alpha source and a non-monochromated He I-alpha ultraviolet source. During the UPS and WF measurements, the sample was held at a bias voltage of -20 V relative to the

spectrometer to accelerate the slow secondary electrons. The sample geometry was with the sample normal parallel to the electrostatic lens axis of the analyzer. Samples were measured at temperatures of 100 °C to 450 °C in 50 °C increments. The position of the work function was determined from the secondary electron cut-off, by fitting a line tangent to the data at point of steepest descent, and extrapolating the line to the intersection with the abscissa. The binding energy of this intersection represents the secondary electron cut-off. A value of 20 eV was added to this binding energy to account for the applied voltage, and the resulting number was subtracted from the photon energy to yield the work function.

### 4.4.3 Catalytic Investigations

The catalysts in this study were tested for the ambient pressure liquid phase hydrogenation of cinnamaldehyde. Reactions were performed in a 3-neck round bottom flask connected to a condenser maintained at 4 °C. Firstly, 100 mg of the catalyst was added to the batch reactor with 40 ml dioxane (99.8% purity, Sigma-Aldrich) and 365 mg decane (internal standard; ≥ 99% purity, Sigma-Aldrich) along with a stir bar. The reactor was placed in an oil bath at room temperature and the solution was stirred at 500 rpm. The system was then purged with nitrogen at 20 ml $min^{-1}$ for 20 min using a Bronkhorst mass flow controller and a fine frit (10 – 20 μm porosity) to remove any air. Following this, the gas flow was switched to hydrogen and the temperature of the oil bath was ramped to 80 °C using an IKA-RCT magnetic stir plate equipped with a PT1000 thermocouple. After 30 minutes at 80 °C, 5 g of cinnamaldehyde dissolved in 10 ml of dioxane was added to the reactor with a syringe using the third neck of the flask fitted with a rubber septum. The addition of cinnamaldehyde marked the starting time of the reaction and 200 μl of samples were then withdrawn every 15

minutes. The reaction samples were collected in pre-cooled glass vials and refrigerated to immediately quench the reaction and prevent the evaporation of the solvent. All catalytic tests were performed in triplicates.

Reactant and products were analyzed using an Agilent 7890 A gas chromatograph (GC) with an HP-5 column (30 m X 320 μm X 0.25 μm) and a flame ionization detector (FID). Prior to the analysis, samples were diluted 15 times with dioxane, filtered using 0.22 μm nylon filters, and 1 μl of this diluted sample was injected in the GC. A split ratio of 20:1 at 20 ml $min^{-1}$, inlet heater temperature of 300 °C, total flow of 24 ml $min^{-1}$, septum purge flow of 3 ml $min^{-1}$, and column flow of 1 ml $min^{-1}$ was used. The initial temperature of the oven was maintained at 40 °C for 1 min and then increased to 180 °C with a ramp rate of 10 °C $min^{-1}$. The temperature of the FID heater was maintained at 300 °C.

### 4.4.4 Density Functional Theory Calculations

Plane-wave density functional theory calculations were performed using the Vienna ab initio simulation package (VASP)[56] to calculate the interaction energies between Pd particles and the carbon supports, as well as the reaction coordinates for cinnamaldehyde hydrogenation. In order to fully capture the electronic phenomena occurring at the metal-carbon interface and their attenuation with distance from the support, the calculations were performed for Pd clusters of 119 and 293 atoms, which corresponds to nanoparticles of 1.7 and 2.5 nm in diameter, respectively and 0.9 and 1.1 nm in height, respectively. The particles were modeled as cubo-octahedral particles which are composed of (100) and (111) surfaces, with atoms arranged in 4–5 metal layers orthogonal to the carbon surface. The support was modeled as either a graphene sheet or a functionalized graphene sheet (which has 0.125 ML

of O* and 0.125 ML of OH* adsorbed). The lattice parameters for the functionalized graphene sheet were 8.702 and 2.512; those for an equivalent pure graphene sheet were 8.523 and 2.46, indicating that functionalization of the graphene sheet is associated with an expansion in C–C bonds. The functionalized graphene sheet, furthermore, is curved in a periodic manner, further increasing C–C bond lengths in a manner consistent with the rehybridization of C-atoms from $sp^2$ to $sp^3$.

Plane-waves were constructed using an energy cutoff of 400 eV with projector augmented wave potentials[57]. The revised Perdew–Burke–Ernzerhof (RPBE) form of the generalized gradient approximation (GGA) was used to determine exchange and correlation energies[58-59]. Wavefunctions were converged to within $10^{-6}$ eV and forces were computed using a fast Fourier transform (FFT) grid with a cutoff of twice the planewave cutoff. A 1 × 1 × 1 Γ-point sampling of the first Brillouin zone (k-point mesh) was used and structures were relaxed until forces on unconstrained atoms were <0.05 eV $Å^{-1}$. Converged wavefunctions were transformed into a set of localized quasiatomic orbitals (QUAMBOs)[60] and used to carry out Löwdin population analyses[61] to determine the charges on the individual atoms.

## 4.5 References


1. Willinger, M. G.; Zhang, W.; Bondarchuk, O.; Shaikhutdinov, S.; Freund, H. J.; Schlögl, R. *Angew. Chem. Int. Ed.* **2014,** *53*, 5998-6001.

2. Jenness, G. R.; Schmidt, J. *ACS Catal.* **2013,** *3*, 2881-2890.

3. Zhang, L.; Liu, H.; Huang, X.; Sun, X.; Jiang, Z.; Schlögl, R.; Su, D. *Angew. Chem. Int. Ed.* **2015,** *54*, 15823-15826.

4. Matsubu, J. C.; Zhang, S.; DeRita, L.; Marinkovic, N. S.; Chen, J. G.; Graham, G. W.; Pan, X.; Christopher, P. *Nat. Chem.* **2016,** *9*, 120-127.

5. Schlögl, R. In *Preparation of Solid Catalysts*, Ertl, G., Knözinger, H., Weitkamp, J., Eds.; Wiley-VCH Verlag: Weinheim, 1999.

6. Schlögl, R. In *Handbook of Heterogeneous Catalysis*, Ertl, G., Knözinger, H., Schüth, F., Weitkamp, J., Eds.; Wiley-VCH Verlag: Weinheim, 2007.

7. Auer, E.; Freund, A.; Pietsch, J.; Tacke, T. *Appl. Catal., A* **1998,** *173*, 259-271.

8. Chen, B.; Dingerdissen, U.; Krauter, J. G. E.; Lansink Rotgerink, H. G. J.; Möbus, K.; Ostgard, D. J.; Panster, P.; Riermeier, T. H.; Seebald, S.; Tacke, T.; Trauthwein, H. *Appl. Catal., A* **2005,** *280*, 17-46.

9. Arunajatesan, V.; Chen, B.; Möbus, K.; Ostgard, D. J.; Tacke, T.; Wolf, D. In *Carbon Materials for Catalysis*, Serp, P., Figueiredo, J. L., Eds.; John Wiley & Sons: Hoboken, 2009; pp 535-572.

10. Radovic, L. R.; Rodriguez-Reinoso, F. In *Chemistry and Physics of Carbon*, Thrower, P. A., Ed.; Marcel-Dekker: New-York, 1997; Vol. 25.

11. Bartholomew, C. H.; Farrauto, R. J. *Fundamentals of Industrial Catalytic Processes;* Wiley: Hoboken, NJ, USA, 2005.

12. Besson, M.; Gallezot, P.; Pinel, C. *Chem. Rev.* **2013,** *114*, 1827-1870.

13. Su, D. S.; Perathoner, S.; Centi, G. *Chem. Rev.* **2013,** *113*, 5782-5816.

14. Toebes, M. L.; Prinsloo, F. F.; Bitter, J. H.; van Dillen, A. J.; de Jong, K. P. *J. Catal.* **2003,** *214*, 78-87.

15. Toebes, M. L.; Zhang, Y.; Hájek, J.; Alexander Nijhuis, T.; Bitter, J. H.; Jos van Dillen, A.; Murzin, D. Y.; Koningsberger, D. C.; de Jong, K. P. *J. Catal.* **2004,** *226*, 215-225.

16. Tessonnier, J.-P.; Pesant, L.; Ehret, G.; Ledoux, M. J.; Pham-Huu, C. *Appl. Catal., A* **2005,** *288*, 203-210.

17. Amadou, J.; Chizari, K.; Houllé, M.; Janowska, I.; Ersen, O.; Bégin, D.; Pham-Huu, C. *Catal. Today* **2008,** *138*, 62-68.

18. Plomp, A. J.; Vuori, H.; Krause, A. O. I.; de Jong, K. P.; Bitter, J. H. *Appl. Catal., A* **2008,** *351*, 9-15.

19. Zhu, J.; Holmen, A.; Chen, D. *ChemCatChem* **2013,** *5*, 378-401.

20. Centi, G.; Perathoner, S. *ChemSusChem* **2011,** *4*, 913-925.

21. Rao, R. G.; Blume, R.; Hansen, T. W.; Fuentes, E.; Dreyer, K.; Moldovan, S.; Ersen, O.; Hibbitts, D. D.; Chabal, Y. J.; Schlögl, R.; Tessonnier, J.-P. *Nat. Commun.* **2017,** *8*, 340.

22. Yang, Y.; Reber, A. C.; Gilliland, S. E.; Castano, C. E.; Gupton, B. F.; Khanna, S. N. *J. Catal.* **2018,** *360*, 20-26.

23. Şen, F.; Gökağaç, G. *J. Phys. Chem. C* **2007,** *111*, 5715-5720.

24. Dong, B.; Pei, Y.; Zhao, F.; Goh, T. W.; Qi, Z.; Xiao, C.; Chen, K.; Huang, W.; Fang, N. *Nature Catalysis* **2018,** *1*, 135.

25. Tessonnier, J.-P.; Rosenthal, D.; Hansen, T. W.; Hess, C.; Schuster, M. E.; Blume, R.; Girgsdies, F.; Pfänder, N.; Timpe, O.; Su, D. S.; Schlögl, R. *Carbon* **2009,** *47*, 1779-1798.

26. Tessonnier, J.-P.; Rosenthal, D.; Girgsdies, F.; Amadou, J.; Bégin, D.; Pham-Huu, C.; Su, D. S.; Schlögl, R. *Chem. Commun.* **2009**, 7158-7160.

27. Shao, L.; Zhang, B.; Zhang, W.; Hong, S. Y.; Schlögl, R.; Su, D. S. *Angew. Chem. Int. Ed.* **2013,** *52*, 2114-2117.

28. Yuvaraj, S.; Fan-Yuan, L.; Tsong-Huei, C.; Chuin-Tih, Y. *The Journal of Physical Chemistry B* **2003,** *107*, 1044-1047.

29. Tengco, J. M. M.; Lugo-José, Y. K.; Monnier, J. R.; Regalbuto, J. R. *Catal. Today* **2015,** *246*, 9-14.

30. Rameshan, C.; Stadlmayr, W.; Penner, S.; Lorenz, H.; Mayr, L.; Hävecker, M.; Blume, R.; Rocha, T.; Teschner, D.; Knop-Gericke, A.; Schlögl, R.; Zemlyanov, D.; Memmel, N.; Klötzer, B. *J. Catal.* **2012,** *290*, 126-137.

31. Teschner, D.; Pestryakov, A.; Kleimenov, E.; Hävecker, M.; Bluhm, H.; Sauer, H.; Knop-Gericke, A.; Schlögl, R. *J. Catal.* **2005,** *230*, 186-194.

32. Sinha, S.; Badrinarayanan, S.; Sinha, A. *Journal of Physics F: Metal Physics* **1986,** *16*, L229.

33. Wu, B.; Huang, H.; Yang, J.; Zheng, N.; Fu, G. *Angew. Chem.* **2012,** *124*, 3496-3499.

34. Vu, K. B.; Bukhryakov, K. V.; Anjum, D. H.; Rodionov, V. O. *ACS Catal.* **2015,** *5*, 2529-2533.

35. Durndell, L. J.; Parlett, C. M. A.; Hondow, N. S.; Isaacs, M. A.; Wilson, K.; Lee, A. F. *Sci. Rep.* **2015,** *5*, 9425.

36. Jiang, F.; Cai, J.; Liu, B.; Xu, Y.; Liu, X. *RSC Adv.* **2016,** *6*, 75541-75551.

37. Cárdenas-Lizana, F.; Hao, Y.; Crespo-Quesada, M.; Yuranov, I.; Wang, X.; Keane, M. A.; Kiwi-Minsker, L. *ACS Catal.* **2013,** *3*, 1386-1396.

38. Resasco, D.; Haller, G. *J. Catal.* **1983,** *82*, 279-288.

39. Omotoso, T.; Boonyasuwat, S.; Crossley, S. P. *Green Chem.* **2014,** *16*, 645-652.

40. Wilson, O. M.; Knecht, M. R.; Garcia-Martinez, J. C.; Crooks, R. M. *J. Am. Chem. Soc.* **2006,** *128*, 4510-4511.

41. Chen, W.; Ji, J.; Feng, X.; Duan, X.; Qian, G.; Li, P.; Zhou, X.; Chen, D.; Yuan, W. *J. Am. Chem. Soc.* **2014,** *136*, 16736-16739.

42. Hibbitts, D.; Iglesia, E. *Acc. Chem. Res.* **2015,** *48*, 1254-1262.

43. Allian, A. D.; Takanabe, K.; Fujdala, K. L.; Hao, X.; Truex, T. J.; Cai, J.; Buda, C.; Neurock, M.; Iglesia, E. *J. Am. Chem. Soc.* **2011,** *133*, 4498-4517.

44. Den Breejen, J.; Radstake, P.; Bezemer, G.; Bitter, J.; Frøseth, V.; Holmen, A.; Jong, K. d. *J. Am. Chem. Soc.* **2009,** *131*, 7197-7203.

45. Liu, J.; Hibbitts, D.; Iglesia, E. *J. Am. Chem. Soc.* **2017,** *139*, 11789-11802.

46. Green, I. X.; Tang, W.; Neurock, M.; Yates, J. T. *Science* **2011,** *333*, 736-739.

47. Graciani, J.; Mudiyanselage, K.; Xu, F.; Baber, A. E.; Evans, J.; Senanayake, S. D.; Stacchiola, D. J.; Liu, P.; Hrbek, J.; Sanz, J. F. *Science* **2014,** *345*, 546-550.

48. Rodriguez, J. A.; Liu, P.; Stacchiola, D. J.; Senanayake, S. D.; White, M. G.; Chen, J. G. *ACS Catal.* **2015,** *5*, 6696-6706.

49. Yang, S.; Zhou, P.; Chen, L.; Sun, Q.; Wang, P.; Ding, S.; Jiang, A.; Zhang, D. W. *Journal of Materials Chemistry C* **2014,** *2*, 8042-8046.

50. Tessonnier, J.-P.; Ersen, O.; Weinberg, G.; Pham-Huu, C.; Su, D. S.; Schlogl, R. *ACS Nano* **2009,** *3*, 2081-2089.

51. Rao, R. G.; Blume, R.; Hansen, T. W.; Fuentes, E.; Dreyer, K.; Moldovan, S.; Ersen, O.; Hibbitts, D. D.; Chabal, Y. J.; Schlögl, R.; Tessonnier, J.-P. *Nature Communications* **2017,** *8*, 340.

52. Bluhm, H.; Hävecker, M.; Knop-Gericke, A.; Kiskinova, M.; Schloegl, R.; Salmeron, M. *MRS Bull.* **2007,** *32*, 1022-1030.

53. Seah, M. *Surf. Interface Anal.* **1986,** *9*, 85-98.

54. Shirley, D. A. *Phys. Rev. B* **1972,** *5*, 4709.

55. Doniach, S.; Sunjic, M. *J. Phys. Condens. Matter* **1970,** *3*, 285.

56. Kresse, G.; Hafner, J. *Phys. Rev. B* **1993,** *47*, 558.

57. Blöchl, P. E. *Phys. Rev. B* **1994,** *50*, 17953.

58. Perdew, J. P.; Burke, K.; Ernzerhof, M. *Phys. Rev. Lett.* **1996,** *77*, 3865.

59. Hammer, B.; Hansen, L. B.; Nørskov, J. K. *Phys. Rev. B* **1999,** *59*, 7413.

60. Lu, W.; Wang, C.; Schmidt, M.; Bytautas, L.; Ho, K.; Ruedenberg, K. *J. Chem. Phys.* **2004,** *120*, 2629-2637.

61. Löwdin, P. O. *J. Chem. Phys.* **1950,** *18*, 365-375.

## 4.6 Supplementary Information

### 4.6.1 Interfacial metal-support interaction calculations:

#### 4.6.1.1 Experimental values:

The perimeter and surface area for each particle were calculated using equation (1) and (2), respectively.

$$Perimeter\ of\ one\ particle = 2\pi R \tag{1}$$

$$Surface\ area\ of\ one\ particle = 2\pi R^2 \tag{2}$$

where, R is the radius of the particle as obtained from hydrogen chemisorption and particles were assumed to be hemispherical in shape.

In order to obtain the total perimeter and the total surface area of all the nanoparticles in the catalyst, the values calculated for each particle were multiplied by the total number of particles. The number of particles in each catalyst were estimated using equation (3).

$$Number\ of\ particles\ (n) = \frac{Total\ volume\ of Pd}{Volume\ of\ each\ particle} \tag{3}$$

As the total volume of Pd metal on each catalyst is constant due to the uniform loading of Pd, the numerator of the equation (3) can be assumed to be constant. Therefore, n will only be dependent on the denominator of equation (3). This correlation has been better explained in equation (4).

$$Number\ of\ particles\ (n) \propto \frac{1}{\left(\frac{2\pi R^3}{3}\right)} \tag{4}$$

Therefore, the total perimeter of all the particles can be estimated by multiplying equation (1) and (4) to obtain equation (5).

$$Total\ perimeter\ \propto \frac{1}{R^2} \tag{5}$$

Similarly, the total surface area of all the particles can be estimated by multiplying equation (2) and (4) to obtain equation (6).

$$Total\ surface\ area\ \propto \frac{1}{R} \tag{6}$$

The total perimeter and total surface area were normalized using the highest value for estimated for them in each catalyst series.

**4.6.1.2 Model values:**

Theoretical models were designed to estimate the activity of the nanoparticles with different sizes. Using the ratio of $Pd^0$ and $Pd^{\delta+}$ as obtained from X-ray photoelectron spectroscopy studies, the average height (x) at the metal-support interface, which will be affected by the $Pd^{\delta+}$ phase, was calculated to be approximately 0.25 nm. Using this height x, where the $Pd^{\delta+}$ phase will predominantly be present, the area at the surface of the particle that will be affected by this phase was calculated using equation (7). Similarly, the surface area that will be affected by the Pd0 phase was calculated using equation (8).

$$Surface\ area\ affected\ by\ Pd^{\delta+}phase = 2\pi R^2 - 2\pi(R-x)^2 \tag{7}$$

$$Surface\ area\ affected\ by\ Pd^{0}phase = 2\pi(R-x)^2 \tag{8}$$

In Model 1, it was assumed that the intrinsic reaction rate was the same on $Pd^0$ and $Pd^{\delta+}$ sites. Therefore, the surface areas obtained from equation (7) and (8) were multiplied by the same intrinsic reaction rate of 300 mg $ml^{-1}$ $h^{-1}$ to obtain the total theoretical activity.

In Model 2, it was assumed that the intrinsic reaction rate was the different for the $Pd^0$ and $Pd^{\delta+}$ sites. Therefore, the surface areas obtained from equation (7) and (8) were multiplied by intrinsic reaction rates of 600 and 2 mg $ml^{-1}$ $h^{-1}$, respectively, to obtain the total theoretical activity.

### 4.6.2 Supplementary Tables

**Table S1.** Inductively Coupled Plasma-Optical Emission Spectroscopy (ICP-OES) results for the palladium metal loading in catalysts using the PS supports with different annealing temperatures

| Catalyst | Pd metal loading (%)[a] |
|---|---|
| PdPS Pristine | 3.1 ± 0.1 |
| PdPS Annealed-400 | 3.0 ± 0.3 |
| PdPS Annealed-550 | 2.9 ± 0.1 |
| PdPS Annealed-700 | 2.9 ± 0.1 |
| PdPS Annealed-850 | 2.9 ± 0.1 |
| PdPS Annealed-1000 | 3.2 ± 0.3 |

[a] All samples were analysed in triplicates to obtain the standard deviation.

**Table S2.** Support annealing temperature used for pre-treatment, ratio of surface oxygen to carbon as obtained from X-ray photoelectron spectroscopy, and catalyst work function as measured from ultraviolet photoelectron spectroscopy

| Support annealing temperature (°C) | Support O/C ratio | Catalyst work function (eV) |
|---|---|---|
| 0 | 0.24 | 5.1 |
| 200 | 0.23 | 5.0 |
| 400 | 0.23 | 4.85 |
| 600 | 0.11 | 4.73 |

**Table S3.** Average palladium nanoparticle sizes as obtained from hydrogen chemisorption and X-ray diffraction (XRD)

| Catalyst | Hydrogen chemisorption (nm) | XRD (nm) |
|---|---|---|
| PdPS Pristine | 4.57 | 5.1 ± 0.3 |
| PdPS Annealed-400 | 5.49 | 5.5 ± 0.3 |
| PdPS Annealed-550 | 7.89 | 5.5 ± 0.3 |
| PdPS Annealed-700 | 10.48 | 11.3 ± 0.5 |
| PdPS Annealed-850 | 23.86 | 10.6 ± 0.3 |
| PdPS Annealed-1000 | 53.13 | 13.5 ± 0.6 |

**Table S4.** Pd particle size and surface area obtained from 1st adsorption isotherm and the difference (1st adsorption isotherm – 2nd adsorption isotherm) results in hydrogen chemisorption. Theoretical atomic cross section area for Pd used for the calculation was 0.0787 $nm^2$.

| Catalyst | Particle size from 1st isotherm (nm) | Surface area from 1st isotherm ($m^2$/g sample) |
|---|---|---|
| PdPS Pristine | 4.57 | 5.46 |
| PdPS Annealed-400 | 5.49 | 4.55 |
| PdPS Annealed-550 | 7.89 | 3.16 |
| PdPS Annealed-700 | 10.48 | 2.38 |
| PdPS Annealed-850 | 23.86 | 1.05 |
| PdPS Annealed-1000 | 53.13 | 0.47 |

Negative values of the particle sizes and surface area are due to the highly reversible nature of the isotherms

### 4.6.3 Supplementary Figures

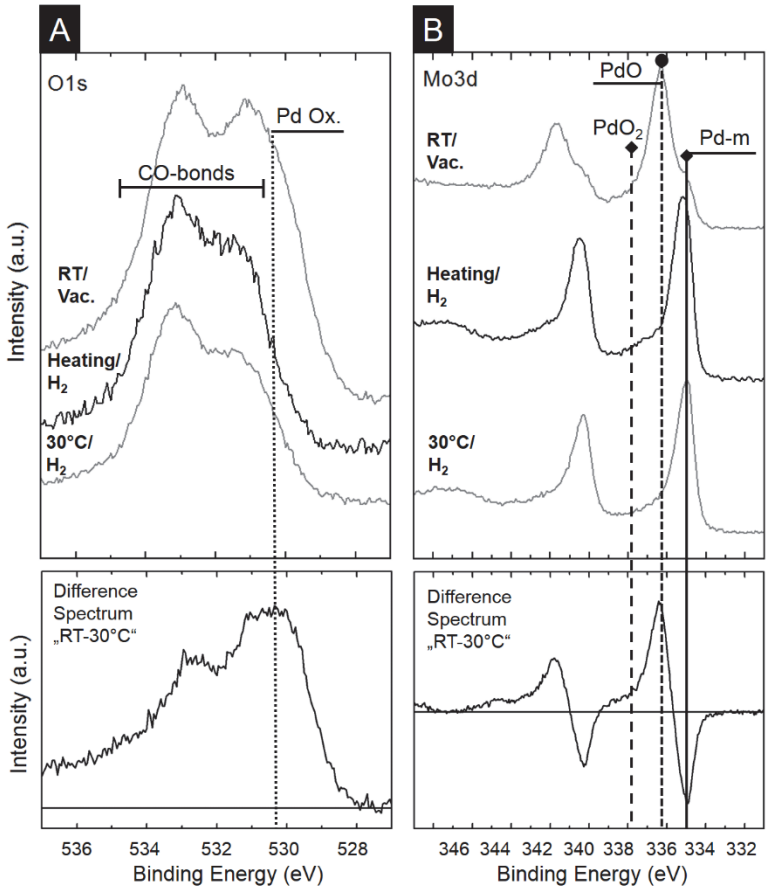


**Figure S1.** In-situ X-ray photoelectron spectra of a) O 1s and b) Pd 3d for Pd/PS catalysts at room temperature under vacuum and at increasing temperature up to 30 °C under hydrogen.

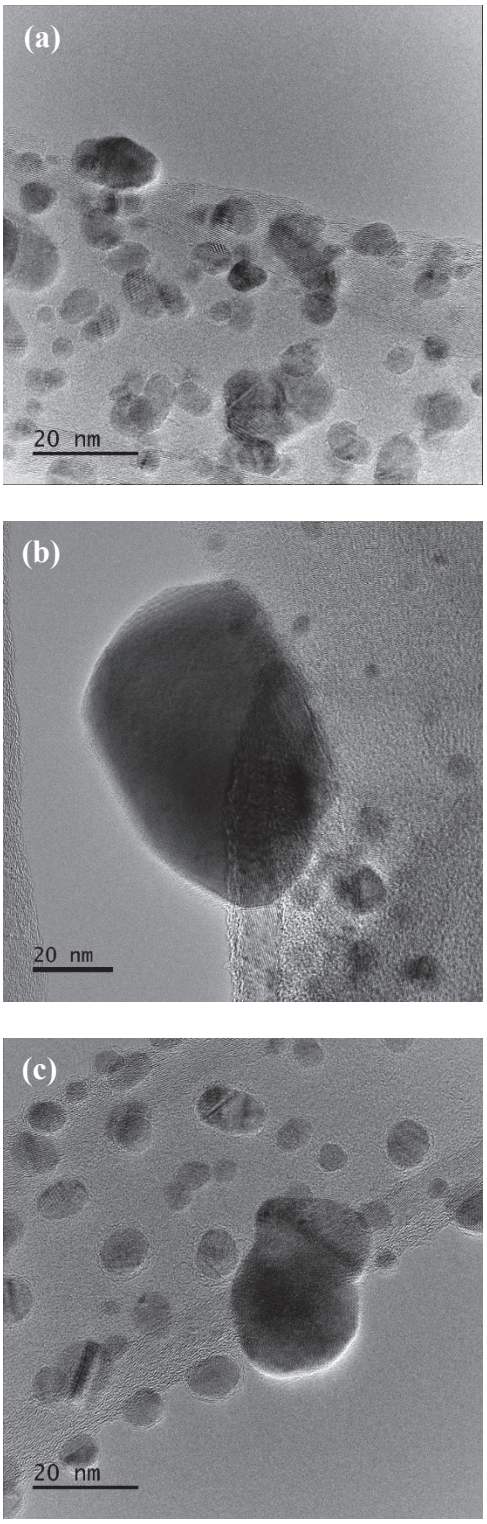


**Figure S2.** Aberration-corrected transmission electron micrographs of a) PdPS No Anneal b) PdPS Anneal700 c) PdPS Anneal850. Micrographs reveal varied thickness of the carbon overlayer on the Pd nanoparticles.

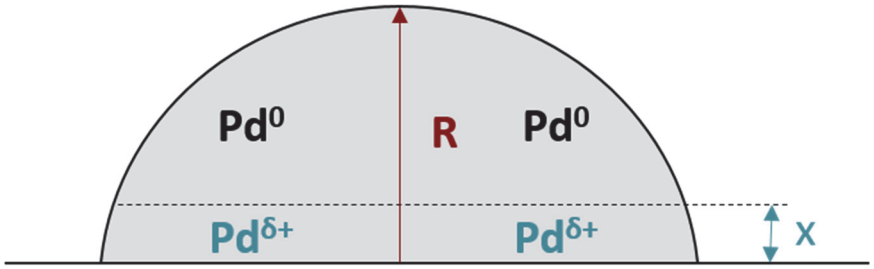


**Figure S3.** Scanning electron microscopy (SEM) images of Pd/PS catalysts annealed at a) 700, b) 850, and c) 1000 °C. The images were acquired in the BSE mode. Scale bar represents 500 nm.

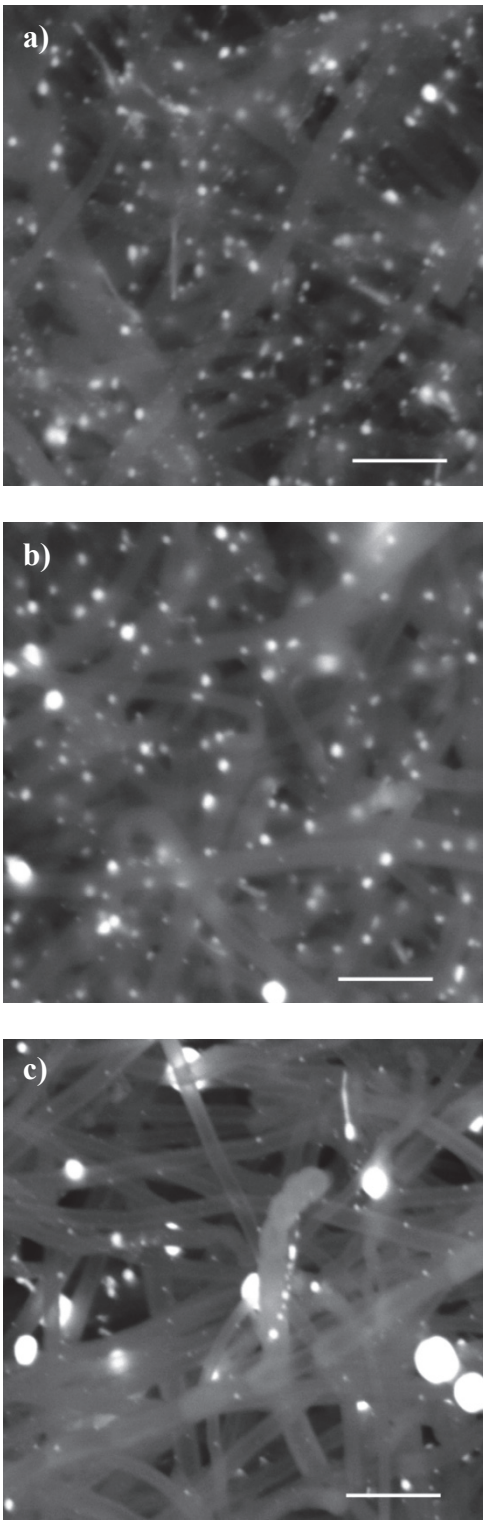


**Figure S4.** Scanning electron microscopy (SEM) images of Pd/PS catalysts annealed at a) 700, b) 850, and c) 1000 °C. The images were acquired in the BSE mode. Scale bar represents 500 nm.

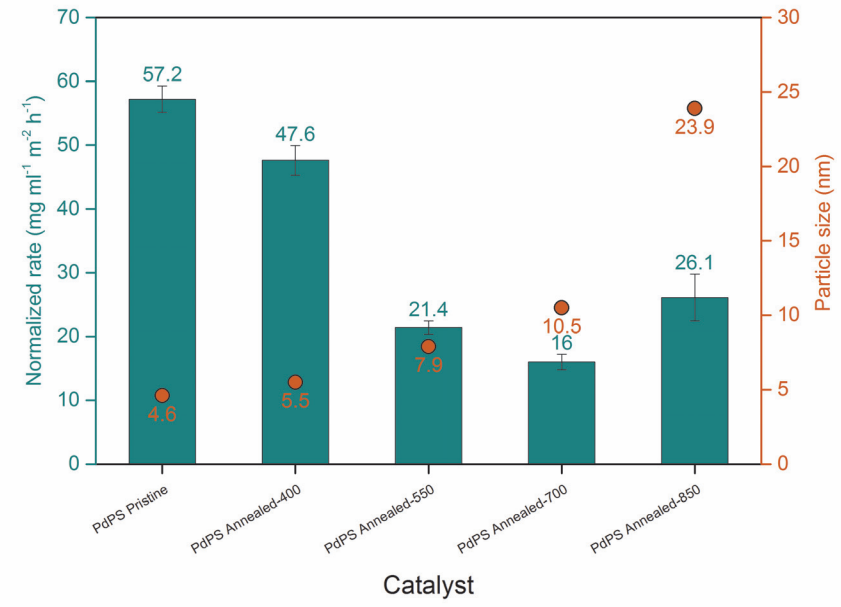


**Figure S5.** Rates for CALD conversion normalized with Pd active metal surface area and the particle sizes obtained from hydrogen chemisorption.

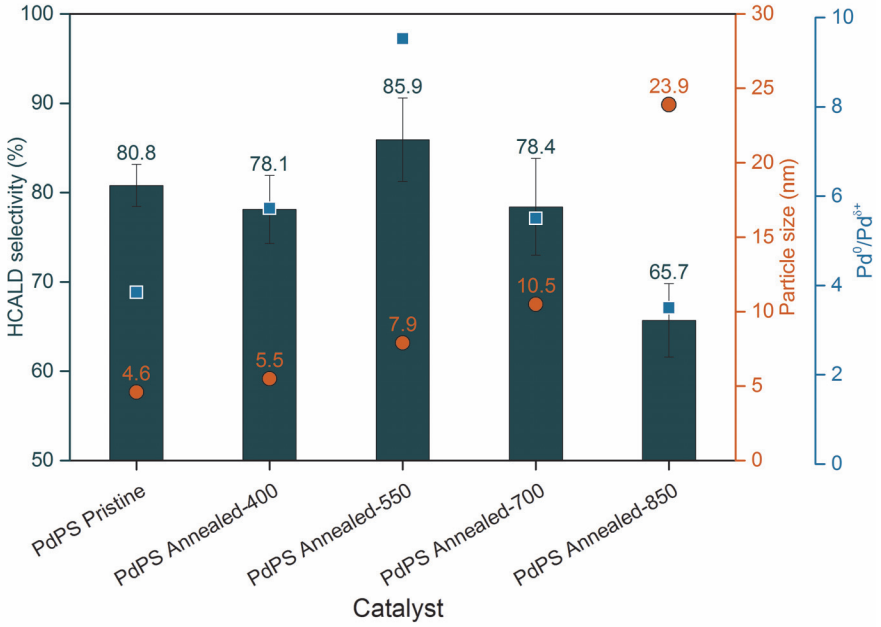


**Figure S6.** HCALD selectivity, particle size from hydrogen chemisorption, and $Pd^0/Pd^{\delta+}$ phase ratio from XPS for the PdPS catalysts

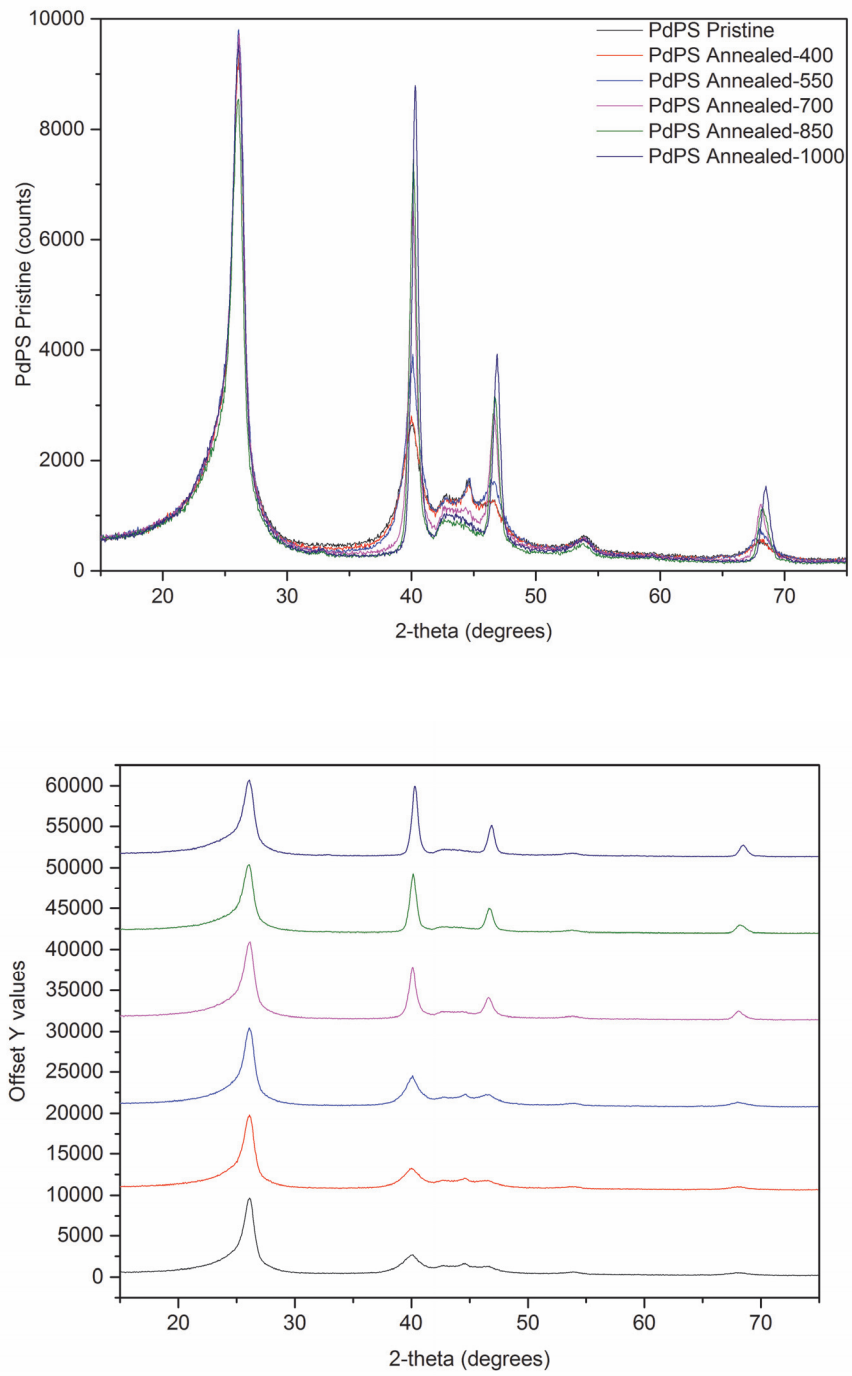


**Figure S7.** X-ray diffractograms for the Pd on PS catalyst supports

# CHAPTER 5

# EFFECT OF METAL-SUPPORT HETEROJUNCTIONS ON THE CATALYTIC ACTIVITY OF PALLADIUM NANOPARTICLES

A manuscript in preparation for Advanced Materials

Radhika G. Rao[1,2], Season Chen[1,3], Mark Greiner[4], & Jean-Philippe Tessonnier[1,2,*]

[1] Department of Chemical and Biological Engineering, Iowa State University, Ames, IA 50011, USA

[2] NSF Engineering Research Center for Biorenewable Chemicals, Ames, IA 50011, USA

[3] Department of Civil and Environmental Engineering, The Hong Kong Polytechnic University, Hung Hom, Kowloon, Hong Kong, China

[4] Max Planck Institute for Chemical Energy Conversion, Heterogeneous Reactions Group, DE-45470 Mülheim an der Ruhr, Germany

[*] Corresponding author

## Abstract

In heterogeneous catalysis, supports not only serve to disperse the active phase and increase the number of active sites available to the reaction, but they can also actively participate in the reaction through activation of the reactants and/or modification of the active sites. Among the various metal-support effects known in catalysis, the electronic metal-support interactions remain the least understood. Here, we demonstrate that these effects can be simply explained in terms of charge transfer at the metal-support heterojunction. The direction and intensity of this charge transfer can be predicted by measuring the work function and, when applicable, the band gap of the support. In the case of carbonaceous materials (carbon nanotubes, carbon nitride), the electronic structure of the support can be

further engineered through simple thermal treatments to tailor the catalytic performance of the active phase, hereby offering a powerful handle to fine tune the catalytic activity of metal nanoparticles.

## 5.1 Introduction

The chemical industry relies heavily on nanostructured heterogeneous catalysts to minimize the formation of undesired byproducts—waste—and decrease the production costs. Industrial catalysts are constantly refined and optimized, a process that typically involves manipulating the electronic structure of the active phase with atomic precision. Various strategies have been explored and developed, for example to control the number of low coordination sites in metal nanoparticles by altering the size and shape of the particles or through alloying. In the 1960s, Schwab also hypothesized that the electronic structure of a metal, hence its catalytic activity, could be modulated by giving or withdrawing electronic density using a semiconducting support. The direction of this charge transfer would then depend on the metal-support heterojunction and the electronic properties intrinsic to the support material and the active phase. This hypothesis nucleated many studies over the past half a century and gave rise to the so-called strong metal support interactions (SMSI). However, advances in environmental transmission electron microscopy (ETEM) demonstrated a few decades later that most SMSI effects are actually due to the migration of species from the support onto the metal active phase under reducing conditions. Still today, there is limited evidence for electronic SMSI effects as defined by Schwab and in most cases evidence was provided for metal nanoparticles supported on well-defined semiconducting oxides.[1-2]

We have recently demonstrated that electronic metal-support interactions are not restricted to oxides but that carbon supports present similar properties when functionalized. Our work built on recent studies discussing the optoelectronic properties of nanocarbons. We showed that when structural defects such as vacancies are introduced in the honeycomb structure of graphitic carbons, carbons atoms located at edges are saturated with oxygen-containing functional groups that act as molecular dipoles. These dipoles alter the electronic structure of the carbon material and, as a result, promote a charge transfer at the metal-carbon interface strong enough to enhance the intrinsic rate of palladium atoms by two orders of magnitude for a model hydrogenation reaction.

Here, we study these electronic effects in more details and demonstrate that they can be explained and predicted by measuring the work function of the carbon support and of the corresponding catalyst. Furthermore, the proposed method can be generalized and applied to other organic (carbon nitride) catalyst supports.

## 5.2 Experimental Methods

### 5.2.1 Catalyst synthesis

Mesoporous g-$C_3N_4$ supports were synthesized using a facile one-pot synthesis method that was recently reported.[3] Melamine (99 %, Sigma-Aldrich) and ammonium chloride (≥99.5 %, Fisher) were grounded by mortar and pestle, and homogeneously mixed in a one-to-one mass ratio (5 g each). The mixture was then transferred to an alumina crucible, covered with a borosilicate watch glass, heated to the desired temperature (500, 550, 600, 650 °C) in a muffle furnace (Carbolite) at a ramping rate of 2 °C $min^{-1}$, and held for

2 h. The materials thus obtained were labeled as g-$C_3N_4$ T °C, where T represents the temperature that was used for the synthesis.

Palladium nanoparticles were deposited on the g-$C_3N_4$ supports using the deposition-precipitation method.[4] 1 g of the support and 125 mg of palladium nitrate dihydrate (~40% Pd, Sigma-Aldrich) were added to 30 ml of deionized (DI) water. This mixture was stirred overnight at 400 rpm at 80 °C in a capped glass bottle. 1 M of NaOH solution was then added to the mixture and the pH was adjusted to 10.0. 5 ml of 0.5 M $NaBH_4$ solution was added to this suspension for reducing the palladium. The Pd/g-$C_3N_4$ was separated using centrifugation at 4500 rpm for 10 min. The catalyst thus obtained was washed 5 times with 50 ml of DI water and 3 times with 50 ml of 200-proof ethanol using centrifugation to separate the solid from the solution after each washing step. The catalysts were dried overnight in a vacuum oven at 100 °C.

Stacked cup carbon nanotube (SCCNT) supports were obtained from Pyrograf Products Inc. (Ohio, USA). The SCCNTs were synthesized by catalytic chemical vapor deposition (CCVD) using methane as a carbon source. Post synthesis, the polyaromatic hydrocarbons were removed from the SCCNT surface by heating them in an inert environment at 700 °C. The materials, thus obtained, were labeled as the pyrolytically stripped (PS) SCCNTs. Based on already reported procedures, 10 g of the PS SCCNTs were oxidized using 500 ml trace metal grade concentrated nitric acid (65% $HNO_3$, Fisher scientific) at 100 °C for 4 h.[5] Post oxidation, the supports were washed with 5 L of deionized water (18 MΩ, Millipore) and dried overnight at 110 °C. The oxidized PS SCCNTs were transferred to a quartz tube reactor, heated to different temperatures (200, 400, 600, 800 °C) with a ramp rate of 10 °C $min^{-1}$ under nitrogen at 200 ml $min^{-1}$, and held at this temperature

for 30 min. The thermally defunctionalized supports thus obtained, were labeled as PS200-PS800 SCCNTs.

Palladium metal was deposited on the surface of the treated PS SCCNTs using the incipient wetness impregnation technique. 187.5 mg of palladium nitrate dihydrate (~ 40 % palladium, Sigma Aldrich) was dissolved in 12.6 ml of deionized water at pH 4.0, adjusted using nitric acid. This solution was added dropwise to 1.5 g of the oxidized supports and sonicated for 5 min. The impregnated supports were dried overnight at room temperature and 65 °C, followed by an 8 h drying at 80 °C. These samples were heated to 250 °C at a ramp rate of 2 °C $min^{-1}$ and held at this temperature in a quartz tube reactor under flowing air at 200 ml $min^{-1}$. This calcination treatment was used for thermally decomposing the palladium precursor. Following this, the reactor was cooled down to room temperature, purged with nitrogen gas at 200 ml $min^{-1}$ to remove any oxygen from the system, and switched to hydrogen at 200 ml $min^{-1}$. The quartz tube reactor temperature was then increased to 400 °C with a ramp rate of 2 °C $min^{-1}$ and held at this temperature for 2 h. This reduction treatment was conducted to convert the palladium oxide to palladium metal in the supported catalysts.

### 5.2.2 Catalyst characterization

The BET surface area and pore volume of the g-$C_3N_4$ supports were obtained using nitrogen adsorption-desorption isotherms at 77 K using the Micromeritics ASAP 2020 instrument. Prior to this analysis, 100 mg of the samples were degassed at 100 °C for 15 h to a residual pressure of 66.66 Pa.

The elemental composition of the carbon nitride supports was investigated using a Perkin Elmer 2100 Series II CHN/S Analyzer. Acetanilide was used as the calibration

standard for the analysis. 1.5 to 2 mg of sample was weighed in tin capsules and the combustion/reduction tests were conducted at 925 and 975 °C. The expected precision and accuracy of the measurements for each element is +/- 0.3%.

X-ray photoelectron spectroscopy (XPS) studies were conducted on the PS SCCNTs using a PHI ESCA 5500 instrument. The samples were irradiated with 225 W monochromated Al Kα X-rays and the pass energy was set at 188 eV for survey scans, 47 eV for high resolution scans, and 59 eV for valence band scans.

Ultraviolet photoelectron spectroscopy (UPS) and work function measurements were performed on a Specs Phoibos NAP-150 hemispherical analyzer with a monochromated Al K-alpha source and a non-monochromated He I-alpha ultraviolet source. During the UPS and WF measurements, the sample was held at a bias voltage of -20 V relative to the spectrometer to accelerate the slow secondary electrons. The sample geometry was with the sample normal parallel to the electrostatic lens axis of the analyzer. Samples were measured at temperatures of 100 °C to 450 °C in 50 °C increments. The position of the work function was determined from the secondary electron cut-off, by fitting a line tangent to the data at point of steepest descent, and extrapolating the line to the intersection with the abscissa. The binding energy of this intersection represents the secondary electron cut-off. A value of 20 eV was added to this binding energy to account for the applied voltage, and the resulting number was subtracted from the photon energy to yield the work function.

The palladium content of the catalysts was measured using inductively coupled plasma-optical emission spectroscopy (ICP-OES) with a Perkin Elmer Optima 8000 instrument. Prior to the analysis, 30 mg of the catalyst was weighed in a ceramic crucible, heated in air at 10K $min^{-1}$ to 1000 °C, and held at this temperature for 6 h. The combustion

process burned off the carbon support, leaving the oxidized palladium metal in the crucible. The contents remaining in the crucible were soaked in 5 ml aqua regia (1:3 nitric acid : hydrochloric acid) overnight to dissolve the palladium metal. The solution was then diluted using 45 ml of DI water and analyzed.

The size of the palladium nanoparticles was calculated from the hydrogen chemisorption isotherms obtained using a Micromeritics ASAP 2020C instrument. For this analysis, 70 to 80 mg of catalyst was packed in a U-shaped chemisorption tube. The catalysts were reduced in-situ under hydrogen at 350 °C for 2 h, followed by evacuation at 350 °C for 2 h to remove any bound hydrogen, and cooled down to room temperature under vacuum. Hydrogen gas was subsequently re-introduced in the system at 35 °C and the total quantity adsorbed ($H_T$) was calculated from the first isotherm. Following this, a vacuum was applied to remove the weakly bound hydrogen and a second adsorption isotherm was recorded to determine the reversibly bound hydrogen ($H_R$).

### 5.2.3 Catalyst performance

The catalysts were tested for the liquid-phase hydrogenation of cinnamaldehyde. The reactions were conducted at ambient pressure in a 100 ml 3-neck round bottom flask (RBF), connected to a condenser at 4 °C. For the catalytic tests, 100 mg of the catalyst, 40 ml dioxane, and 365 mg of decane as an internal standard were added to the RBF. The mixture was placed in an oil bath and stirred continuously at 500 rpm using an IKA-RCT magnetic stir plate equipped with a PT1000 thermocouple. Nitrogen was purged through the system at room temperature at 20 ml $min^{-1}$ at ambient pressure using a Brooks mass flow controller and a fine frit bubbler (10 – 20 μm). Following this, hydrogen was bubbled through the system at

20 ml $min^{-1}$ and ambient pressure for 30 min and the mixture was simultaneously heated to 80 °C. 5 g of cinnamaldehyde in 10 ml of dioxane was then added to the flask using the third neck, fitted with a rubber septum and a needle. The addition of cinnamaldehyde was marked as the start time of the reaction and 200 µl samples were withdrawn every 15 min to follow the progress of the reaction. The samples were collected in pre-cooled 2 ml glass vials to quench the reaction and prevent solvent loss. All the tests were conducted in triplicates.

The reactant and products were analyzed using an Agilent 7890A gas chromatograph (GC) connected with an HP-5 column and a flame ionization detector (FID). 100 µl of the reaction samples were diluted with 1400 µl of dioxane, filtered using a 0.22 µm nylon filter, and then injected in the GC. The operating conditions of the GC-FID consisted of a split ratio of 20:1 at 20 ml $min^{-1}$ and an inlet heater temperature of 300 °C. A total flow rate of 24 ml $min^{-1}$, septum purge flow rate of 3 ml $min^{-1}$, and column flow of 1 ml $min^{-1}$ was used for the GC-FID analysis. Initially, the oven temperature was maintained at 40 °C for 1 min and then increased to 180 °C at 10 °C $min^{-1}$. The temperature of the FID heater was maintained at 300 °C during the analysis.

## 5.3 Results and Discussion

### 5.3.1 Carbon support properties

Mesoporous graphitic carbon nitride materials were chosen as supports in this study due to the ease in tunability of their electronic properties, as has been previously reported.[6] Particularly, in the photocatalysis literature, different strategies have been designed for modulating the band gap of carbon nitride materials. For example, a 0.21 eV decrease in the band gap was achieved by inducing changes in the separation of layers of g-$C_3N_4$ via oxygen

incorporation.[7] In this work, the synthesis temperature of the support was varied for altering its electronic properties through stacking and lattice constant modifications.[6] This control on the electronic nature along with mesoporous structure of these carbons permits the isolation of transport effects from the interfacial interactions in the metal/carbon catalysts. These advantages make carbon nitride a support material of choice in this work for tailoring the metal-support interaction effects.

In the case of carbon materials with oxygen functional groups, literature from optoelectronic studies has demonstrated correlations between the surface oxygen content and work function of the nanocarbons.[8-10] Specifically, these correlations have been established for graphene oxide (GO) materials due to their extensive utilization for optoelectronic applications. The variations in the work function of the GO upon reduction are typically attributed to the changes in the density and nature of surface oxygen functional groups, suggesting that the defunctionalization of carbon materials other than GO could also allow for tuning their electronic properties. Utilizing this knowledge, herein the SCCNT supports were thermally defunctionalized for selectively removing surface oxygen functional groups, as has been established in the literature.[11] This potential for tunability of electronic properties coupled with the absence of micropores in the SCCNTs make them ideal candidates for studying the interfacial catalytic phenomena in carbon supported catalysts.

With the help of g-$C_3N_4$ and SCCNT supports, herein efforts are directed towards decoding the influence of nitrogen and oxygen functionalities on the electronic properties of carbon materials and thereby their role as supports in hydrogenation catalysts. For the carbon nitride scaffolds, the elemental composition was confirmed using CHN analysis and the ratio of carbon to nitrogen was observed to be uniform across the different supports despite the

changes in synthesis temperature (Supplemental Information Table S1). In contrast, in the case of SCCNT supports, decrease in the surface O/C ratio from 0.24 to 0.11 was observed between the pristine and 600 °C annealed carbons using XPS (Supplemental Information Figure S2). The electronic nature of the PS SCCNTs supported catalysts was studied using UPS and a decrease in the work function from 5.1 to 4.73 eV was observed with increasing thermal annealing temperature (Supplemental Information Table S3). These changes in the WF were in coherence with the observations on GO that have been previously reported in the literature.

### 5.3.2 Synthesis of carbon supported palladium catalysts

Deposition-precipitation and incipient wetness impregnation techniques were used to deposit Pd metal on the carbon nitride and SCCNT supports, respectively. These techniques were preferred over the ligand-based synthesis methods in order to avoid the possible steric and electronic effects of the ligands. The palladium nitrate precursor was specifically preferred over chloride-based precursors to avoid poisoning of the metal catalysts from the chloride residues. Overall, a uniform palladium loading was observed on all the catalyst supports using ICP-OES analysis (Supplemental Information Table S4). Hydrogen chemisorption studies confirmed that the average particle size of 5 nm on both the carbon nitride and SCCNT supported catalysts (Supplemental Information Table S5). These studies eliminated the effects due to differences in metal loading or particle size variations on the performance of these two catalyst series.

### 5.3.3 Catalytic performance for α,β- unsaturated aldehydes

To investigate the influence of the support's electronic properties on the performance of Pd catalysts, the liquid-phase hydrogenation of α,β- unsaturated aldehyde – cinnamaldehyde was used as a probe reaction. This reaction was particularly of interest due to its sensitivity towards the electronic configuration of the metal active phase. Pd catalysts are of prime interest for this reaction due to their selectivity towards the C=C bond for the production of hydrocinnamaldehyde (HCALD), which is an important pharmaceutical intermediate (Figure 1). Comparing the selectivity of the catalysts designed in this study revealed interesting correlations with the support annealing and synthesis temperatures. For the Pd/$C_3N_4$ catalysts, the HCALD selectivity increased with decreasing support synthesis temperature and increasing band gap (Figure 2). Contrary to this, for the Pd/PS catalysts, the HCALD selectivity increased with increasing support treatment temperature and decreasing work function (Figure 3). The correlations for the PS SCCNT supported catalysts even demonstrated linear dependence between the catalyst work function and HCALD selectivity (Figure 4). Additionally, even minor changes in the surface O/C ratio resulted in changes in the electronic properties of the support that further manifested themselves in coherent changes in HCALD selectivity. This indicates that the electronic interactions between the metal and support can be modulated by tuning the chemical and electronic properties of the carbon scaffolds.

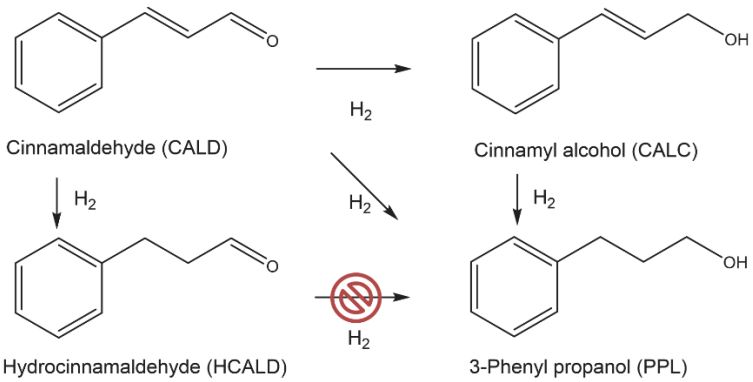


Figure 1. Reaction scheme for cinnamaldehyde (CALD) hydrogenation

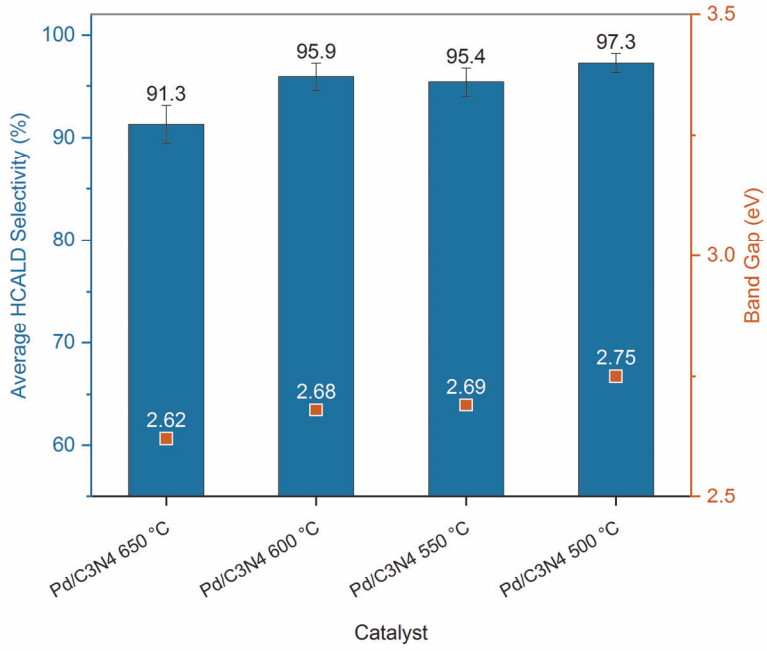


Figure 2. HCALD selectivity for $C_3N_4$ supported catalysts determined experimentally and band gap for the supports as reported in the literature[6]

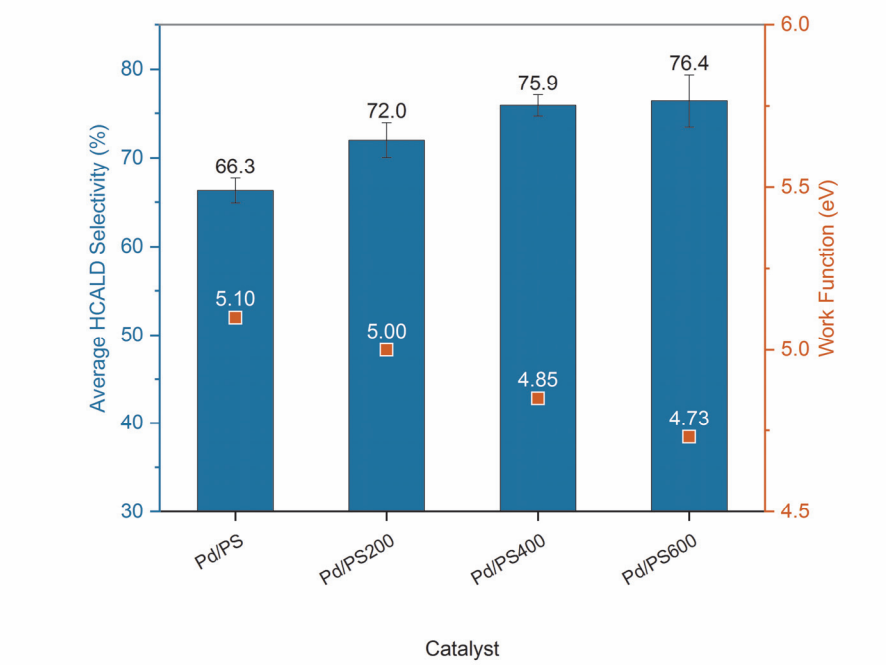


Figure 3. HCALD selectivity and work function as obtained from UPS for catalysts supported on PS SCCNTs

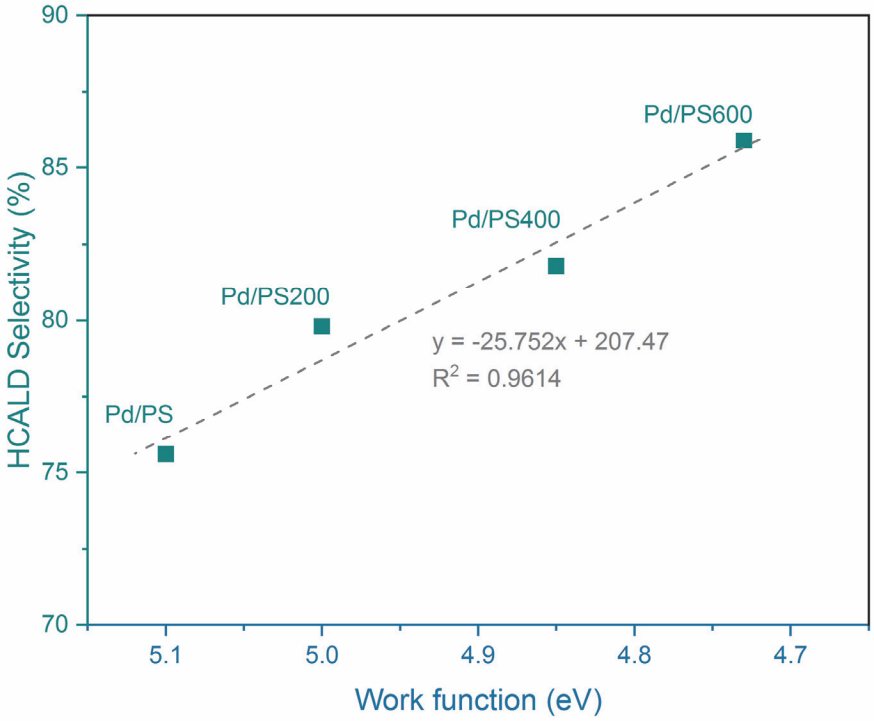


Figure 4. Linear trend between the HCALD selectivity and work function of palladium catalysts supported on PS SCCNTs

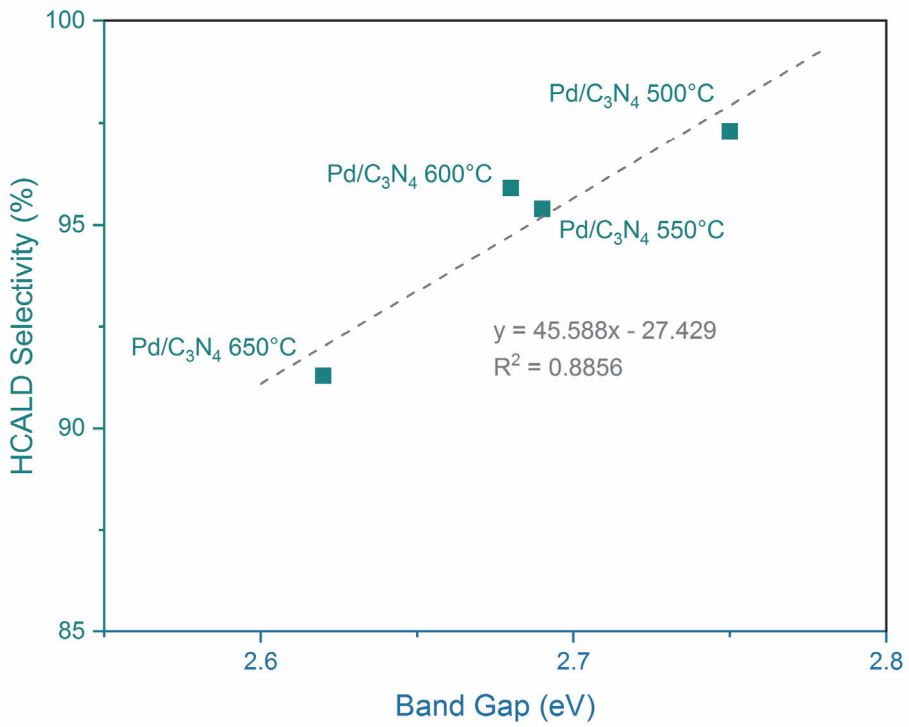


Figure 5. Trend between the HCALD selectivity and work function of palladium catalysts supported on $C_3N_4$

### 5.4 Conclusions

We demonstrate here linear correlations between the selectivity obtained for cinnamaldehyde hydrogenation, a model α,β-unsaturated compound, the electronic properties of the supported Pd catalyst. Hence, UPS offers a simple and effective way to predict the catalytic activity of metals for hydrogenation reactions and beyond. Furthermore, we showed that for a given nanostructured catalyst, its performance can be modulated through simple thermal treatments. We already demonstrate the validity of this approach for carbons and carbon nitrides but anticipate that it can be extended to a broad range of O-, N-, P-, S-doped carbons for applications in both thermocatalysis and electrocatalysis.

## 5.5 References


1. Gunasooriya, G. T. K. K.; Seebauer, E. G.; Saeys, M. *ACS Catal.* **2017,** *7*, 1966-1970.

2. Gunasooriya, G. T. K. K.; Saeys, M. In *Nanotechnology in Catalysis*, Van de Voorde, M., Bert, S., Eds.; 2017.

3. Iqbal, W.; Dong, C.; Xing, M.; Tan, X.; Zhang, J. *Catal. Sci. Tech.* **2017,** *7*, 1726-1734.

4. Wang, Y.; Yao, J.; Li, H.; Su, D.; Antonietti, M. *J. Am. Chem. Soc.* **2011,** *133*, 2362-2365.

5. Tessonnier, J.-P.; Rosenthal, D.; Hansen, T. W.; Hess, C.; Schuster, M. E.; Blume, R.; Girgsdies, F.; Pfänder, N.; Timpe, O.; Su, D. S.; Schlögl, R. *Carbon* **2009,** *47*, 1779-1798.

6. Zuluaga, S.; Liu, L.-H.; Shafiq, N.; Rupich, S. M.; Veyan, J.-F.; Chabal, Y. J.; Thonhauser, T. *Phys. Chem. Chem. Phys.* **2015,** *17*, 957-962.

7. Li, J.; Shen, B.; Hong, Z.; Lin, B.; Gao, B.; Chen, Y. *Chem. Commun.* **2012,** *48*, 12017-12019.

8. Mathkar, A.; Tozier, D.; Cox, P.; Ong, P.; Galande, C.; Balakrishnan, K.; Leela Mohana Reddy, A.; Ajayan, P. M. *J. Phys. Chem. Lett.* **2012,** *3*, 986-991.

9. Loh, K. P.; Bao, Q.; Eda, G.; Chhowalla, M. *Nat. Chem.* **2010,** *2*, 1015-1024.

10. Kumar, P. V.; Bernardi, M.; Grossman, J. C. *ACS Nano* **2013,** *7*, 1638-1645.

11. Kundu, S.; Wang, Y.; Xia, W.; Muhler, M. *J. Phys. Chem. C* **2008,** *112*, 16869-16878.

## 5.6 Supporting Information

Table S1. Elemental composition of carbon nitride catalysts as obtained from CHN analysis conducted at 925 °C

| Support Synthesis Temperature (°C) | Carbon (%) | Hydrogen (%) | Nitrogen (%) | C:N |
|---|---|---|---|---|
| 500 | 34.18 | 1.86 | 59.94 | 0.57 |
| 550 | 34.66 | 1.56 | 60.12 | 0.58 |
| 600 | 34.71 | 1.34 | 59.68 | 0.58 |
| 650 | 35.02 | 1.30 | 60.91 | 0.57 |

Table S2. Surface oxygen to carbon ratio (O/C) for PS SCCNT supports as obtained from X-ray photoelectron spectroscopy (XPS)

| Support | O/C |
|---|---|
| PS | 0.24 |
| PS200 | 0.23 |
| PS400 | 0.23 |
| PS600 | 0.11 |

Table S3. Work function of the palladium catalysts supported on PS SCCNTs as measured with ultraviolet photoelectron spectroscopy (UPS)

| Catalyst | Work function (eV) |
|---|---|
| Pd/PS | 5.10 |
| Pd/PS200 | 5.00 |
| Pd/PS400 | 4.85 |
| Pd/PS600 | 4.73 |

Table S4. Inductively Coupled Plasma-Optical Emission Spectroscopy (ICP-OES) results for the palladium metal loading in catalysts using the PS and carbon nitride supports

| Catalyst | Pd metal loading (%) |
|---|---|
| Pd/PS | 3.3 |
| Pd/PS200 | 3.2 |
| Pd/PS400 | 3.3 |
| Pd/PS600 | 3.9 |
| Pd/$C_3N_4$ 500 °C | 4.3 |
| Pd/$C_3N_4$ 550 °C | 4.6 |
| Pd/$C_3N_4$ 600 °C | 4.2 |
| Pd/$C_3N_4$ 650 °C | 3.9 |

Table S5. Sizes of palladium nanoparticle as obtained from hydrogen chemisorption adsorption isotherms

| Catalyst | Particle size (nm) |
|---|---|
| Pd/PS | 4.86 |
| Pd/PS200 | 4.94 |
| Pd/PS400 | 5.08 |
| Pd/PS600 | 4.98 |
| Pd/$C_3N_4$ 500 °C | 4.64 |
| Pd/$C_3N_4$ 550 °C | 5.32 |
| Pd/$C_3N_4$ 600 °C | 5.33 |
| Pd/$C_3N_4$ 650 °C | 4.45 |

# CHAPTER 6

# GENERAL CONCLUSION

Lignocellulosic biomass offers a promising alternative to petroleum resources for the production of specialty and fine chemicals. However, the transition from a petroleum-based to a bio-based chemical industry entails several challenges. For example, the platform molecules obtained from biomass consist of highly conjugated and oxidized moieties, which present a substantially different chemistry as compared to the hydrocarbon building blocks derived from fossil feedstocks. The prevalence of C=C and C=O bonds in these platform molecules require reactions that can selectively alter these functionalities. In this regard, selective hydrogenation reactions are of prime significance and designing catalysts that can selectively hydrogenate a target double bond within multifunctional molecules is imperative for the production of renewable chemicals from biomass.

Carbon-supported noble metal catalysts are commonly used for hydrogenation reactions in the petroleum industry. These materials are expected to retain their importance in the bio-based chemical industry, ultimately expanding their applications to reactions performed in aqueous media as traditional metal oxide supports lose their structural integrity in this environment. Despite this significance, the fundamental properties of these catalysts remain poorly understood because of the complex nature of carbon materials. This gap in knowledge hinders the rational design of carbon-supported catalysts for selective hydrogenation reactions.

In this work, attempts were made to elucidate the role of carbons as catalyst supports by decreasing the complexity of the investigated materials. Particularly, a simpler carbon

platform that offered a control on the support's chemical and electronic properties while preserving its morphological structure and surface area was developed. Uniform loading of Pd metal on the carbons allowed a direct comparison of catalysts for selective hydrogenation of α,β- unsaturated aldehydes. Differences in the selectivity towards C=C bond hydrogenation were observed with varying surface chemistry and graphitic character of the support. As the support surface area, porosity, and graphitic character were preserved, the observed differences in selectivity were attributed to metal-support interaction (MSI) effects. Detailed investigation revealed that the trends in catalytic selectivity were consistent with the contribution of a $Pd^{\delta+}$ phase as observed using X-ray photoelectron spectroscopy (XPS). The presence of oxides, carbides, and hydrides under hydrogen environment was ruled out using near ambient pressure-XPS (NAP-XPS) studies. The interatomic distances obtained from aberration corrected transmission electron microscopy (ac-TEM) also confirmed the presence of metallic Pd in the nanoparticles. These observations verified that the contribution from the $Pd^{\delta+}$ phase is due to electronic interactions between the metal and support rather than a change in the oxidation state of palladium due to chemical bonding. The electronic metal-support interaction (EMSI) effects, observed here, also altered the ratio of the reversibly ($H_R$) to irreversibly ($H_I$) bound hydrogen, further confirming the changes in electronic structure of Pd atoms.

Once the presence of EMSI effects in carbon-supported catalysts was established, efforts were directed towards elucidating the role of supports on these interactions in detail using NAP-XPS studies, XPS depth profiling, ultraviolet photoelectron spectroscopy (UPS), controlled sintering experiments, and density functional theory (DFT) calculations. Our investigation revealed that O-containing groups saturate defects on carbon surfaces and

create surface dipoles that alter the electronic structure of the surface. The consequences of these modifications were probed directly by UPS as this technique allowed us to measure the work function (WF) of the catalytic materials. Combining the UPS results with catalytic data confirmed that the shift in WF with support annealing temperature was consistent with changes in the selectivity for cinnamaldehyde hydrogenation. Further investigation using XPS-based depth profiling and DFT studies proved that the changes induced in the electronic structure of the surface results in a charge transfer at the metal-carbon interface. Interestingly, this charge transfer was strong enough to alter the core electrons of the Pd atoms at the interface, as observed from XPS, and rapidly decayed with increasing distance from the interface.

We further studied the interfacial effects by investigating the role of the Pd-C contacts through controlled sintering experiments. Increasing the Pd particle size altered the ratio of surface to interfacial Pd atoms and demonstrated correlations between the contribution of $Pd^{\delta+}$ and catalytic activity. Simple geometric effects could not explain the drop in reaction rate with increasing particle size as the trends in catalytic activity remained unchanged even after normalizing the rate with surface active Pd atoms. In order to understand these interfacial effects, we developed a simple model based on XPS and kinetic data and found that atoms near the interface demonstrate an intrinsic reaction rate that is two orders of magnitude higher than that of the atoms further away. This model was consistent with DFT studies, which revealed that the charge transfer weakens the binding of hydrogen, in coherence with chemisorption, and lowers the activation energy for the transition state associated with hydrocinnamaldehyde (HCALD) by ca. 10 kJ $mol^{-1}$. The magnitude of change in the transition state activation energy was coherent with the experimentally

observed 2 orders of magnitude change in rate at 80 °C. Because of these alterations, the HCALD formation is boosted relative to phenyl propanol, which explains the observed change in selectivity for the reaction.

Finally, as the WF was observed to be an important parameter, we tried to generalize our findings by studying other materials with significantly different electronic properties, like $C_3N_4$. The results obtained so far are consistent but need additional work, especially to fully understand the electronic effects at the metal-support heterojunction and decouple the roles of WF and band gap.

In summary, our work demonstrated the existence of electronic metal-support interactions for carbon supports and offered a simple yet elite approach for tuning these effects for hydrogenation catalysts. The structure-activity correlations that were developed will ultimately facilitate the fine tuning of carbon-supported metal catalysts for a broad range of reactions beyond hydrogenations, in particular for biomass conversion reactions.

# CHAPTER 7

# FUTURE DIRECTIONS

Our work provides strong evidence for the presence of electronic metal-support interactions (EMSI) for Pd/C and provides some guidance for the rational design of carbon-supported catalysts. However, additional work is still needed to control these support effects. Here we highlight three different routes that could be explored for tailoring the interfacial interactions and further improving the fundamental understanding of nanocarbon-supported catalysts.

## 7.1 Effect of metal active phase

Palladium on carbon (Pd/C) catalysts that have been studied in this work are known to form hydrides under high pressure conditions, which is inconvenient for studying the active phase in more details. Using noble metals that do not form hydrides, such as platinum and ruthenium, would allow us to generalize our findings and enable an investigation of the active phase for a broader range of reaction conditions, in particular for pressures common in industrial hydrogenation reactions. Since Pd, Pt, and Ru nanoparticles have different work functions and d band centers, our work would also elucidate the effect of these properties on the interactions of the noble metals with nanocarbons, specifically on the direction and intensity of the charge transfer.

### 7.2 Effect of work function of carbons

Tailoring the electronic properties of carbon materials offered novel insights into the EMSI effects in this work. However, these effects were only studied for a limited set of carbon supports, namely the carbon nitride and oxygen-functionalized carbon nanotubes. Extending this study to a variety of other carbon supports can provide a more detailed understanding of the interfacial phenomena and thereby allow a better control on the EMSI effects. Ultimately, this work would generate transformative concepts to enhance or tailor the selectivity of a catalyst without altering the elemental composition of the active phase.

#### 7.2.1 Top-down approach

Materials such as carbon nanotubes present several challenges in the measurement of the work function and valence band positions. In contrast, the work function of graphene oxide (GO) and reduced graphene oxide (rGO) can be easily measured using simple spectrophotometric techniques. The structural simplicity of these materials permits the evaluation of even the valence band position using ultra-violet photoelectron spectroscopy (UPS). With the help of these techniques, a more detailed understanding of the electronic properties of carbon materials can be developed. As a result, trends between the electronic nature of the supports, the performance of metal nanoparticles decorating their surface, and EMSI effects would be further strengthened through this proposed work.

#### 7.2.2 Bottom-up approach

In addition to altering support functionalization, the electronic properties of the nanocarbons can also be tuned by controlling their size. For example, graphene quantum dots

(GQDs) allow for changing their WF through size modulation via simple modifications in the synthesis conditions. Using a bottom-up approach for controlled GQD synthesis from sugars, correlations between the electronic nature of nanocarbons and their influence on EMSI effects could be determined.

### 7.3 Quantitative investigation of interfacial charge transfer

The adsorption of oxygen and moisture on the catalyst surface during ex situ characterization causes the structure-activity correlations to be qualitative in nature. Therefore, near-ambient pressure synchrotron-based X-ray photoelectron spectroscopy (NAP-XPS) studies under different atmospheres are essential for a quantitative analysis of the EMSI. NAP-XPS studies were already conducted at the ISISS beamline at the BESSY II synchrotron facility in Germany. The dynamic changes of the support (without palladium) and catalyst precursor were monitored throughout the calcination, reduction, and thermal annealing steps. Once fully analyzed, these results will provide further insights into the changes of the active phase as a function of the nature and density of the oxygen-containing groups decorating the surface. We envision that additional NAP-XPS experiments on Pd/GO and Pd/GQD as well as in situ catalytic tests (*e.g.,* for alkyne hydrogenation) would provide important information on the role of the $Pd^{\delta+}$ phase under reaction conditions.